

Department of Physics and Astronomy

University of Heidelberg

Master thesis

in Physics

submitted by

Luisa Bergmann

born in Ulm-Söflingen

2019



**Probing the path-length dependence  
of jet energy loss  
with correlation functions  
in JEWEL**

This Master thesis has been carried out by Luisa Bergmann

at the

Physikalisches Institut Heidelberg

under the supervision of

Prof. Dr. Johanna Stachel



## Abstract

In this thesis the sensitivity of angular correlation functions to the path-length of hard scattered partons was tested using Monte Carlo simulations. The aim was to define observables that can be used in real data analysis.

In the general characterization of jets and jet modification, 80-90% of the partons momentum were contained in the leading jet. Medium modifications reduce the leading jet momentum by 20-60% and spread the constituents over a larger area compared to the vacuum case. The influence of the medium was found to decrease with increasing parton momentum. When restricting the transverse momentum of the jets leading track to different trigger intervals, different ranges in parton  $p_T$  and jet  $p_T$  are selected. Since the main fraction of the jets momentum is contained in the leading track, the jet  $p_T$  increases on average with increasing leading track momentum. Soft fragments are scattered outside the scope of the jet in a medium and the remaining particles are located closer to the respective jet axis, compared to jets with similar  $p_T$  in vacuum. The mean path-length corresponding to the triggered jet decreases with increasing trigger momentum. In different bins of the trigger hadron azimuthal angle relative to the event plane,  $\Delta\phi$ , out-of plane bins on average correspond to larger path-lengths. The dependency is stronger for higher  $p_T^{\text{trig}}$  and more peripheral systems. For a back-to-back dihadron trigger pair, the path-length distributions reflect the asymmetry of the trigger conditions. The  $I_{AA}$ , the comparison of the yield in medium and vacuum, for two-particle correlations on the near- and the away-side are consistent with unity. The same behavior was found for the near-sides of trigger 1 and 2 in 2+1 correlations. 2+1 correlations are obtained by selecting back-to-back in azimuth located hadrons as trigger particles for the correlation functions. By selecting the trigger particle for two-particle correlations out of a bin in  $\Delta\phi$ , a modulation of the  $I_{AA}$  is observed for different triggers in the same bin in  $\Delta\phi$ . The modulation decreases when going from (0-10)% to (50-60)% centrality.

It was found that the comparison of different trigger conditions within the same centrality or the comparison of the same trigger condition in different centralities can be used to access relative path-length changes between the different systems. In 2+1 correlations, the peak width in  $\Delta\eta$  can be used as tool to select on different relative path-lengths between trigger 1 and trigger 2. These observables are applicable as tools for real data analysis.



## Kurzfassung

In dieser Arbeit wurde die Sensibilität von Winkelkorrelationsfunktionen auf die Weglänge von Partonen, welche mit hohem Impulsübertrag gestreut wurden, unter der Verwendung von Monte Carlo Simulationen getestet. Das Ziel war das Herausarbeiten von Observablen, welche in der Analyse echter Daten verwendet werden können.

In der allgemeinen Charakterisierung von Jets und Jet Modifikation wurde festgestellt, dass der Jet mit dem größten Anteil am Gesamtimpuls 80-90% des Partonimpulses trägt. Durch Modifikationen durch das Medium ist der Impuls dieses Jets im Schnitt um 20-60% reduziert und die in ihm enthaltenen Teilchen werden über eine größere Fläche gestreut als es bei vergleichbaren Jets ohne Medieumeeinfluss der Fall ist. Wenn der Transversalimpuls des Teilchens mit dem größten Bruchteil des Jetimpulses in verschiedene Triggerintervallen unterteilt wird, werden gleichzeitig verschiedene Bereiche in Jet- und Partonimpuls selektiert. Da der größte Teil des Jetimpulses in einem einzelnen Teilchen enthalten ist, steigt der Jetimpuls mit dem steigenden Impuls dieses Teilchens. Fragmente mit nur einem kleinen Anteil des Impulses werden im Medium außerhalb des Umfangs des Jets gestreut, daher befinden sich die verbleibenden Teilchen des Jets näher an der Jetachse als die Teilchen von Jets mit vergleichbarem Impuls im Vacuum. Die mittlere Weglänge, welche durch den getriggerten Jet selektiert wird, sinkt mit steigendem Triggerimpuls. Bei den verschiedenen Bins des Trigger-Azimutalwinkels relativ zur Ereignisfläche  $\Delta\phi$  entsprechen Bins mit zunehmender Transversalität zur Ereignisfläche einer längeren Weglänge. Diese Abhängigkeit ist stärker für Teilchen mit hohem Triggerimpuls und in peripheren Kollisionen. Für Hadron-Triggerpaare, welche in gegensätzliche Richtungen emittiert wurden, entsprechen die Verteilungen der Weglänge der Asymmetrie der Triggerbedingungen. Der  $I_{AA}$ , der Vergleich von Peakintegral in Medium und Vacuum, ist für Zwei-Teilchen Korrelationen konsistent mit 1, sowohl auf der nahen als auch auf der fernen Peakposition. Das gleiche Verhalten wurde für die nahen Seiten der beiden Trigger in 2+1 Korrelationen beobachtet. Die Erzeugung von 2+1 Korrelationen erfolgt durch die Auswahl zweier Hadronen als Trigger, die gegensätzlich in Azimut emittiert wurden. Durch die Selektierung des Triggerteilchens für Zwei-Teilchen Korrelationen in ein Bin in  $\Delta\phi$  wurde eine Modulation des  $I_{AA}$  für verschiedene Trigger mit gleichem  $\Delta\phi$  beobachtet. Zwischen (0-10)% und (50-60)% Zentralität nimmt die Stärke der Modulation ab.

Es wurde festgestellt, dass der Vergleich von verschiedenen Triggerbedingungen für die gleiche Zentralität oder der Vergleich der gleichen Triggerbedingung für verschiedene Zentralitäten benutzt werden kann, um auf die relative Weglänge zwischen zwei Systemen zugreifen zu können. In 2+1 Korrelationen kann die Peakweite in  $\Delta\eta$  als Mittel genutzt werden um die verschiedenen relativen Weglängen zwischen Trigger 1 und 2 zu selektieren. Diese Observablen können als Werkzeuge für die Analyse echter Daten genutzt werden.



# Contents

<b>1</b>	<b>Introduction</b>	<b>1</b>
<b>2</b>	<b>Quantum chromodynamics and heavy-ion collisions</b>	<b>3</b>
2.1	Color and asymptotic freedom . . . . .	3
2.2	The quark-gluon plasma and heavy-ion collisions . . . . .	7
<b>3</b>	<b>Jets as a probe of the QGP</b>	<b>11</b>
3.1	Jet production in hadronic collisions . . . . .	11
3.2	Jet quenching . . . . .	13
3.3	Two-particle and 2+1 correlations . . . . .	15
<b>4</b>	<b>The event generator JEWEL</b>	<b>19</b>
4.1	The physics of JEWEL . . . . .	19
4.1.1	General principles . . . . .	19
4.1.2	Medium model . . . . .	22
4.2	Data simulation - parameter selection . . . . .	23
<b>5</b>	<b>Analysis and discussion</b>	<b>25</b>
5.1	Particle selection and jet reconstruction . . . . .	25
5.2	Characterization of jets and jet modification in JEWEL . . . . .	27
5.2.1	Jet transverse momentum . . . . .	27
5.2.2	Average angular distance of the jets constituents to the jet axis . . . . .	30
5.2.3	Average transverse momentum and number of jet constituents . . . . .	32
5.3	Quantifying the path-length . . . . .	37
5.3.1	Geometrical and energy-density weighted path-length . . . . .	37
5.3.2	Path-length and jet modification . . . . .	41
5.4	Triggered distributions . . . . .	44
5.4.1	Single hadron trigger . . . . .	44
5.4.2	Hadron triggered path-length distributions . . . . .	55
5.4.3	Path-length with respect to the event plane . . . . .	57
5.4.4	Dihadron trigger . . . . .	62
5.5	Correlation functions . . . . .	69
5.5.1	Two-particle correlations . . . . .	69
5.5.2	2+1 correlations . . . . .	73
5.5.3	Results . . . . .	74
<b>6</b>	<b>Conclusions and Outlook</b>	<b>81</b>



# Chapter 1

## Introduction

The search for the fundamental building blocks of our universe has inspired various theories and experiments over the centuries. While great progress has been made – the Standard Model of Particle Physics[1] with great success being the current state of the art – numerous details still remain unknown.

One of the ongoing fields of research is the study of Quantum Chromodynamics (QCD), the theory of the strong interaction. The fundamental quarks and gluons, constituents of the material world around us [2–4] in hadrons such as for example protons and neutrons, are the particles that interact via the strong interaction. They have, however, never been observed as free particles since they are confined within the hadrons [5]. In ultra-relativistic heavy-ion collisions, where the nucleons are exposed to high energy densities, the bound structures are dissipated [6, 7]. The heated matter undergoes a phase transition and forms a state, in which the quarks and gluons act as quasi free particles: the Quark-Gluon Plasma (QGP). Contrary to elementary hadronic collisions, where single nucleons are collided, the collision of heavy nuclei creates a many body system. This system has defining properties like its viscosity, temperature and interaction properties, which are collective effects from inter-particle interactions in the medium [8]. The QGP has a very short lifetime,  $\mathcal{O}(10^{-23} \text{ s})$  [9]. It expands and cools down to the critical temperature  $T_c = 156 \pm 1.5 \text{ MeV}$  [10], where the hadronization sets in. At this temperature, the hadronic abundancies are specified. The hadron gas expands and cools down further, until the hadrons do not interact with each other anymore. At this point, the kinematical structure is fixed [8]. Due to the very short lifetime, the QGP can only be studied via the particles emerging from the collision and expansion. Tools are needed to extract information about its properties. One very useful tool are jets, originating from the fragmentation of two hard scattered partons [8]. Since the scattering takes place at high transverse momenta  $p_T$ , their cross section and development down to momenta  $\mathcal{O}(1 \text{ GeV})$  can be calculated by using perturbative QCD. Jets are therefore theoretically well understood. Since they obey momentum conservation, the two partons are emitted back-to-back in azimuth, which can be used as identifying characteristic, and carry the same momentum. The latter becomes important when interactions of jets with the QGP are studied. Since jets are produced in the early stages of hadronic collisions, they traverse the medium completely and interact with its constituents. Thereby, they transfer momentum to the medium particles. This medium induced reduction of the jets

momentum is known as quenching. The fraction of the momentum transferred depends on the nature of the interactions and the in-medium path-length of the parton. Thus the study of the partons path-length dependent quenching yields insight into the properties of the medium.

Due to the hadronization of the thermalized medium, high multiplicities, i.e. particle numbers, are characteristic for heavy-ion collisions. This complicates the identification of jets in single events especially at low jet momenta, since it is impossible to distinguish between soft jet fragments and the hadronized medium particles. With angular correlation functions, this complication is circumvented. In the analysis of angular correlation functions, a single hadron is taken as proxy for the jet. With  $\varphi$  being the azimuthal angle and  $\eta$  being the pseudorapidity of a particle, the angular distances  $\Delta\varphi$  and  $\Delta\eta$  of the trigger hadron to all other particles in the event are calculated. In this way, jets can be studied both on a statistical basis, rather than event-by-event, and independent of specific jet definitions. In this thesis, the sensitivity of angular correlation functions to the in-medium path-length of hard scattered partons is tested using Monte Carlo (MC) based simulations. The simulation program used is JEWEL [11–13]. In JEWEL, the assumptions going into the implementation are kept on a minimal level, which makes it a widely applicable and comparable simulation. Furthermore, the event layout is kept very simple. Only one dijet system is generated per event and the medium is not hadronized. In this way, features of jets can be studied without distortion. The aim of the analysis is to carve out observables that can be used to measure the path-length of hard scattered partons. The usage of MC simulations for this purpose allows for the establishing of a basis for real data analysis. To connect the observables obtained from angular correlation functions to the path-length of the underlying hard parton, jets and jet modification, as well as path-length distributions, were studied prior to the correlation functions evaluation. For this, the jet reconstruction package FastJet [14, 15] was used.

The thesis is structured as follows. In Chapter 2, a short introduction to QCD and the creation of the QGP in heavy-ion collisions is given. The geometry of such a collision is described in the scope of the Glauber model. The next chapter addresses the generation and fragmentation process of jets, as well as the interaction processes that occur in the medium. Correlation functions and observables that can be extracted from them, are explained qualitatively. In Chapter 4, the principles of the Monte Carlo simulator JEWEL are illustrated. Chapter 5 describes the analysis done for this thesis. Results and conclusions are discussed along the way. In the last chapter, the conclusion reached in this work are summarized. Furthermore, an outlook is given about possible extensions and further uses of the presented study.

# Chapter 2

## Quantum chromodynamics and heavy-ion collisions

The Standard Model of particle physics (SM) summarizes the current understanding of the elementary particles and their interactions. These forces – electromagnetism and the strong and weak interaction – are described by the exchange of force carriers (bosons) between the fundamental fermions (quarks and leptons). The fourth fundamental force, gravity, is not part of the SM, as there is no Quantum Field Theory of it.

This chapter gives a short introduction to the basics of the strong interaction. Integral features like color confinement and asymptotic freedom are explained. Following from these characteristics, the Quark-Gluon Plasma and its production in heavy-ion collisions is introduced. The chapter closes with the introduction of collision simulation in a Glauber Monte Carlo framework.

### 2.1 Color and asymptotic freedom

This section follows the references [1, 5, 16]. Quantum Chromodynamics (QCD) is the quantum field theory of the strong interaction. It is based on the SU(3) symmetry group [17, 18], consisting of three complex dimensions. Its generators, eight linearly independent  $3 \times 3$  matrices, introduce three additional degrees of freedom. They are called "color", with red, green and blue as the different states. Accordingly, only particles that carry this color charge – quarks and gluons – participate in strong interactions. Similar to the electric charge in Quantum Electrodynamics (QED), antiparticles in QCD carry anti-color. The Lagrangian of the interaction is given by [16]

$$\mathcal{L}_{\text{QCD}} = \sum_q \bar{\psi}_{q,a} (i\gamma^\mu \partial_\mu \delta_{ab} - m_q \delta_{ab} - g_s \gamma^\mu t_{ab}^C \mathcal{A}_\mu^C) \psi_{q,b} - \frac{1}{4} F_{\mu\nu}^A F^{A\mu\nu}, \quad (2.1)$$

where  $a, b$  are color-indices and  $C = 1, \dots, 8$  accesses the eight different generator matrices.  $\gamma^\mu$  are the Dirac matrices and  $g_s$  is the strong coupling.

The  $\psi$  ( $\bar{\psi}$ ) are spinors for quarks of flavor  $q$  mass  $m_q$ , going into (out of) the interaction vertex. Thus, the first two terms in brackets comprise the Dirac Lagrangian. Since SU(3)

constitutes a symmetry of QCD, additional gauge fields are necessary to ensure its local gauge invariance. In Eq. (2.1) they are represented by  $\mathcal{A}_\mu^C$  and correspond to the eight physical gluons, introducing interactions between quarks via gluons. The presence of the generator matrices  $t_{ab}^C$  indicates the color flow in these interactions. Quarks and gluons are rotated in color space by the fundamental and adjoint ( $t_{ab}^C \hat{=} T_{ab}^C$ ) representation of the generators, respectively. The fundamental representation is usually given by the eight Gell-Mann matrices with normalization  $\text{Tr } t^A t^B = T_R \delta^{AB}$ ,  $T_R = \frac{1}{2}$ . Following Noether's theorem, color is conserved at each strong interaction vertex. Hence, as gluons may connect quarks with different color charges, they themselves are required to carry a color charge, giving rise to self-interactions. In the Lagrangian, these gluon self-interactions are summarized in the term  $F_{\mu\nu}^A F^{A\mu\nu}$ , with [16]

$$F_{\mu\nu}^A = \partial_\mu \mathcal{A}_\nu^A - \partial_\nu \mathcal{A}_\mu^A - g_s f_{ABC} \mathcal{A}_\mu^B \mathcal{A}_\nu^C, \quad (2.2)$$

where the  $f_{ABC}$  are the structure constants of SU(3), defined by the commutation relation of the generators:

$$[t^A, t^B] = i f_{ABC} t^C \quad (2.3)$$

$$[T^A, T^B] = i f_{ABC} T^C. \quad (2.4)$$

For the calculation of interaction cross sections, often the following relations are needed:

$$\sum_A t_{ab}^A t_{bc}^A = C_F \delta_{ab}, \quad C_F = \frac{N^2 - 1}{2N} \quad (2.5)$$

$$\text{Tr } T^C T^D = \sum_{A,B} f^{ABC} f^{ABD} = C_A \delta^{CD}, \quad C_A = N \quad (2.6)$$

The Casimir operators  $C_F = \frac{4}{3}$  of the fundamental representation and  $C_A = 3$  of the adjoint representation for  $N = 3$  are often also called color factors and introduce different behaviour of quarks and gluons in strong processes.

While quarks and gluons constitute the microscopic degrees of freedom in QCD, they have never been observed as individual particles but only as constituents of (colorless) hadrons. Although there is no analytical solution to this problem yet, a widely accepted explanation, supported by numerical calculations, is given by the theory of color confinement [1]. As gluons are subject to self-interactions, the energy density between two quarks becomes constant at large distances, resulting in a linearly increasing potential (cf. Fig. 2.1). Accordingly, increasing amounts of energy would be necessary to separate two colored objects to increasing distances. Thus, quarks and gluons are grouped into colorless hadrons, preventing long range color fields from forming.

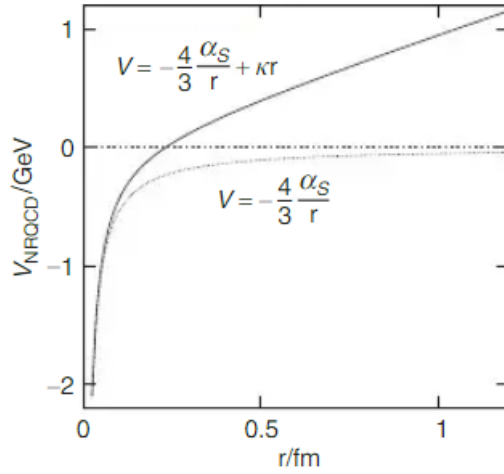


Figure 2.1: Qualitative representation of the non-relativistic QCD potential between a quark and an anti-quark, where  $\alpha_s = 4\pi g_s^2 = 0.2$  and  $\kappa = 1 \text{ GeV/fm}$  were assumed [1]

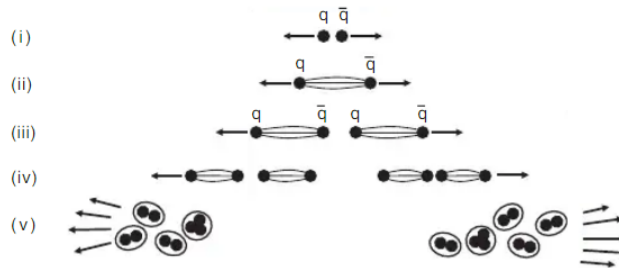


Figure 2.2: Schematic jet production, shown in the center of mass frame of the partons [1]

The consequence of color confinement for fundamental processes like  $2 \rightarrow 2$  parton scattering (with high momentum transfer) is shown schematically in Fig. 2.2. Momentum conservation in the center of mass system implies back-to-back scattering of the two emerging particles [1]. As they separate with high velocities, the energy density between them increases, until it is high enough to produce an additional parton-anti-parton pair. This process is repeated until the energies of the particles fall below the so called hadronization scale  $\mathcal{O}(1 \text{ GeV})$ . Then the partons get confined within hadrons and the original two hard scattered partons emerge as sprays of particles. These are called jets.

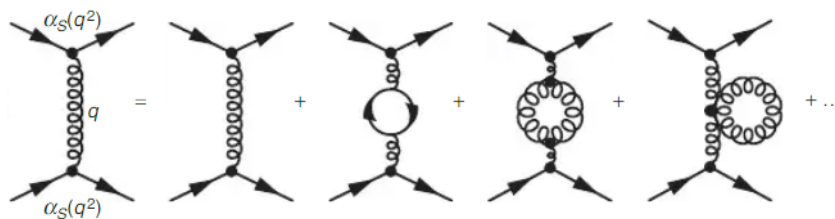


Figure 2.3: Schematics of QCD renormalization [1]

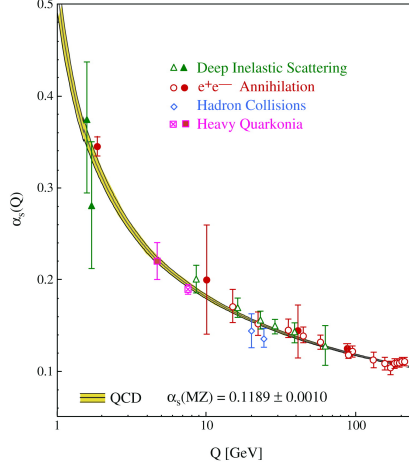


Figure 2.4: The running coupling constant  $\alpha_s$ , measured in different processes. The QCD calculation using the reference value  $\mu = m_Z$  is depicted as yellow band. [19]

Another consequence of the gluon self-interaction is its effect on renormalization and the running strong coupling constant, generally defined as  $\alpha_s = g_s^2/4\pi$  [5]. Similar to QED, quantum loops are present in next-to-leading order, next-to-next-to-leading order,... Feynman diagrams. Since there is no upper limit for higher order corrections, they lead to diverging integrals in the calculation of interaction cross sections.

Renormalization is the process of absorbing these higher order quantum loop corrections into the definition of the coupling constant, schematically shown in Fig. 2.3. The procedure follows the renormalization group equation [5]

$$Q^2 \frac{\partial \alpha_s}{\partial Q^2} = \beta(\alpha_s) \quad (2.7)$$

where the  $\beta$  function is the perturbation series of  $\alpha_s$ :

$$\beta(\alpha_s) = -b\alpha_s^2(1 + b'\alpha_s + b''\alpha_s^2 * \mathcal{O}(\alpha_s^3)). \quad (2.8)$$

The definitions of the coefficients  $b, b', b''$  can be found in [5].  $Q^2$  is the scale of the process  $\alpha_s$  has to be determined for. By introducing a reference scale  $\mu$ , Eq. (2.8) can be solved to obtain

$$\alpha_s(Q^2) = \frac{\alpha_s(\mu^2)}{1 + \alpha_s(\mu^2)bt}, \quad t = \ln \frac{Q^2}{\mu^2} \quad (2.9)$$

Fig. 2.4 shows  $\alpha_s$  at different scales, measured in different processes. The QCD calculation using the measured reference value at  $\mu = m_Z$  is depicted as well. At high energy scales,  $\alpha_s$  is small, allowing for a perturbative treatment of strong processes. However, it diverges for small energies, below the QCD scale  $\Lambda_{\text{QCD}} \approx 0.2 \text{ GeV}$ . This phenomenon is called asymptotic freedom. In the following section, consequences of asymptotic freedom are discussed in more detail.

## 2.2 The quark-gluon plasma and heavy-ion collisions

Due to asymptotic freedom, there are different states of hadronic matter. When hadrons are compressed or heated, a phase transition occurs upon reaching a maximum, critical temperature, first defined by [20]. It is expected that at sufficiently high temperatures and/or hadronic density the quarks and gluons bound in hadrons become deconfined [6, 7] and migrate into a strongly bound state of matter wherein they behave like quasi-free particles. This state of matter is called the Quark-Gluon Plasma (QGP). According to current understanding, up to a few microseconds after the Big Bang the universe was in this state [21, 22]. Therefore, the QGP constitutes a powerful tool to both study strong interactions and improve our understanding of matter and the evolution of the universe. The QGP can be created in ultra-relativistic collisions of heavy nuclei [23], which provides the possibility to study the fundamental degrees of freedom of QCD under laboratory conditions. Currently, heavy-ion collisions are performed at the Brookhaven National Laboratory's Relativistic Heavy-Ion Collider (RHIC)[24–26], at the GSI[27] in Darmstadt and at the Large Hadron Collider (LHC)[28] in Geneva. There, ALICE [29] is the dedicated heavy-ion detector.

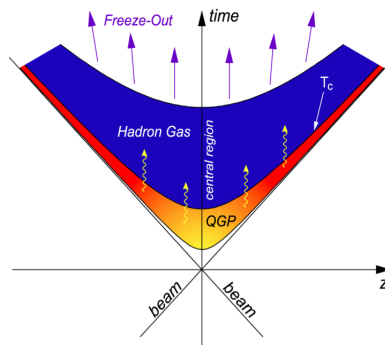


Figure 2.5: Schematic evolution of a heavy-ion collision [30]

In Fig. 2.5 the space-time evolution of such a heavy-ion collision is shown. At  $t = z = 0$  the two beams collide, initiating hard and soft collisions (i.e collisions with both large and small momentum transfer) of the beams partons. After an initial time of  $\tau_0 \sim 1$  fm the deconfined quarks and gluons thermalize and form a QGP. The QGP created in ultra-relativistic heavy-ion collisions is short lived, with a life time of  $\sim 10$  fm/c [9]. With progressing time, the medium expands and cools down. When the critical temperature  $T_c = 156 \pm 1.5$  MeV [10] is reached, quarks and gluons again become confined within hadrons. At this stage, the hadron abundancies are fixed. The hadron gas further expands and cools down, until elastic collisions between the hadrons stop. This is the kinetic freeze out, that determines the kinematics of the particles ultimately measured in detectors.

The collision geometry, for example the distribution and number of particles participating, can be modelled with the Glauber model [31], which is explained below, following [31]. Taking input parameters like the nuclear charge density and inelastic nucleon-nucleon cross section  $\sigma_{\text{inel}}^{\text{NN}}$ , it calculates the number of interactions. The colliding nuclei can be described by the Woods-Saxon distribution

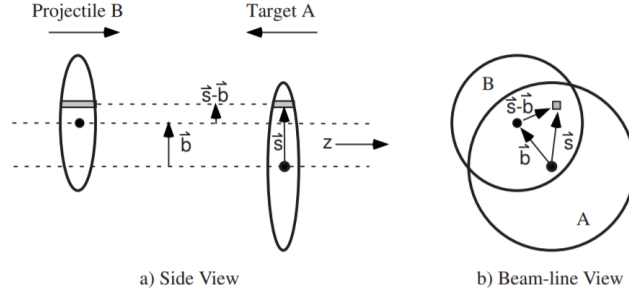


Figure 2.6: Schematics of the optical Glauber geometry, as seen along beam direction (a) and in the transverse plane (b)[31].

$$\rho(r) = \rho_0 \frac{1 + w(r/R)^2}{1 + \exp\left(\frac{r-R}{a}\right)}, \quad (2.10)$$

where  $\rho_0$  is the density at the nucleus center,  $R$  is the radius of the nucleus and  $a$  is a measure of the surface thickness of the nucleus.  $w$  quantifies the deviation of the nucleus shape from a perfect sphere.

In Fig. 2.6 a schematic depiction of the Glauber model geometry can be seen. The probability that a nucleon in nucleus A is found in a tube positioned relative to the nucleus center by a displacement  $\vec{s}$  is given by

$$\hat{T}_A(\vec{s}) = \int \hat{\rho}_A(\vec{s}, z_A) dz_A, \quad (2.11)$$

where  $\hat{\rho}_A(\vec{s}, z_A)$  is the probability per unit area. Taking a second nucleus, B, displaced to A by the impact parameter  $\vec{b}$ , the respective tube is located at  $\vec{s} - \vec{b}$ . When the nuclei collide, both tubes overlap and the nucleons contained within interact. The probability for nucleons from both A and B to be located the overlap-tube is then given by  $\hat{T}_A(\vec{s})\hat{T}_B(\vec{s} - \vec{b})$  and consequently, by summing all possible tube positions,

$$\hat{T}_{AB}(\vec{b}) = \int \hat{T}_A(\vec{s})\hat{T}_B(\vec{s} - \vec{b}) ds^2. \quad (2.12)$$

$\hat{T}_{AB}$  is called “thickness function”. The probability that one interaction occurs in the overlap-region is obtained by multiplying  $\hat{T}_{AB}$  with  $\sigma_{\text{inel}}^{\text{NN}}$ . Assuming  $N_A$  nucleons in nucleus A and  $N_B$  nucleons in nucleus B, the probability for  $n$  collisions is given by

$$P(n, \vec{b}) = \binom{N_A N_B}{n} \left[ \hat{T}_{AB}(\vec{b}) \sigma_{\text{inel}}^{\text{NN}} \right]^n \left[ 1 - \hat{T}_{AB}(\vec{b}) \sigma_{\text{inel}}^{\text{NN}} \right]^{N_A N_B - n} \quad (2.13)$$

and the total number of collisions by

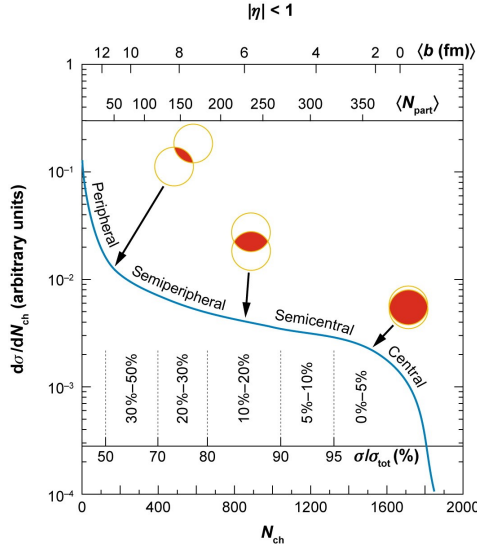


Figure 2.7: Schematics of the determination of  $N_{\text{part}}$  using the total inclusive charged-particle multiplicity as an observable [31].

$$N_{\text{coll}}(\vec{b}) = \sum_{n=1}^{N_A N_B} n P(n, \vec{b}) = N_A N_B \hat{T}_{AB}(\vec{b}) \sigma_{\text{inel}}^{\text{NN}}. \quad (2.14)$$

The number of nucleons that actually take part in interactions (called number of participants or wounded nucleons) can be estimated by adding the wounded nucleons from nucleus A and B:

$$N_{\text{part}}(\vec{b}) = N_A \int \hat{T}_A(\vec{s}) \left\{ 1 - \left[ 1 - \hat{T}_B(\vec{s} - \vec{b}) \sigma_{\text{inel}}^{\text{NN}} \right]^{N_B} \right\} ds^2 + N_B \int \hat{T}_B(\vec{s} - \vec{b}) \left\{ 1 - \left[ 1 - \hat{T}_A(\vec{s}) \sigma_{\text{inel}}^{\text{NN}} \right]^{N_A} \right\} ds^2 \quad (2.15)$$

In experiments,  $N_{\text{coll}}$  and  $N_{\text{part}}$  cannot be measured directly. To be able to interpret experimental data in terms of Glauber modelling, Glauber distributions of wounded nucleons are compared to distributions of accessible observables like e.g. the charged particle multiplicity [32]. The measured observable is connected to the number of participants, usually in centrality percentile classes. The principle of mapping observables to Glauber variables is shown in Fig. 2.7. Events with low impact parameter, the “central events”, have high multiplicities. They are usually denoted by e.g. (0-5) % or (0-10) % centrality. Events with for example (30-50) % centrality are “peripheral events”. They are characterized by a large impact parameter and therefore low multiplicity. The detailed process of determining the centrality percentile for example in ALICE is described in [32].

The centrality of a heavy-ion collision, and therefore shape of the overlap region, influences the azimuthal distribution of the measured particles [33]. In peripheral events,

a pressure gradient develops in the almond-shaped overlap region. Due to the resulting momentum anisotropy, particles get boosted predominantly into the direction of the event plane [33–37], which is defined by the vector connecting the centers of the colliding nuclei and the beam direction. For central events this effect decreases, since the overlap region is roughly circular and the pressure gradient is smaller compared to peripheral collisions.

As discussed above, the QGP constitutes an excellent system to probe fundamental properties of QCD. However, the QGP itself is not directly accessible. Measurements and conclusions have to be made from the hadronized particles stemming from the collision. In the next chapter, a possible observable to measure characteristics of the QGP is introduced.

# Chapter 3

## Jets as a probe of the QGP

The state of the QGP, as described in the previous chapter, has a variety of characterizing properties such as its viscosity, critical temperature or interaction mechanisms. Jets are an effective probe to explicitly study the interaction properties of the QGP [8]. Since jet production occurs at high momentum transfer, asymptotic freedom allows for a perturbative calculation of its cross section which makes jets theoretically well accessible. Furthermore, as mentioned in Section 2.1, high momentum processes are directly coupled to the microscopic degrees of freedom of QCD, making jets a suitable probe for those. In heavy ion collisions, jets are produced well before the medium thermalizes ( $\tau \lesssim 0.1$  fm/c) and therefore traverse it completely while departing from their production point. By comparing jets which have been modified by their interactions with the QGP to jets which fragment in vacuum one therefore gains insight into the interaction properties of the QGP. In this chapter a general overview of jet production and evolution is given, followed by the discussion of possible medium modifications induced by a QGP. In the last section, possibilities to measure medium modifications with jets are discussed.

### 3.1 Jet production in hadronic collisions

Jets are produced in hadronic collisions by scatterings with high momentum transfer  $Q^2$  (“hard” scattering)[8], cf. Section 2.1. As the factorisation theorem states, the calculation of the complete process can be split into one perturbative and two non-perturbative parts. Therefore the differential cross section for the production of a hadron  $h$  in the collision of nuclei  $A$  and  $B$  reads

$$d\sigma_{AB \rightarrow h}^{\text{hard}} = f_{a/A}(x_1, Q^2) \otimes f_{b/B}(x_2, Q^2) \otimes d\sigma_{ab \rightarrow c}^{\text{hard}}(x_1, x_2, Q^2) \otimes D_{c \rightarrow h}(z, Q^2). \quad (3.1)$$

A schematic representation of the theorem is shown in Fig. 3.1. The single parts are explained in the following.  $f_{a/A}(x_1, Q^2)$  and  $f_{b/B}(x_2, Q^2)$  are the parton distribution functions (PDFs) of the two colliding nuclei. They give the probability to find a parton of flavor  $a(b)$  in  $A(B)$  carrying a momentum fraction  $x_1(x_2)$  of the total momentum. The PDFs are non-perturbative and have to be measured, e.g. in electron-nucleus scattering experiments.

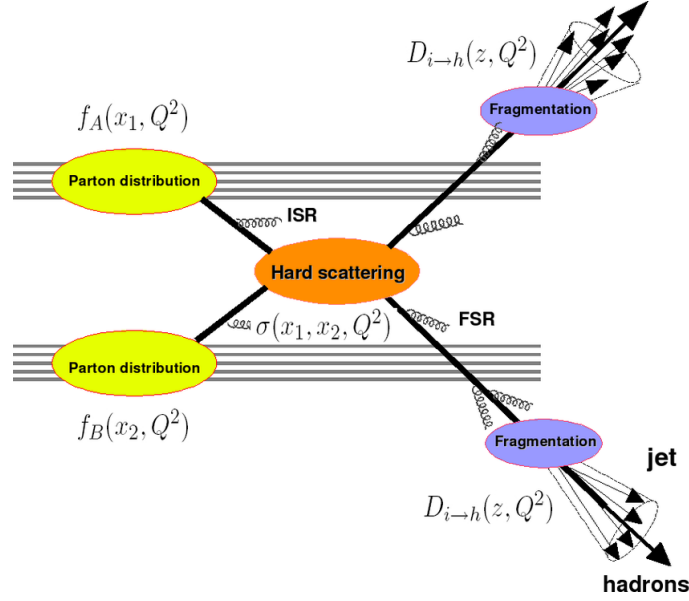


Figure 3.1: Schematic representation of the factorisation theorem in dijet production [8].

$\sigma_{ab \rightarrow c}^{\text{hard}}(x_1, x_2, Q^2)$  is the production cross section of a parton  $c$  in the scattering of the partons  $a$  and  $b$ . As the scatterings take place well above the QCD scale  $\Lambda_{\text{QCD}} \approx 0.2 \text{ GeV}$ , it can be calculated using perturbative QCD. The fragmentation function  $D_{c \rightarrow h}(z, Q^2)$  gives the probability for parton  $c$  to fragment into the hadron  $h$  carrying the fraction  $z$  of  $c$ 's momentum. Like the PDFs, the fragmentation function is not perturbatively calculable but has to be measured. Electron-positron collisions with hadronic final states are commonly used.

The outgoing partons of the hard scattering possess a high, defined as the virtual mass squared. In subsequent processes, the partons emit gluons and/or split into quark–anti-quark pairs and thereby reduce their virtuality. The influence of these processes on the partonic fragmentation functions is described by the Dokshitzer–Gribov–Lipatov–Altarelli–Parisi (DGLAP) equations [38–41]. Their evolution is given by [5, 42]:

$$\frac{\partial D_{q \rightarrow h}(z, Q^2)}{\partial \ln Q^2} = \frac{\alpha_s}{2\pi} \int_z^1 \frac{dx}{x} \left[ P_{qq}(x) D_{q \rightarrow h}\left(\frac{z}{x}, Q^2\right) + P_{gq}(x) D_{g \rightarrow h}\left(\frac{z}{x}, Q^2\right) \right] \quad (3.2)$$

$$\begin{aligned} \frac{\partial D_{g \rightarrow h}(z, Q^2)}{\partial \ln Q^2} = \frac{\alpha_s}{2\pi} \int_z^1 \frac{dx}{x} \left[ P_{qg}(x) \sum_q \left\{ D_{q \rightarrow h}\left(\frac{z}{x}, Q^2\right) + D_{\bar{q} \rightarrow h}\left(\frac{z}{x}, Q^2\right) \right\} \right. \\ \left. + P_{gg}(x) D_{g \rightarrow h}\left(\frac{z}{x}, Q^2\right) \right] \quad (3.3) \end{aligned}$$

The DGLAP equations describe the progression of the fragmentation functions with changing virtuality. Integral parts are the (regularized) Altarelli-Parisi splitting functions  $P$ , whose form are specific to the underlying process. The subscript  $P_{ab}$  is defined by the process  $ab \rightarrow c$ , where the nature of  $c$  is determined via  $a$  and  $b$ . The corresponding functions for the different splittings of quarks and gluons can be found in [5].

Depending on the evolution of the fragmentation functions of the initial partons, various final hadronized states can be reached.

For implementation of parton showers in Monte Carlo (MC) simulations, a probabilistic formulation is needed. For that purpose, the DGLAP equations are usually reformed by using the Sudakov form factor, defined as [5]:

$$\mathcal{S}_i(Q^2) \equiv \exp \left[ - \sum_j \int_{Q_0^2}^{Q^2} \frac{dQ'^2}{Q'^2} \int dx \frac{\alpha_s}{2\pi} \hat{P}_{ji}(x) \right], \quad i, j \in \{q, g\} \quad (3.4)$$

With the form factor, the probability that no resolvable radiation is emitted from a parton evolving from scale  $Q_0^2$  to scale  $Q^2$ , is defined. Substitution of Eq. (3.4) into Eqs. (3.2) and (3.3) and integration yields

$$D_{i \rightarrow h}(z, Q^2) = \mathcal{S}_i(Q^2) D_{i \rightarrow h}(z, Q_0^2) + \sum_j \int_{Q_0^2}^{Q^2} \frac{dQ'^2}{Q'^2} \frac{\mathcal{S}_i(Q^2)}{\mathcal{S}_i(Q'^2)} \int_z^1 \frac{dx}{x} \hat{P}_{ji}(x) D_{j \rightarrow h}\left(\frac{z}{x}, Q'^2\right), \quad i, j \in \{q, g\} \quad (3.5)$$

Eq. (3.5) is then implemented in a MC framework, where parton showers according to the fragmentation function are generated.

## 3.2 Jet quenching

When the partons from the hard scattering do not simply evolve in vacuum, like described in the previous section, but traverse a strongly interacting medium like a QGP, they become subject to additional interactions. This results in energy loss of the hard partons or rather a energy/momentum transfer from the parton to the medium.

While jet modification by emission of synchrotron, Cherenkov and transition radiation is in principle possible, the two main effects are given by elastic scatterings with the medium, i.e. collisional energy loss, and gluon bremsstrahlung [8], cf. Fig. 3.2.

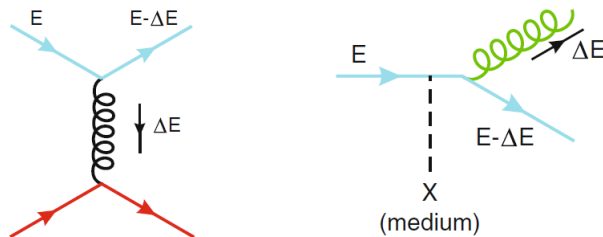


Figure 3.2: Collisional (left) and radiative (right) energy loss [8].

### Collisional energy loss

Collisional energy loss for light quarks/gluons and heavy quarks were described first by Bjorken [43] and Braaten-Thoma [44], and later improved in various extensions. It is the dominant process at low particle momenta and for high particle masses. The average energy loss per scattering in a plasma with temperature  $T$  can be calculated by integrating the differential scattering cross section over the range of transferred momentum [8]:

$$\langle \Delta E_{\text{coll}}^{\text{scat}} \rangle = \frac{1}{\sigma T} \int_{t_{\text{min}}}^{t_{\text{max}}} t \frac{d\sigma}{dt} dt. \quad (3.6)$$

The differential scattering cross section is, to leading order, given by

$$\frac{d\sigma}{dt} = C_R \frac{4\pi\alpha_s^2(t)}{t^2}. \quad (3.7)$$

The color factors for quark-quark, quark-gluon and gluon-gluon scattering are  $C_R = \frac{4}{9}, 1, \frac{9}{4}$ .

From Eq. (3.6) one obtains the energy loss per unit path-length:

$$-\frac{dE_{\text{coll}}}{dx} \Big|_{\text{light}q,g} = \frac{C_R}{4} \alpha_s(ET) m_D^2 \ln \left( \frac{ET}{m_D^2} \right), \quad (3.8)$$

$$-\frac{dE_{\text{coll}}}{dx} \Big|_{\text{heavy}q} = \frac{dE_{\text{coll}}}{dx} \Big|_{\text{light}q} - \frac{2\pi C_R T^2}{9} \left[ \alpha_s(m_q^2) \alpha_s(ET) \ln \left( \frac{ET}{m_q^2} \right) \right]. \quad (3.9)$$

When the energy loss per unit path-length is integrated over a plasma with finite size  $L$ , dependence of the total energy loss on the path-length traversed by the parton is obtained. Since the differential energy loss is not dependent on the path, the total energy lost increases linearly with  $L$ .

### Radiative energy loss

For low particle masses and high momenta, gluon radiation is the main process of energy loss [8]. Depending on the energy  $\omega$  of the radiated gluon off a parton with energy  $E$ , the gluon spectrum takes a different form [45]. Therefore, the radiation is subdivided into three different regimes. For very soft radiation –  $\omega < \omega_{\text{BH}} \sim \lambda m_D^2$ , where  $\lambda$  is the mean free path and  $m_D$  is the Debye mass of the medium – in the Bethe-Heitler (BH) regime, incoherent radiation is emitted at each scattering site. For very energetic emissions in the factorization regime,  $\omega_{\text{fact}} < \omega < E$  the whole medium acts as a single scattering site. The intermediate gluon energy region is called the Landau-Pomeranchuk-Migdal (LPM) regime. For gluon emissions in this regime, radiation is emitted coherently for scattering sites within one coherence length. The gluon spectrum for each regime is given by [45]

$$\omega \frac{d^2 I}{d\omega dx} = \begin{cases} \frac{\alpha_s}{\lambda} & \omega < \omega_{\text{BH}} \\ \frac{\alpha_s}{\lambda} \sqrt{\frac{\lambda m_D^2}{\omega}} & \omega_{\text{BH}} < \omega < \omega_{\text{fact}} \\ \frac{\alpha_s}{L} & \omega_{\text{fact}} < \omega < E \end{cases} \quad (3.10)$$

for a finite medium size  $L$ .

To obtain the total energy loss by radiation, the gluon spectrum is integrated over the complete energy range and the whole medium:

$$\Delta E = \int_0^E d\omega \int_0^L dx \omega \frac{d^2 I}{d\omega dx} \sim \alpha_s \frac{m_D^2 L^2}{\lambda}. \quad (3.11)$$

Hence, contrary to collisional energy loss, the energy loss by gluon radiation is proportional to  $L^2$  in a static medium.

In MC simulations, the energy loss mechanisms described above enter the jet development process by way of medium modified fragmentation functions, cf. eg. [46]. Experimentally, this jet quenching phenomenon can be observed as a suppression of high transverse momentum jets. In the following a possible way to measure jet quenching is described.

### 3.3 Two-particle and 2+1 correlations

In heavy-ion collisions, high multiplicities are characteristic, stemming from the hadronization of both the hard scattered partons (i.e. the jets) and the thermalized medium. The presence of the underlying event makes the reconstruction of jets a highly complex and difficult task, since it is basically impossible to distinguish between soft fragments of the jet and hadronized medium particles. Especially at low jet momenta, where the energy loss is most distinct, jets cannot be identified on an event-by-event basis.

To circumvent this complication, jets can be studied on a statistical basis with two-particle angular correlation functions [47, 48]. In this approach, a particle within a selected momentum range (trigger particle) is used as a proxy for the jet. Then the angular distances  $\Delta\varphi$  and  $\Delta\eta$ , the relative azimuthal angle and the relative pseudorapidity, of the trigger to all other particles in the event (associated particles) are calculated. A more detailed description of the procedure can be found in Chapter 5. The resulting correlation function is shown in Fig. 3.3. Since the particles of a jet are located spatially close to the trigger particle, the peak observed at  $\Delta\varphi = 0 = \Delta\eta$ , the near-side peak, corresponds to the jet associated with the trigger particle. Due to the scale of the  $z$ -axis, the top of the near-side peak is cut off in the image. The recoil jet, emitted back-to-back in azimuth, is visible at  $\Delta\varphi = \pi$ . Since the separation in  $\eta$  depends on the momentum fractions taken by the scattering partons, the away-side peak is smeared in  $\Delta\eta$ .

When comparing the yield  $Y$  of the peak in heavy ion collisions to the yield in pp collisions, the modification of the jets can be studied with the observable

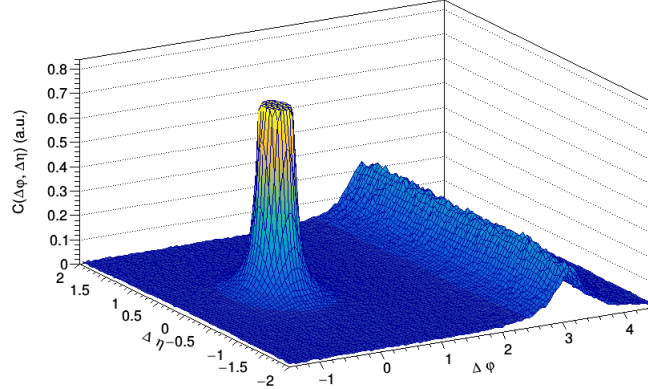


Figure 3.3: Correlation function of a trigger particle with the associated particles, generated with a toy event generator. It includes the near-side peak at  $\Delta\varphi = 0 = \Delta\eta$  and the away-side at  $\Delta\varphi = \pi$ . The top of the near-side peak is cut by the  $z$ -axis scale.

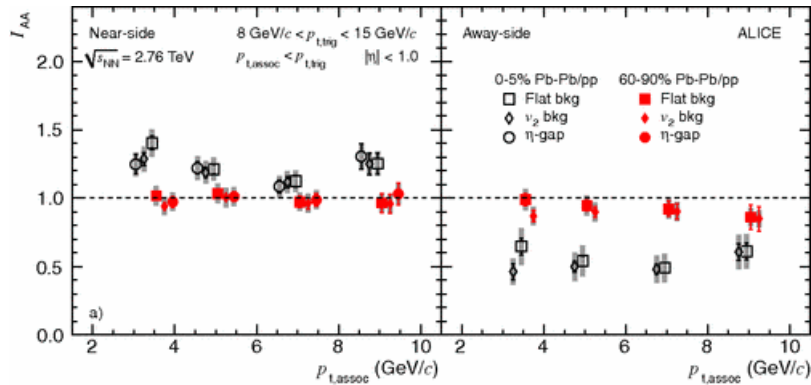


Figure 3.4:  $I_{AA}$  on the near (left) and away (right) side, for central and peripheral collisions. The medium modification is visible via a deviation of  $I_{AA}$  from unity [47].

$$I_{AA} = \frac{Y_{\text{PbPb}}}{Y_{\text{pp}}}. \quad (3.12)$$

An example for the measurement of  $I_{AA}$ , taken from [47], is shown in Fig. 3.4. The yield-ratio of PbPb collisions to pp collisions for different centrality bins is shown. The trigger condition  $8 < p_{T,\text{trig}} < 15 \text{ GeV}$  and different bins in  $p_{T,\text{assoc}}$  were chosen. The influence of in-medium interactions is clearly visible as an  $I_{AA}$  suppression on the away-side. On the near-side, an enhancement is observed, also indicating medium modifications.

As was discussed in the previous section, different in-medium path-lengths result in varying amounts of energy loss. Thus, the modification observed with the  $I_{AA}$  can be an indicator of the path-length traversed by the corresponding jet. As can be seen in Fig. 3.5, there is a strong suspicion that the emission angle relative to the event plane is related to the path-length [8]. Particles emitted transverse to the event plane had a

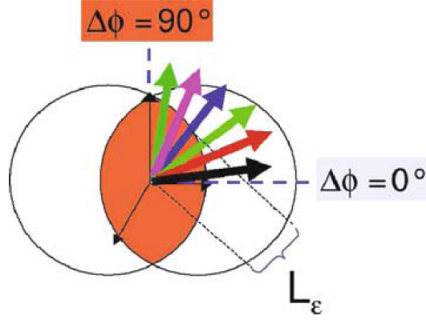


Figure 3.5: Schematic depiction of the path-length in the transverse direction, relative to the event plane [8].

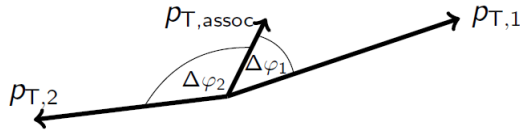


Figure 3.6: Schematics of 2+1 correlations

longer path-length than particles emitted in plane. Therefore, studies of modifications of correlation functions in combination with event plane studies constitute a promising way to study the path-length dependence of jet modifications.

The selection of a usually high trigger  $p_T$  potentially introduces a surface bias to the measurement [49], meaning that the jet was more likely to be produced at the surface of the medium. One can understand this in the way that a high  $p_T$  particle did not undergo many medium interactions (otherwise it would have lost more energy) and therefore had to be produced at the surface of the medium. However, the goal is to study the medium interactions of jets. Therefore, the recoil jet, located at  $\Delta\varphi = \pi$ , becomes an interesting observable. When the triggered jet only had a small path-length in the medium, the recoil jet had a correspondingly large path-length and therefore experienced a larger medium modification. Investigation of the recoil jet though is less precise than a similar analysis of the near-side jet, since the peak is smeared in  $\Delta\eta$ .

A possible way to study the away-side as well are 2+1 correlations [50]. In this method, two trigger particles – emitted back-to-back – are selected, see Fig. 3.6. The angular correlations are then calculated wrt. both trigger particles and filled into different histograms. In this way, both the jet and recoil jet form a distinct peak at  $\Delta\varphi = 0$  in their corresponding histogram and are accessible to detailed studies.

In the same way as the selection of the trigger condition in two-particle correlations potentially introduces a surface bias, it is theorized that one can influence the position of the production vertex of the dijet, and thereby the in-medium path-length of the jets, by modifying the trigger conditions in 2+1 correlations. It is the goal of this thesis to study the sensitivity of observables obtained from correlation functions to the path-length of jets. Since the approach via correlations is somewhat novel, the analysis is done using simulations. In this way, the controlled environment allows for the establishment of a baseline for the analysis of real data.



# Chapter 4

## The event generator JEWEL

As was stated in the previous chapter, the aim of this work is to study the sensitivity of correlation observables to path-length dependence of jet modification by the QGP. To provide a well found basis for future data analyses, the study in this thesis was done using Monte Carlo simulations. This chapter gives an introduction to the MC generator used, JEWEL, by illustrating the main physical concepts in Section 4.1. In Section 4.2 the parameters used are defined.

### 4.1 The physics of JEWEL

JEWEL [11–13] (Jet Evolution With Energy Loss) is a Monte Carlo simulator that models the phenomenon of jet quenching using four minimal assumptions in a simple medium model [51]. In the following, these assumptions, as well as the details of the medium model are explained.

#### 4.1.1 General principles

JEWEL describes jet evolution in the presence of a medium, the QGP produced in heavy-ion collisions. Consistently, perturbative QCD calculations are used to describe the processes of parton evolution and modification by the medium. The modifications included are elastic collisions with the constituents of the medium and gluon radiation, emitted as bremsstrahlung by the hard partons.

The event generation is done in three stages. First, the event is initialized by PYTHIA 6.4 [52] via generating a hard scattering and initial state radiation (ISR) off these hard partons. In case ISR is switched off, only the remnants of the incident nucleons are kept in the event for hadronization. Multi-parton interactions are switched off, as well as final state radiations (i.e. the production of a parton shower), since the latter part is done by the JEWEL main code. Accordingly, there is only one dijet system present per event. This represents a simplification of real experiments, where multiple jets can be produced in each collision. In the next step, the event is handed over to the JEWEL main code, where an impact parameter, based on the chosen centrality interval, and the transverse vertex position ( $z = 0$ ) of the hard scattering in the medium are chosen. With the impact parameter and the medium settings, specified by the user in an external parameter file,

a QGP-like medium is modelled. The medium model is described in Section 4.1.2, the parameters used to initialize the medium are listed in Section 4.2. After the initialization of the medium, final state parton showers are calculated. As a baseline and comparison to identify medium effects on jets, there is the possibility to run JEWEL without a medium ('in vacuum'). In this case the propagation is the usual virtuality ordered parton shower. When a medium is present, the parton shower is modified accordingly, cf. below. In the last step, after traversing the medium, the evolved partons and ISR are hadronized with PYTHIA, using the Lund string fragmentation. The medium in JEWEL is not included in the hadronization, hence there is no background contribution thereof.

In the following, the details of the parton evolution are discussed.

In the course of their evolution, the partons of the dijet system reduce their virtuality by subsequent splitting and radiation of gluons (cf. Section 3.1). The cross section  $\sigma_{n+k}$  for a  $n$ -parton final state with  $k$  additional partons resulting from the splitting and/or radiation is given by the cross section for the  $n$ -parton state, corrected with additional terms [51]:

$$d\sigma_{n+k} = \sigma_n \prod_{j=1}^k \frac{dt_j dz_j}{t_j} \frac{\alpha_s(k_{\perp,j}^2)}{2\pi} \hat{P}_j(z_j) \Theta(t_{j-1} - t_j) \quad (4.1)$$

The additional term(s) in Eq. (4.1) are characterized by the evolution parameter  $t$  (usually the virtuality), the momentum fractions  $z_j$  of the outgoing partons and the Altarelli-Parisi splitting functions  $\hat{P}_j(z_j)$  [5]. The theta function introduces a scale ordering of the emissions. To provide a suitable form for implementation in MC calculations, Eq. (4.1) is transformed in a probabilistic form, the Sudakov form factor [51]:

$$\mathcal{S}_a(t_h, t_c) = \exp \left( - \int_{t_c}^{t_h} \frac{dt}{t} \int_{z_{\min}}^{z_{\max}} dz \sum_b \frac{\alpha_s(k_{\perp}^2)}{2\pi} \hat{P}_{ba}(z) \right). \quad (4.2)$$

As before, it defines the probability that parton  $a$  does not emit (resolvable) radiation between two scales  $t_h$  and  $t_c$ .  $t_h$  is the starting scale, i.e. the virtuality of parton  $a$  before splitting.  $t_c$  is a cut-off value, i.e. a lower bound for the virtuality of parton  $a$  that excludes unresolvable soft radiation. In this implementation, the probability for each emission only depends on the current state of the parton, not on the chain of events leading there.

Modifications imposed by the modeled QGP contribute via the cross section. Here, the first of the four assumptions comes into play. In JEWEL, it is assumed that the partons of the hard scattering have sufficiently high energy to resolve the medium as single partons, i.e. single scattering centers. The cross section for distinct interactions with the medium therefore resembles the one of the initial hard scattering,

$$\sigma_i(E, T) = \int_0^{|\hat{t}|_{\max}(E, T)} \int_{x_{\min}(|\hat{t}|)}^{x_{\max}(|\hat{t}|)} dx \sum_{j \in \{q, \bar{q}, g\}} f_j^i(x, t) \frac{d\hat{\sigma}_j}{d\hat{t}}(x\hat{s}, |\hat{t}|), \quad (4.3)$$

where the  $t$ -channel cross section

$$\frac{d\hat{\sigma}}{d\hat{t}}(\hat{s}, |\hat{t}|) = C_R \frac{\pi\alpha_s^2 \hat{s}^2 + (\hat{s} - |\hat{t}|)^2}{\hat{s}^2 |\hat{t}|^2} \quad (4.4)$$

was chosen for JEWEL. However, unlike in the initial hard scattering where the partons were indeed part of the incoming nucleons, the PDFs in Eq. (4.3) cannot be taken to be the nucleon ones. Instead, special ‘partonic’ PDFs are used, determined from integrated DGLAP equations with medium modified splitting functions. The resulting PDFs can be found in [51].

A further difference of the cross section for hard parton – medium interaction to the hard scattering cross section lies within the scale of the process. To ensure the validity of a perturbative treatment, for hard scatterings a lower bound for the scattering scale is introduced (similar to the cut-off  $t_c$  mentioned above), resulting in a minimum  $p_T$  of the jets. However, soft (‘infra-red’) scatterings cannot be excluded from medium interactions in a consistent way. As can be seen immediately by looking at Eq. (4.4), the cross section diverges for  $\hat{t} \rightarrow 0$ , introducing the need for a special treatment of soft scatterings. This leads to the second assumption made in JEWEL: The matrix element can be regularized for the infra-red region, thus soft scattering can be included as continuation of the perturbative matrix element. In JEWEL the Debye screening mass  $\mu_D$  of the medium is used as regulator, resulting in the following cross section for the infra-red region, leading terms only:

$$\frac{d\hat{\sigma}}{d\hat{t}}(\hat{s}, |\hat{t}|) = C_R 2\pi\alpha_s^2 (|\hat{t} + \mu_D|) \frac{1}{(|\hat{t} + \mu_D^2|)^2} \quad (4.5)$$

$C_R = \frac{4}{9}, 1, \frac{9}{4}$  are the color factors for quark-quark, quark-gluon and gluon-gluon scatterings.  $\alpha_s$  is the strong coupling constant explained in Section 2.1.

The third assumption made in JEWEL takes care of the case where a second parton shower is initiated before the first/current parton shower has finished developing. In this case, the shower with shorter formation time,  $\tau = E/t$  where  $E$  is the energy of the hard parton,  $t$  the scale of the scattering, gets formed while the other one is discarded.

When the hard partons lose energy via bremsstrahlung, also the phases of the radiated gluons have to be taken into account. It was found that the scatterings of adjacent scattering points interfere destructively, leading to an overall diminished radiative energy loss of the parton. This is called the (non-abelian) Landau-Pomeranchuk-Migdal (LPM) effect. In [12], the probabilistic form of the LPM effect in eikonal kinematics was derived. It was found that radiations can be added coherently if further radiations take place during the formation time of the first radiation. If a radiation lies outside this formation time, they are added incoherently. In JEWEL it is assumed (fourth and last assumption) that this interpretation of the LPM effect is also applicable in non-eikonal kinematics.

### 4.1.2 Medium model

The medium in JEWEL is included via the (momentum-) space distribution of its scattering centers, i.e. of its partons. Therefore basically any model specifying these quantities can be used.

By default, a variation of the 1D Bjorken model [53] is used. In the Bjorken model, the medium expands only in the longitudinal direction, with a velocity of  $z/t$ , where  $z$  is the longitudinal position of medium cells and  $t$  describes the time that passed since the nuclei collided. The thermodynamics of the QGP is modelled as an ideal gas of quarks and gluons. In this way, only the temperature  $T$  is necessary as a describing parameter. By integrating the mean occupation number of gluons (Bose-Einstein distribution) and quarks (Fermi-Dirac distribution), one obtains the energy densities of the ideal, relativistic quantum gases:

$$\varepsilon_g = g_g \frac{\pi^2}{30} T^4 \quad (4.6)$$

$$\varepsilon_q = \frac{7}{8} g_q \frac{\pi^2}{30} T^4 \quad (4.7)$$

$$p_{g/q} = \frac{1}{3} \varepsilon_{g/q} \quad (4.8)$$

where  $g_g = n_{\text{spin}} \cdot n_{\text{colors}} = 2 \cdot 8 = 16$  and  $g_q = g_q + g_{\bar{q}} = 2 \cdot (n_{\text{spin}} \cdot n_{\text{colors}} \cdot n_{\text{flavor}}) = 2 \cdot (2 \cdot 3 \cdot N_f) = 12N_f$  are the degeneracies of quarks and gluons.

The energy density (and thereby momentum) of the QGP is obtained by combining the energy densities of quarks and gluons:

$$\begin{aligned} \varepsilon_{\text{QGP}} &= \left( g_g + \frac{7}{8} (g_q + g_{\bar{q}}) \right) \frac{\pi^2}{30} T^4 \\ &= \left( 16 + \frac{7}{8} \cdot 12N_f \right) \frac{\pi^2}{30} T^4 \end{aligned} \quad (4.9)$$

$$p_{\text{QGP}} = \frac{1}{3} \varepsilon_{\text{QGP}} \quad (4.10)$$

The transverse distribution is described in the Glauber picture. The initial energy density, calculated with Eq. (4.9) and the initial temperature  $T_i$ , is distributed according to the density of wounded nucleons:

$$\varepsilon(x, y, b, \tau_i) = \varepsilon_i \frac{n_{\text{part}}(x, y, b)}{\langle n_{\text{part}} \rangle (b=0)} \quad \text{with} \quad \langle n_{\text{part}} \rangle (b=0) \approx \frac{2A}{\pi R_A} \quad (4.11)$$

$b$  is the impact parameter of the ‘‘collision’’, the number of participant is calculated via the Glauber model, cf. Section 2.2:

$$\begin{aligned} n_{\text{part}}(x, y, b) &= T_A \left( \sqrt{(x-b/2)^2 + y^2} \right) \left[ 1 - e^{-\sigma_{\text{NN}}^{\text{inel}} T_A \left( \sqrt{(x+b/2)^2 + y^2} \right)} \right] \\ &\quad + T_A \left( \sqrt{(x+b/2)^2 + y^2} \right) \left[ 1 - e^{-\sigma_{\text{NN}}^{\text{inel}} T_A \left( \sqrt{(x-b/2)^2 + y^2} \right)} \right] \end{aligned} \quad (4.12)$$

Pressure, energy density and temperature of the QGP are assumed to be solely (proper) time dependent. In this picture the conservation of energy-momentum yields the following evolution equation [53]:

$$\frac{d\varepsilon}{d\tau} = -\frac{\varepsilon + p}{\tau} \quad (4.13)$$

With  $\varepsilon = 3p$  this results in a power law for the decrease of energy density and temperature with proper time:

$$\varepsilon(x, y, b, \tau) = \varepsilon(x, y, b, \tau_i) \left(\frac{\tau}{\tau_i}\right)^{-4/3}; \quad T(\tau) \propto \varepsilon^{1/4}(x, y, b, \tau_i) \left(\frac{\tau}{\tau_i}\right)^{-1/3} \quad (4.14)$$

The values used to initialize the medium, as well as the some of the settings for the main program are described in the following section.

## 4.2 Data simulation - parameter selection

A detailed description for using JEWEL is given in [54]. In this section, the parameters used to obtain the results in this thesis are listed.

For the analysis, dijet events at a c.m.s. energy of  $\sqrt{s_{NN}} = 2.76$  TeV per nucleon-nucleon pair were created. The nucleons are taken to be part of lead nuclei ( $A = 208$ ). Other parameters characterizing the parton showers, e.g. the QCD scale  $\Lambda_{QCD}$ , the infra-red cutoff of the parton showers or the transverse momentum range for the matrix element of the initial hard scattering, were kept at their default values.

The medium parameters are stored in separate files. The initial temperature  $T_i = 0.36$  GeV and initial time  $\tau_i = 0.6$  fm/ $c$  were kept at their default values as well. The critical temperature  $T_c$ , however, was set to the most recently found value of 0.156 GeV [10]. In this thesis, events in the (0-10) % and (50-60) % centrality percentiles were analyzed.

The output of JEWEL, printed in the HepMC 2 [55, 56] format, comprises in this JEWEL version the event number, scattering cross section, the number of incoming (always 2) and outgoing particles of the interaction vertex, as well as a listing of all hadronized particles and the incoming nucleons. The listing contains information about the particle ID, momentum components, energy and mass. The JEWEL source code was modified to also write out the two hard scattered partons and the interaction vertex, since this information is necessary for the analysis.

In the following chapters, the analysis and results obtained with JEWEL simulated data is described.



# Chapter 5

## Analysis and discussion

In this chapter, the analysis of JEWEL simulated data is described. The procedure was split into four main parts. In the first part, jets were characterized on a general basis. Next, the path-length of the hard scattered partons was characterized. In the next step, distributions were generated for trigger conditions similar to the ones usually used in correlation functions to draw a connection between the two. Finally, the findings were compared to observables obtained with angular correlation functions. The results of each part are discussed along the way. A summary of the conclusions is given in Chapter 6. Natural units ( $c = 1 = \hbar$ ) are used in the following.

### 5.1 Particle selection and jet reconstruction

The events generated with JEWEL, that are used for the final analysis, pass through several stages before they get selected.

Before any reconstruction, a fiducial pseudorapidity cut is applied to both the hard scattered partons and the final state particles. To match the limited acceptance of real life detectors like ALICE and STAR, the final state particles are required to have a pseudorapidity of  $|\eta_{\text{particles}}| < 1$ . An important part for the event selection is that the majority of the fragmented jet lies inside the acceptance. Therefore, both hard scattered partons are required to be within  $|\eta_{\text{parton}}| < 1 - R$ , where  $R$  is the characteristic jet radius chosen in the jet reconstruction. Furthermore only hadrons, both charged and uncharged, are selected for further reconstruction. Leptons and photons are excluded.

In the next step, jets were reconstructed with the remaining final state particles. For this, the FastJet [14, 15] package was used. FastJet provides a collection of the most commonly used jet clustering algorithms. In this work, the anti- $k_T$  algorithm in the  $p_T$ -scheme was used. The anti- $k_T$  sequential recombination is the most commonly used clustering algorithm in high-energy hadron collisions. It calculates the distance measures

$$d_{ij} = \min(1/p_{Ti}^2, 1/p_{Tj}^2) \frac{\Delta R_{ij}^2}{R^2}, \quad (5.1)$$

$$d_{iB} = 1/p_{Ti}^2 \quad (5.2)$$

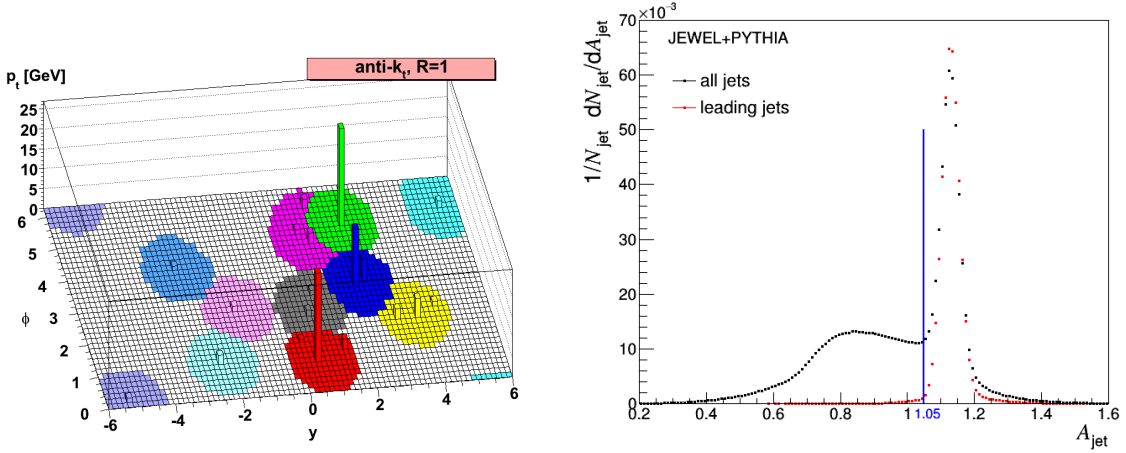


Figure 5.1: The left figure shows the reconstructed jet obtained with the anti- $k_T$  algorithm, taken from [57]. In the right figure, the jet areas of all jets obtained by applying the FastJet package with  $R = 0.6$  to JEWEL simulations are plotted in black. The red distribution is the area of the leading jets in the event. The peak was scaled to match the amplitude of the general distribution. Jets with an area  $A < 1.05$  (blue cutoff line) are excluded from further analysis.

of all particles among themselves and of each particle to the beam, respectively.  $\Delta R_{ij}^2 = (y_i - y_j)^2 + (\varphi_i - \varphi_j)^2$  is the squared spatial distance of the single particles, with  $y$  being the rapidity and  $\phi$  being the azimuthal angle of each particle.  $R$  is the jet radius already mentioned above. The algorithm then searches for the minimum of all  $d_{ij}, d_{iB}$ . If a  $d_{ij}$  is the minimum,  $i$  and  $j$  get recombined into a jet. In the  $p_T$ -scheme, the transverse momentum of the jet is determined by adding the transverse momenta of both recombined quantities. If  $d_{iB}$  is the minimum,  $i$  constitutes a final jet in the sense of the clustering and gets removed from the list. These steps are repeated until all particles from the original list are part of a jet.

The behavior of the anti- $k_T$  algorithm is illustrated in the left plot in Fig. 5.1. Due to the inverse momentum dependence of the measure, soft particles are more likely to be recombined with a hard particle than to cluster among themselves. A single hard particle (i.e. there is no other hard particle in its immediate neighbourhood  $\Delta R_{ij}^2 < 2R$ ) will result in a jet with perfect conical shape, containing all soft particles within  $R$ . For two or more hard particles within  $\Delta R_{ij}^2 < 2R$ , the area gets split between the jets, depending on the respective transverse momenta. The area and shape of soft jets very much depend on their surroundings.

The area of the jets is calculated by generating a uniformly distributed background of low  $p_T$  particles, the ghost particles. The area of each jet is then proportional to the number of ghosts accumulated by the respective jet. Since high  $p_T$  jets, i.e. the supposed fragments of the initial hard partons, are more likely to have a perfect cone shape, their area on average corresponds to  $A_{\text{jet}} = \pi R^2$ . The distribution of jet areas for the used  $R = 0.6$  in JEWEL simulations is shown in the right plot in Fig. 5.1, where the red distribution corresponds to the leading jets of the event. To reduce the contribution of fake jets in the analysis an area cut was applied to all jets. Only jets with  $A \geq 1.05$  were

kept in the event. Finally, events with less than two jets remaining after the area cut was applied were removed from the event record. The surviving events then were passed for the actual analysis, which is described in the following.

## 5.2 Characterization of jets and jet modification in JEWEL

The events, which passed the selection criteria described in the previous section, were analysed in different steps. This section describes the first of these steps, the general characterization of jets and jet modification in JEWEL.

In the description of JEWEL it was made clear that the contribution of the QGP, which complicates jet reconstruction and even jet definitions in real heavy-ion collision experiments, is not hadronized and written in the event record in the MC simulations. However, a direct matching between the initial hard partons and the reconstructed jets is still not well defined. Large initial state radiation, the fragmentation process and the quenching effects spread the jets originating from the single partons over a large area. Thus, the fragments of the partons are – in most of the cases – not contained within the scope of a single jet in the sense of a reconstruction algorithm. Accordingly, instead of singling out a specific jet, e.g. the one spatially closest to the hard parton, one has to look at distributions including all the reconstructed jets. However, in order to infer parton properties like the in-medium path-length from the jets, a certain mapping between jets and partons has to be maintained. This was done by identifying the parton hemisphere of each jet. Since the scattered partons are emitted back-to-back in azimuth and the fragmentation is boosted in their respective direction, the jets constituents are more probable to be contained within the hemisphere of their mother parton ( $\varphi_{\text{jet}} = \varphi_{\text{parton}} \pm \frac{\pi}{2}$ ) than to end up in the other one.

To be able to draw conclusions from distributions made with triggered jets, one has to be able to differentiate features specific to the respective trigger condition from behavior which is generally observed in jets in JEWEL. Therefore, jets and jet modification were quantified with the distributions of observables obtained from the reconstructed jets for different parton energies. In the characterization, both extreme cases were considered. The first of these cases is the fragmentation in vacuum, like that in pp collisions. The second one is the evolution of a parton in a medium with properties like a QGP in heavy-ion collisions with (0-10) % centrality and subsequent hadronization. In the following, the cases are often referred to as “vacuum case” and “medium case”. More peripheral collisions are expected to lie in between those two cases with regard to their characteristics.

### 5.2.1 Jet transverse momentum

The main characteristic to quantify the remaining parton momentum is the transverse momentum of the reconstructed jets. In the vacuum case, all transverse momentum is only transferred from mother to daughter particles and not to external medium particles. Therefore, the comparison of jet  $p_T$  to parton  $p_T$  in vacuum gives a measure, how well

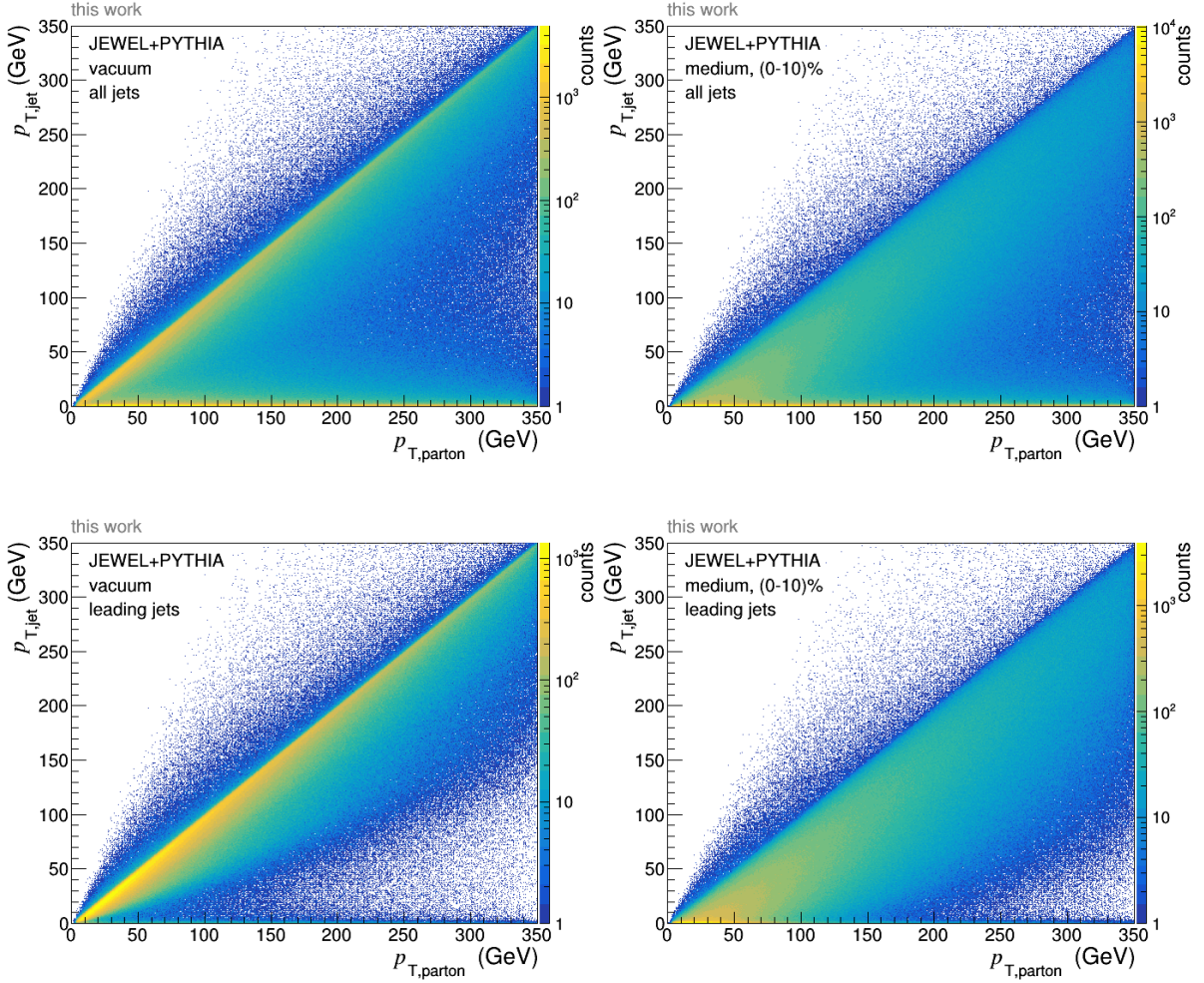


Figure 5.2: Distributions of the reconstructed jet transverse momenta vs. the transverse momentum of the parton located in the same hemisphere as the corresponding (leading) jet. The plots show the distributions for events in vacuum and in a medium with (0 – 10) % centrality.

the partons momentum can be captured by the jet reconstruction. By comparing the jet  $p_T$  to  $p_{T,\text{parton}}$  in the medium case, the momentum transfer is deducible. The resulting distributions can be seen in Fig. 5.2. The top row shows the transverse momentum of all jets in the same hemisphere as the parton, the bottom row the leading jet in each hemisphere. For the leading jets, the hemisphere of each parton was calculated and the jet with the largest transverse momentum in each hemisphere was selected. In Fig. 5.3 the profiles onto the  $x$ -axis, i.e. the mean jet  $p_T$  per parton  $p_T$ , of all distributions are plotted. As can be seen in the distributions both in vacuum and in medium, the main part of the partons momentum is captured by the leading jet. However, especially in the vacuum case it becomes clear that even with a comparatively large jet radius of  $R = 0.6$  the leading jet cannot capture all of the partons momentum. By reading off values from the profiles in Fig. 5.3 one can see that for a  $p_T = 300$  GeV parton,  $\sim 90\%$  of the momentum are contained in the leading jet, for a  $p_T = 50$  GeV parton it is  $\sim 80\%$ . The rest of the parton momentum is distributed amongst the other jet candidates. In the

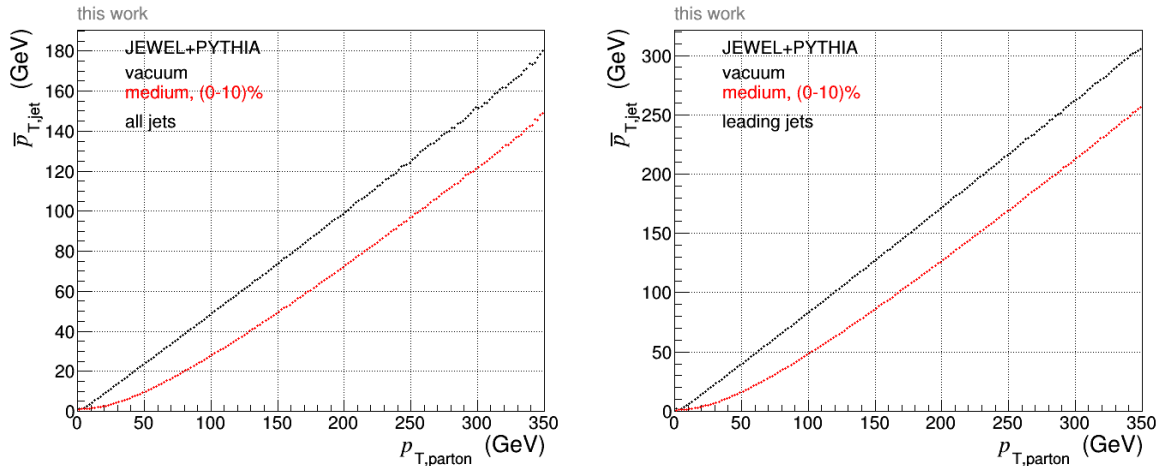


Figure 5.3: Mean jet  $p_T$  per parton  $p_T$ . On the left, the distributions for all jets, on the right the distributions for the leading jets in a partons hemisphere are plotted.

2D distributions for the leading jets in Fig. 5.2 a band of leading jets with almost zero momentum is visible. This is due to events, where the actual leading jet corresponding to the respective parton is cut away by the area cut or the  $\eta$  cut, when the fragments were scattered outside of the acceptance. Since the area calculation depends not only on the momentum of the jets, but also on the distribution and hardness of jets around the jet in question, it may happen in some events that the area of the leading jet is smaller than the cutoff value. Then, the next jet with highest momentum in the hemisphere gets selected as leading jet. In some cases, this jet has a momentum close to zero, resulting in the band in the 2D distributions. A possible way to reduce the inaccurate removal of leading jets in the vacuum case would be an additional maximum  $p_T$  for the jet to be removed. i.e. only jets which both have an area and  $p_T$  below the chosen cutoff value get removed. However, in the medium case, to maintain the comparability to real data analysis, the information about the exact momentum transfer was not used. With a cut on the transverse momentum one might cut away actual physics cases where the jet was quenched to almost zero momentum. Therefore, the events with very low  $p_T$  leading jets were kept in the analysis. The quenching effect becomes apparent when comparing the medium distributions to the vacuum ones. The distribution of sub-leading jets is similar in both cases. However, the distribution for the leading jets in medium extends to lower jet  $p_T$  for the same parton  $p_T$  when compared to the vacuum distribution. This extended spread is more dominant at parton momenta  $p_{T,\text{parton}} < 250$  GeV, indicating the decreasing influence of medium modifications at increasing parton energies. In the profiles of the leading jet distributions, one observes a decrease of jet momentum of  $\sim 20\%$  to  $\sim 60\%$  for parton momenta  $p_T = 300$  GeV and  $p_T = 50$  GeV respectively, when comparing the medium case to the vacuum case.

Analogous to the  $x$ -profiles above, Fig. 5.4 shows the spectra of (leading) jet  $p_T$  in different intervals of  $p_{T,\text{parton}}$ . The top row shows the spectra for all jets in each partons hemisphere, the bottom row shows the leading jets. In the vacuum case, a clear bump in  $p_{T,\text{jet}}$  around the value of  $p_{T,\text{parton}}$  is visible. In the distributions for all jets, the

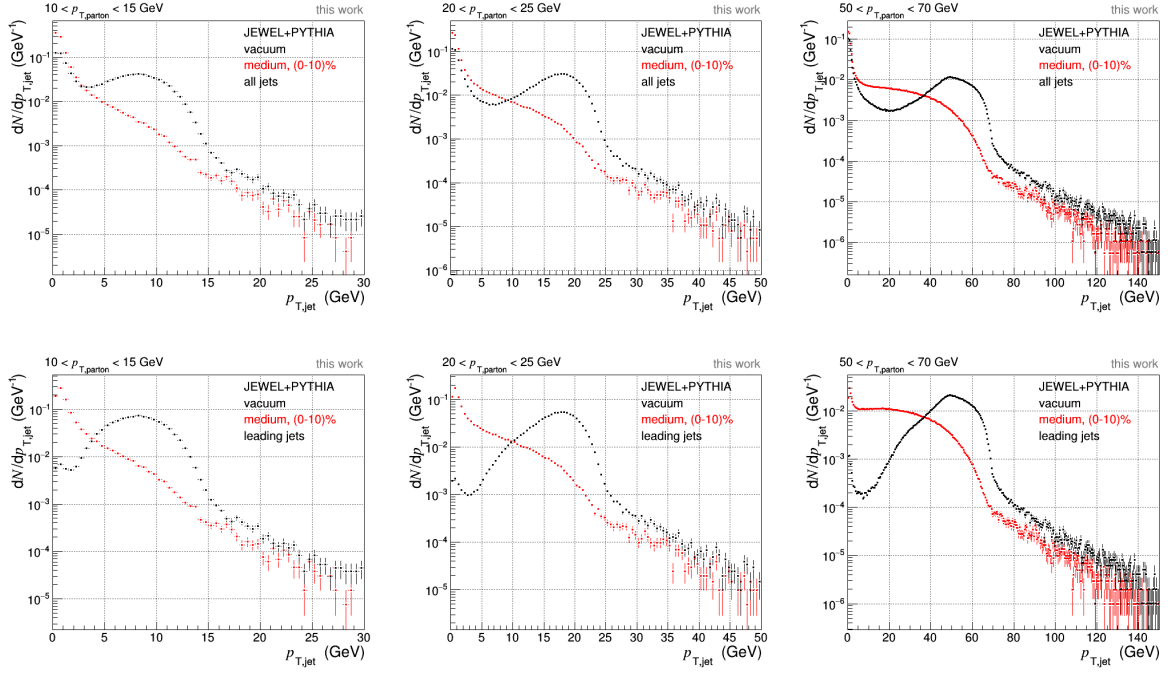


Figure 5.4: The top row shows the jet  $p_T$  spectra of all jets in a partons hemisphere in different ranges of the partons transverse momentum. In the bottom row, the spectra are shown for the leading jets for the same ranges in parton  $p_T$ .

sub-leading jets appear as exponentially declining contribution, superimposed with the leading jets distribution. The peak towards zero  $p_T$  in the leading jet distributions corresponds to the band of leading jets with very low  $p_T$  in the 2-dimensional distributions. As is visible for the medium case, the bump is washed out due to quenching, especially for the two lowest parton  $p_T$  intervals.

## 5.2.2 Average angular distance of the jets constituents to the jet axis

Another observable to quantify jets and jet quenching is the jet shape. In this analysis, this is expressed with the average angular distance of the jet constituents to their respective jet axis,  $\langle \Delta\varphi_{a(xis)} \rangle$ . The angular distance of the jet constituents to the jet axis is a measure for the fragmentation process. In the medium case, a deviation of  $\langle \Delta\varphi_a \rangle$  in comparison to the distribution in vacuum quantifies the diffusion happening in the medium.

The distributions of average angular distance versus parton  $p_T$  are shown in Fig. 5.5. The top row includes the distributions for all jets, the bottom row the leading jets of each partons hemisphere in vacuum and in a medium with (0-10)% centrality. The peak towards low parton  $p_T$  reflects the falling  $p_T$ -spectrum in hard scatterings. In the distributions for all jets, an edge at  $\langle \Delta\varphi_a \rangle = 0.3$  is observed. This edge is characteristic to the size of the chosen cone radius. The tilt in the 2-dimensional distributions indicates that jets with low transverse momentum fragment wider than jets with comparably

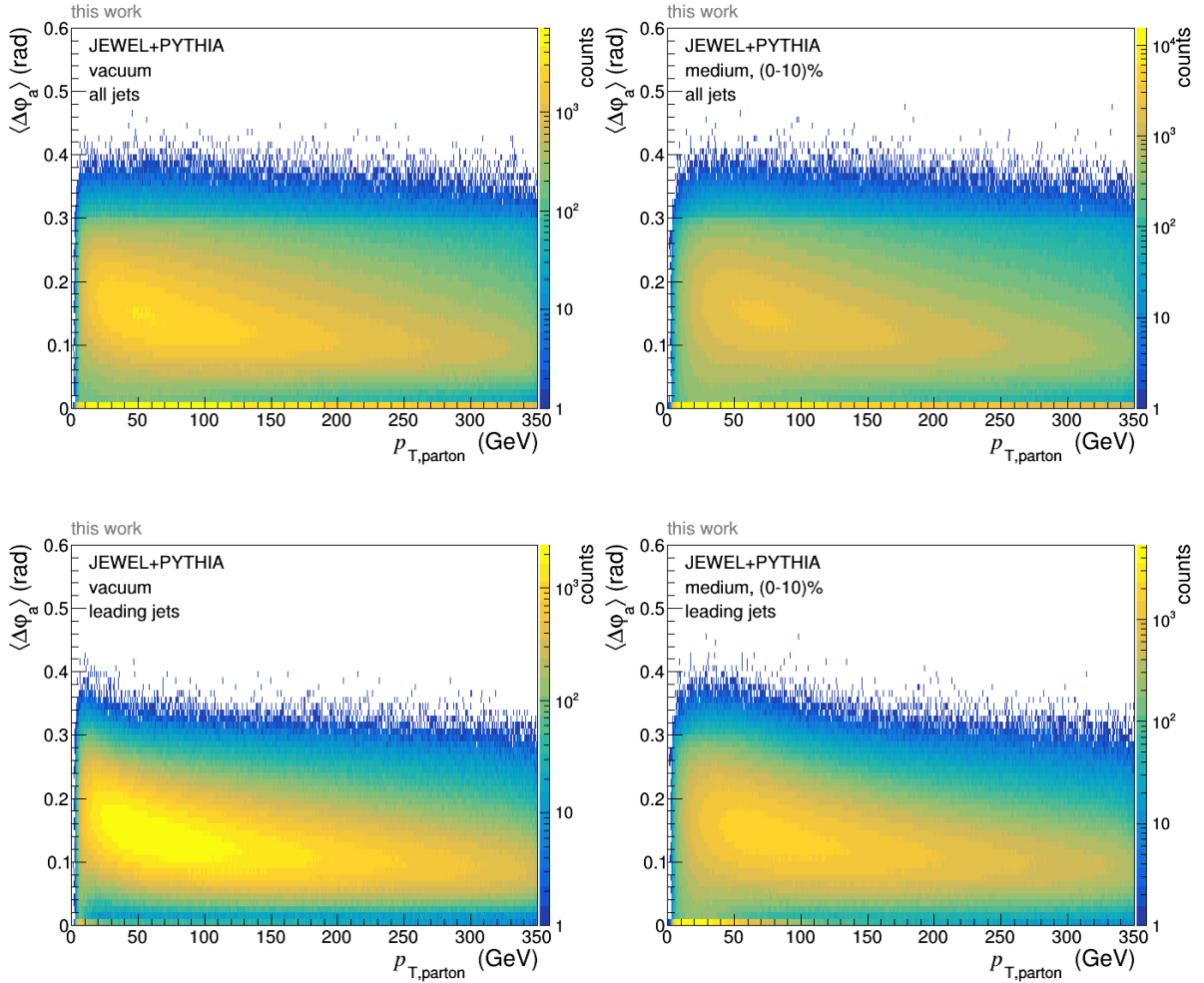


Figure 5.5: Average angular distance of the jet constituents to their respective jet axis. The top row shows the distribution for all jets, the bottom row shows the distributions for the leading jets in each partons hemisphere.

large transverse momentum. For a quantification of the different spreading at varying parton  $p_T$ , the profiles of these distributions are discussed below. In the lowest bin in  $\Delta\varphi_a$ , a peak is observed. By investigation it was found that this peak is caused either by highly energetic jets with few ( $< 10$ ) constituents that are close to the jet axis or by single particle “jets” with very low momentum.

Fig. 5.6 shows the profiles, i.e. the mean average angular distance per parton  $p_T$ . The peaks described above were excluded from the profile calculation. The profiles confirm that on average partons with high transverse momentum fragment over a smaller area than partons with a low transverse momentum. At transverse momenta  $p_{T,\text{parton}} \gtrsim 130$  GeV for jets in general and  $p_{T,\text{parton}} \gtrsim 180$  GeV for leading jets, the average angular distance of the jet constituents to the jet axis is on average equal in vacuum and for jets that traversed the medium. Below these values down to  $p_{T,\text{parton}} \approx 30$  GeV the constituents are on average farther away from the jet axis in events with a medium than in vacuum events. In the distributions of transverse momentum, Fig. 5.3, it was

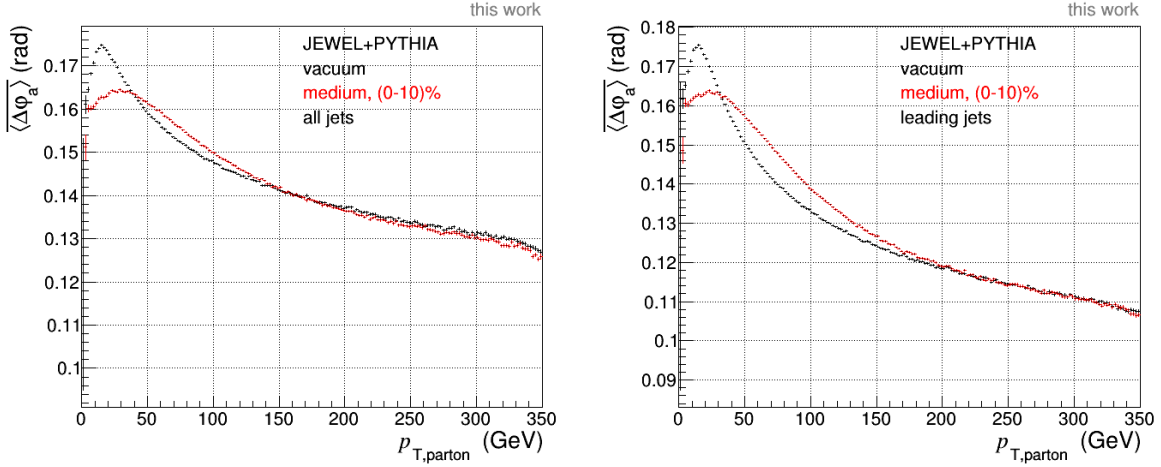


Figure 5.6: Mean average angular distance of the constituents of all (left) jets and the leading jets (right) of a parton hemisphere.

found that the quenching effect decreases relative to the increasing parton momentum. Applying the same logic to  $\langle \Delta\varphi_a \rangle$ , it can be concluded that the fragments of the parton are diffused inside the simulated QGP and that this effect vanishes for high parton momenta. At first glance, the fact that jet constituents for jets at  $p_{T,\text{parton}} \lesssim 30$  GeV are located closer to the jet axis when a medium is present compared to the case where jets fragment in vacuum contradicts this conclusion. However, one has to keep in mind that the angular distance to the jet axis a jet constituent can possess is limited by the cone radius used in the jet reconstruction. When the jet fragments get spread beyond the catchment area of the jet determined by the radius  $R$  used in the clustering algorithm, the fragments get distributed over multiple jets. These jets then contain less particles which have on average a smaller angular distance to the jet axis than a jet stemming from comparable vacuum-fragmentation. Comparable means that the original partons had the same transverse momentum. Further confirmation that the behavior of  $\langle \Delta\varphi_a \rangle$  at low parton  $p_T$  is an artifact of the cone radius and the reconstruction itself is given in Fig. 5.7. There, the procedure was repeated with a cone radius of  $R = 1.0$ . Since a single jet now covers a larger area and therefore can accumulate more particles, the distributions are shifted towards higher values of  $\langle \Delta\varphi_a \rangle$  in general. Furthermore it can be observed that the  $p_{T,\text{parton}}$  at which  $\langle \Delta\varphi_q \rangle$  for jets in the medium case lies below the  $\langle \Delta\varphi_q \rangle$  for jets in the vacuum case is shifted down to  $p_{T,\text{parton}} \approx 10$  GeV. Although a cone radius of  $R = 1.0$  seems to better capture the fragmentation of the jets, this value was not used in the analysis to maintain the comparability to results obtained with real data as much as possible.

### 5.2.3 Average transverse momentum and number of jet constituents

The concluding characteristics to describe jets on a general basis are the number of constituents in a jet coming from a parton with a certain momentum and the average

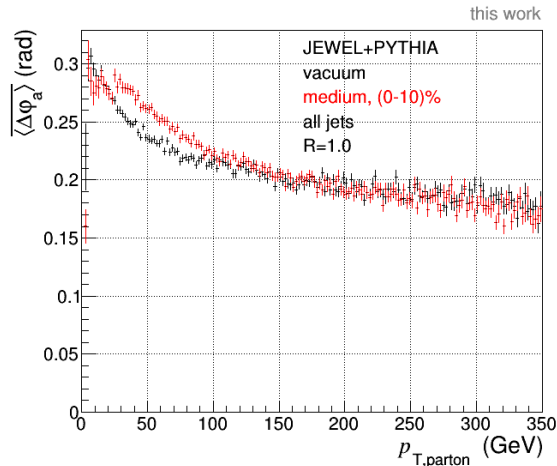


Figure 5.7: Mean average angular distance of the constituents of a jet, for all reconstructed jets in the hemisphere around a parton with  $p_{T,\text{parton}}$ . The distributions were obtained with a jet cone radius of  $R = 1.0$ .

transverse momentum each of the constituents carries. The 2-dimensional distributions of constituent number versus parton  $p_T$  is shown in Fig. 5.8. The top row again contains the distributions for all jets in a partons hemisphere. For both systems, a constant band across all parton transverse momenta is visible. When comparing the distributions to the ones in the bottom row, the distributions containing only the leading jets, it becomes clear that this band is caused by the subleading jets in the event. It is not present in the leading jet distributions. One can therefore conclude that the majority of the hadronized particles is contained within the leading jets, while the subleading jets contain at most 4-5 particles each. Investigation of the leading jet distributions lead to the observation that for  $p_{T,\text{parton}} \lesssim 50$  GeV in the vacuum case and  $p_{T,\text{parton}} \lesssim 30$  GeV in the medium case leading jets mostly have the same number of constituents. For higher parton  $p_T$ , the distributions broadens and the number of constituents contained in the leading jet varies. For a  $p_T = 300$  GeV vacuum fragmentation for example, there are equal amounts of leading jets containing 10 particles as there are leading jets containing 40 particles. For the fragmentations in events containing a medium, partons have to possess a higher transverse momentum than partons evolving in vacuum to reach on average the same number of constituents in the leading jet, since part of the momentum is transferred to the medium and therefore not available for further splittings.

The mean number of jet constituents is shown in Fig. 5.9. The profiles for all jets in a partons hemisphere are similar to the distributions for the leading jets, but scaled down. For  $p_{T,\text{parton}} \geq 50$  GeV in the vacuum case and  $p_{T,\text{parton}} \geq 100$  GeV in the medium case, where the width of the distributions in  $N_{\text{const.,lead. jet}}$  is constant for all  $p_{T,\text{parton}}$ , the profiles for all jets are scaled down by a constant factor of  $1.5 \pm 0.2$  compared to the profiles for the leading jet distributions (quantified by fitting the ratio with a linear function). On average, leading jets stemming from a vacuum fragmentation contain more particles than jets evolving in a medium for the chosen cone radius. A leading jet in vacuum for  $p_{T,\text{parton}} = 50$  GeV on average contains 16 particles. For a jet in medium to contain the same number of particles on average, the parton transverse momentum has

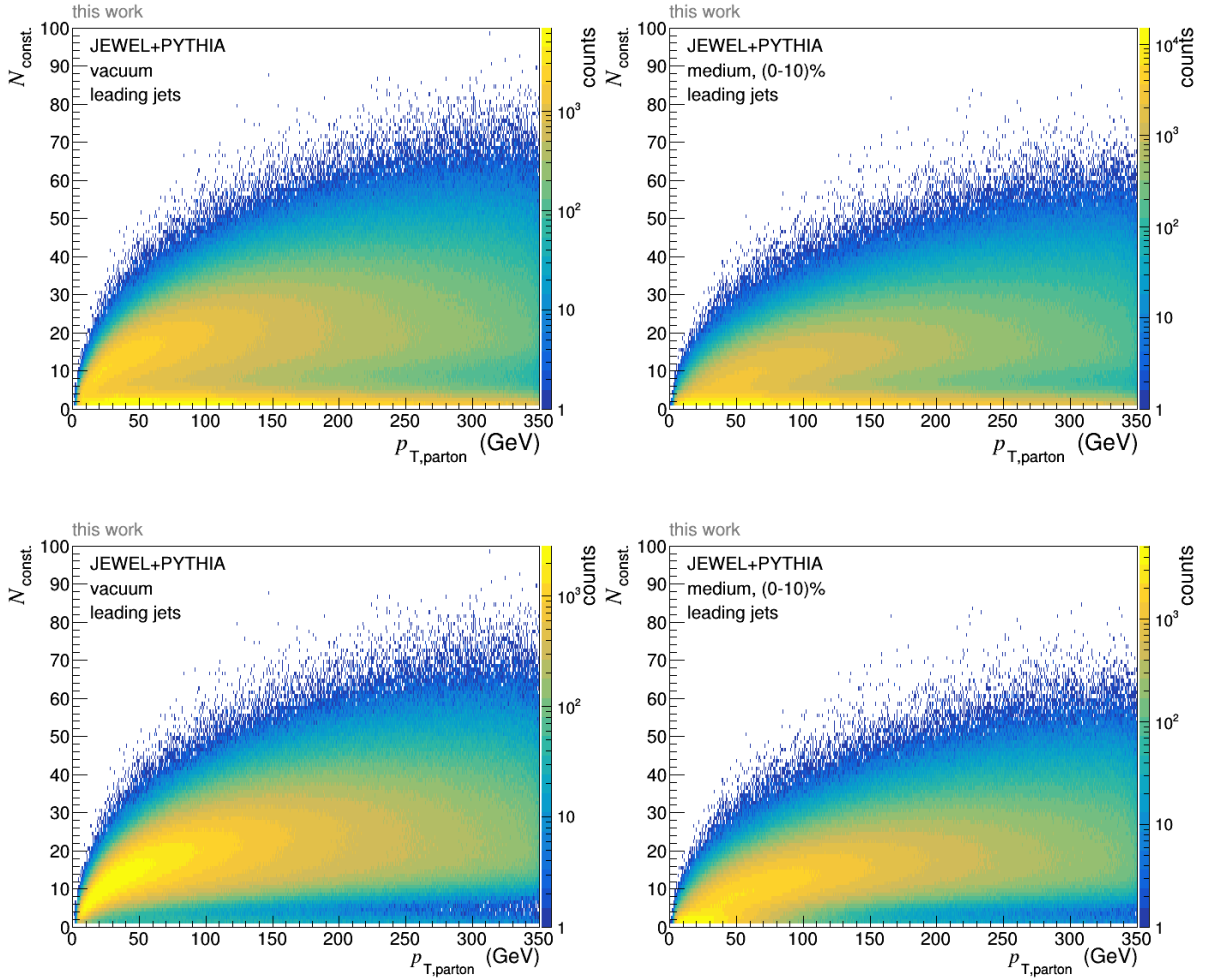


Figure 5.8: Number of constituents of all jets (top row) and the leading jets (bottom row) in the parton hemispheres for different parton  $p_T$ .

to be increased by 80 GeV.

To analyze the transverse momentum distribution among the constituents of the jets, Fig. 5.10 is included. The top row shows the distribution of average transverse momentum of the jet constituents of all jets in a partons hemisphere, the bottom row the distributions for the leading jets. Like in the top row of Fig. 5.8, a constant band with  $p_{T,\text{jet}} \leq 2 \text{ GeV}$  is observed across all  $p_{T,\text{parton}}$ . Since this band is not present in the leading jet distribution, it again corresponds to the sub-leading jets in each event. The sub-leading jets therefore contain only a few particles with on average low transverse momentum each, resulting in low transverse momenta of sub-leading jets, compared to the leading jets. This observation agrees with what was found for the distributions of transverse momentum above. In the distributions of  $\langle p_T \rangle_{\text{const.,lead jet}}$ , stripes are visible. These are an artifact of the division of the line at  $p_{T,\text{lead jet}} = p_{T,\text{parton}}$  in Fig. 5.2 by the integer number of constituents in the corresponding leading jet. Since the line is more distinct in the vacuum distribution than in the medium one, the stripes are more

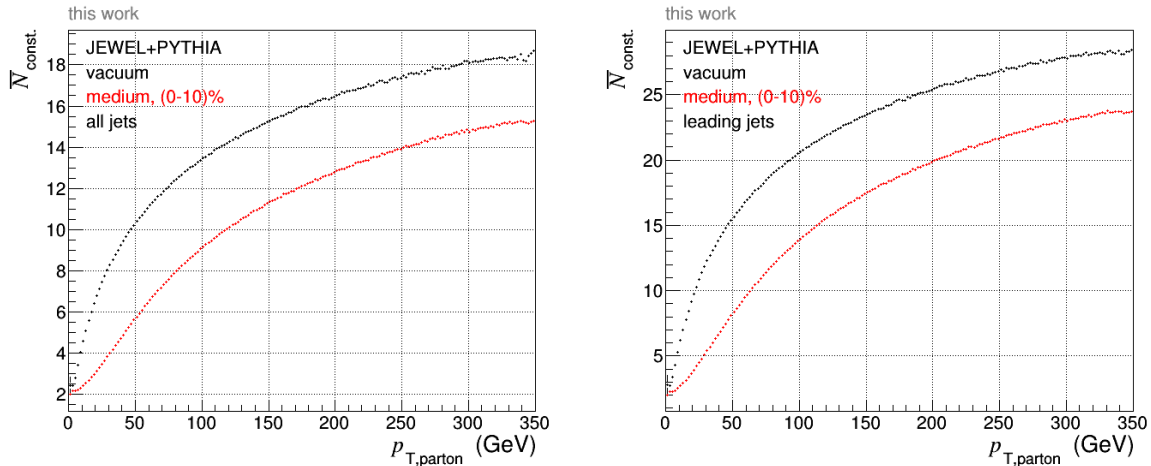


Figure 5.9: Mean number of constituents of all jets (left) and the leading jet (right) per parton  $p_T$ .

distinct in the vacuum distribution in the bottom row of Fig. 5.10.

The distribution of mean average transverse momentum per jet constituent and parton transverse momentum is depicted in Fig. 5.11. Like the mean number of constituents in all jets, see Fig. 5.9, the distribution of mean average transverse momentum of the constituents in a general jet is similar to the distributions for the leading jets. For  $p_{T,\text{parton}} > 50$  GeV,  $\langle \overline{p_T} \rangle_{\text{const.,lead. jet}}$  increases linearly with increasing parton momentum, where the rise is steeper for medium jets than for vacuum jets. For  $p_{T,\text{parton}} > 250$  GeV, the constituents of a leading jet fragmented in medium on average possess higher transverse momentum than the constituents of a jet fragmented in vacuum. Since the medium jets contain less particles than vacuum jets at comparable parton momentum, but a decrease of the quenching effect for high parton momenta was observed, this finding is consistent with the previous ones.

### Summary of the general characterization

In this section, jets and jet modification were characterized on a general level. It was found that the jet reconstruction with a cone radius of  $R = 0.6$  captures 80-90% of the partons transverse momentum in the leading jet. Jet modification by the medium in a (0-10)% collision results in a reduction of the leading jets transverse momentum by 20-60% for highest and lowest parton momenta, respectively. The medium modification further appears as a general reduction of number of particles a (leading) jet contains on average. At high parton momenta, the average transverse momentum carried by a single constituent of a jet in the medium case exceeds the transverse momentum carried by a constituent of a jet fragmented in vacuum. The quenching effect also appears as diffusion of the jet fragments, which reduces with increasing parton momentum.

With the description of jets via their transverse momentum and the fragmentation characterized by  $\langle \Delta\varphi_a \rangle$ ,  $N_{\text{const.}}$  and  $\langle p_T \rangle$ , the baseline for the following analysis is set. In the next section, the calculation of the path-length is described. When this second part of the analysis is defined, the previous findings will be compared to triggered distributions,

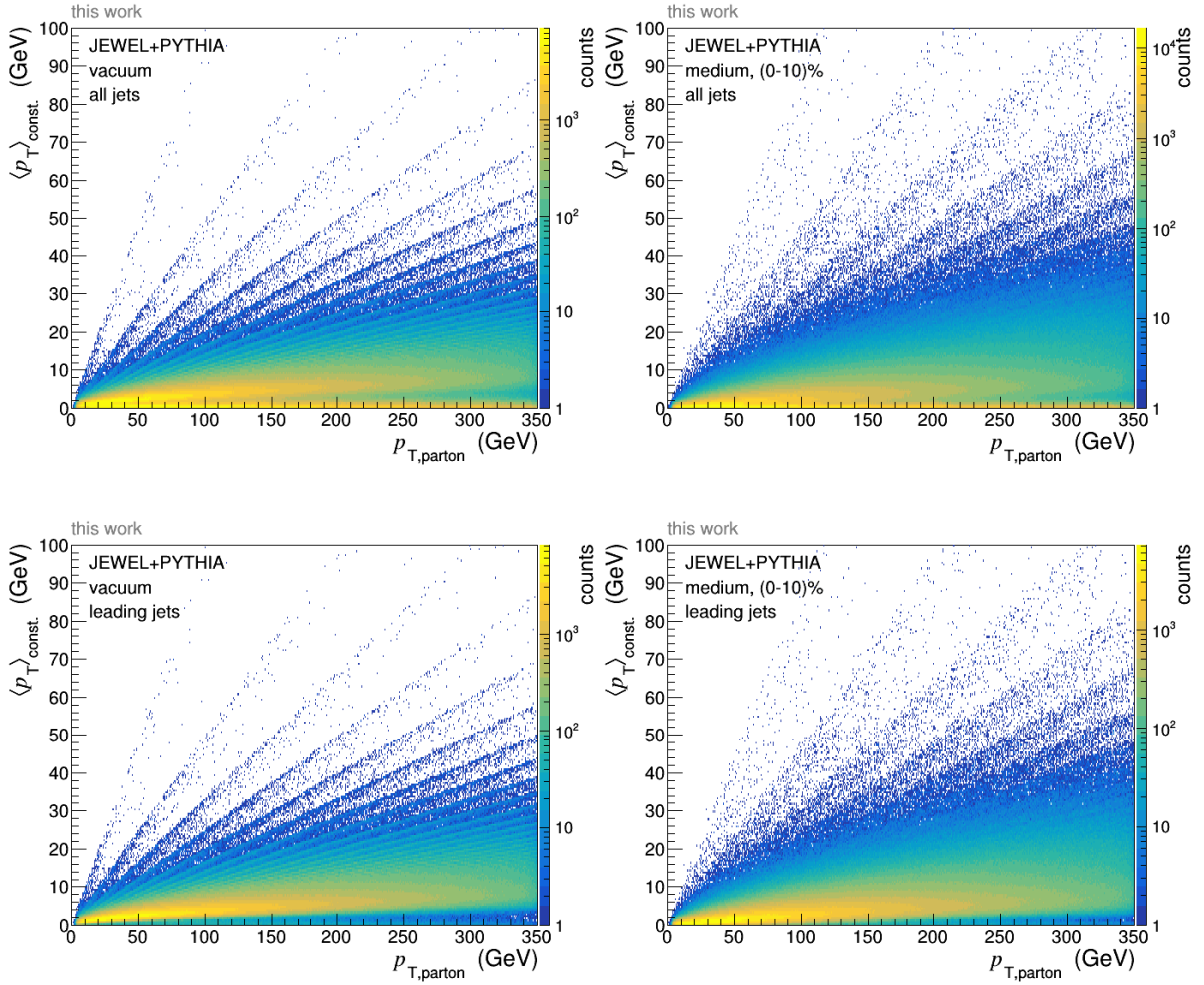


Figure 5.10: Top: Average  $p_T$  of all jets constituents versus the corresponding parton  $p_T$ . Bottom: Average  $p_T$  of the leading jets constituents versus the corresponding parton  $p_T$ .

where the effect of applying a trigger condition is studied. This will also set the basis for the evaluation of measuring the path-length of hard scattered partons with correlation functions.

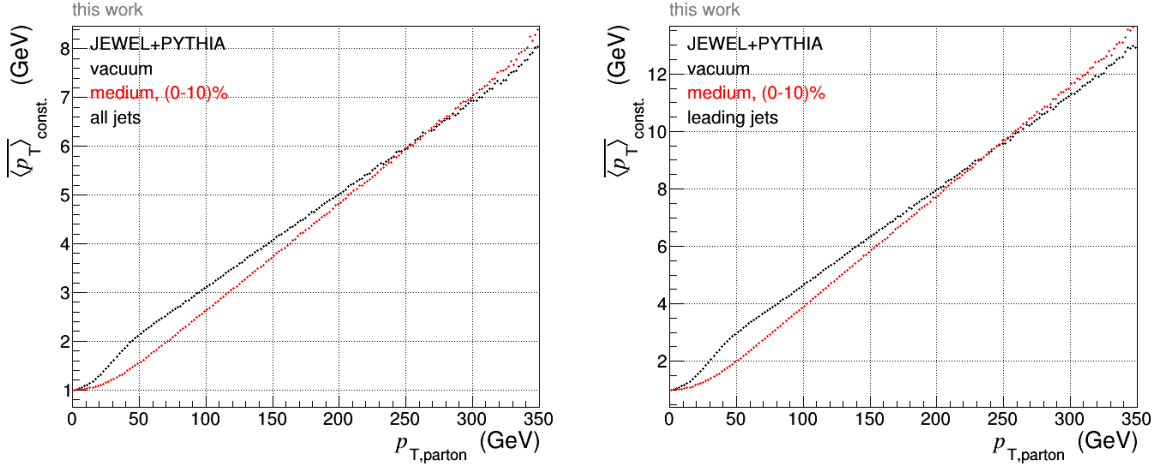


Figure 5.11: Mean average transverse momentum of the constituents of a general jet (left) and the leading jets (right) for the corresponding parton  $p_T$ .

## 5.3 Quantifying the path-length

With jets and jet modification being characterized on a general basis, the second quantity that has to be determined for this analysis is the path-length itself.

### 5.3.1 Geometrical and energy-density weighted path-length

The most precise way to calculate the path-length is a scattering-by-scattering analysis, evaluating the number of scatterings of the parton off the medium constituents while considering the time between scatterings and the scattering angle, then summing up all contributions. However, this approach was not chosen for this analysis for two main reasons. First of all, the computation time and effort exceed the additional benefits of this detailed method compared to the approach chosen for this thesis. Second, due to fragmentation and the quenching process itself, a jet definition is ambiguous even on a partonic level. This makes the choice of what parton to track through the medium an ill-defined quantity. Therefore, for this analysis two approximations for the parton path were made.

#### Geometrical path-length

Under the assumption that the partons move on a straight line through the medium, the path-length was defined as the geometrical distance between the vertex of the initial hard scattering and the edge of the overlap region. A schematic depiction of the calculation is shown in Fig. 5.12. The overlap region is defined as the intersection area of two circles (the "colliding" nuclei) with radius  $R_{\text{AU}} = 10$  fm. This value is the parameter implemented in the JEWEL source code. The impact parameter  $b$  quantifies the overlap. Starting from the vertex of the hard scattering,  $\mathbf{v} = (x_v, y_v)$ , the intersection of the partons line

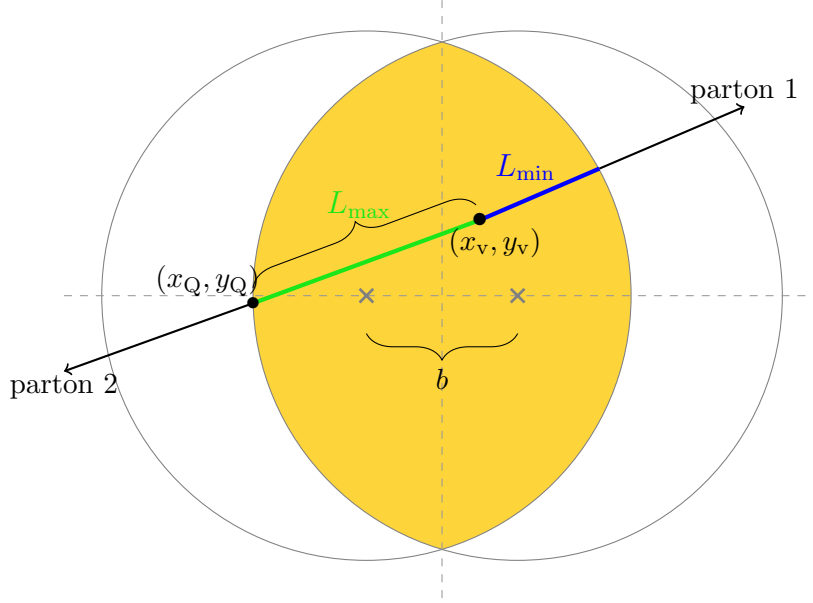


Figure 5.12: Schematic depiction of the geometrical pathlength calculation. The shaded area represents the overlap region of the "colliding" nuclei in the transverse plane, where  $b$  is the impact parameter.  $(x_v, y_v)$  is the vertex position of the initial hard scattering,  $(x_Q, y_Q)$  the intersection point of the parton line with the edge of the overlap region.  $L_{\max}$  and  $L_{\min}$  are the path-lengths of both partons, labeled according to their relative magnitude.

$$\mathbf{x}_p = \mathbf{v} + \lambda \mathbf{d} = \begin{pmatrix} x_v \\ y_v \end{pmatrix} + \lambda \begin{pmatrix} \cos \varphi \\ \sin \varphi \end{pmatrix} \quad (5.3)$$

with the two circles located at

$$K_{1/2} : \quad (\mathbf{x} - \mathbf{c})^2 = R_{\text{AU}}^2 \quad (5.4)$$

$$\left[ \begin{pmatrix} x \\ y \end{pmatrix} - \begin{pmatrix} \mp b/2 \\ 0 \end{pmatrix} \right]^2 = R_{\text{AU}}^2 \quad (5.5)$$

was calculated. Depending on the partons direction, quantified by its azimuthal angle  $\varphi$ , the intersection point  $\mathbf{Q} = (x_Q, y_Q)$  is either on the left circle ( $K_1$ ) or the right one ( $K_2$ ). The geometrical path-length  $L$  is then calculated as distance between  $\mathbf{v}$  and  $\mathbf{Q}$ :

$$L = \sqrt{(x_Q - x_v)^2 + (y_Q - y_v)^2}. \quad (5.6)$$

This procedure is done for each parton in each event. The longer one of the path-lengths is labeled as  $L_{\max}$ , the other one  $L_{\min}$ .

Fig. 5.13 shows the distribution of geometrical path-lengths in events with (0 – 10) % centrality. In JEWEL the interaction vertex is chosen based on the interaction density of nucleons Fig. 5.15. This is highest at the center of the overlap region and drops

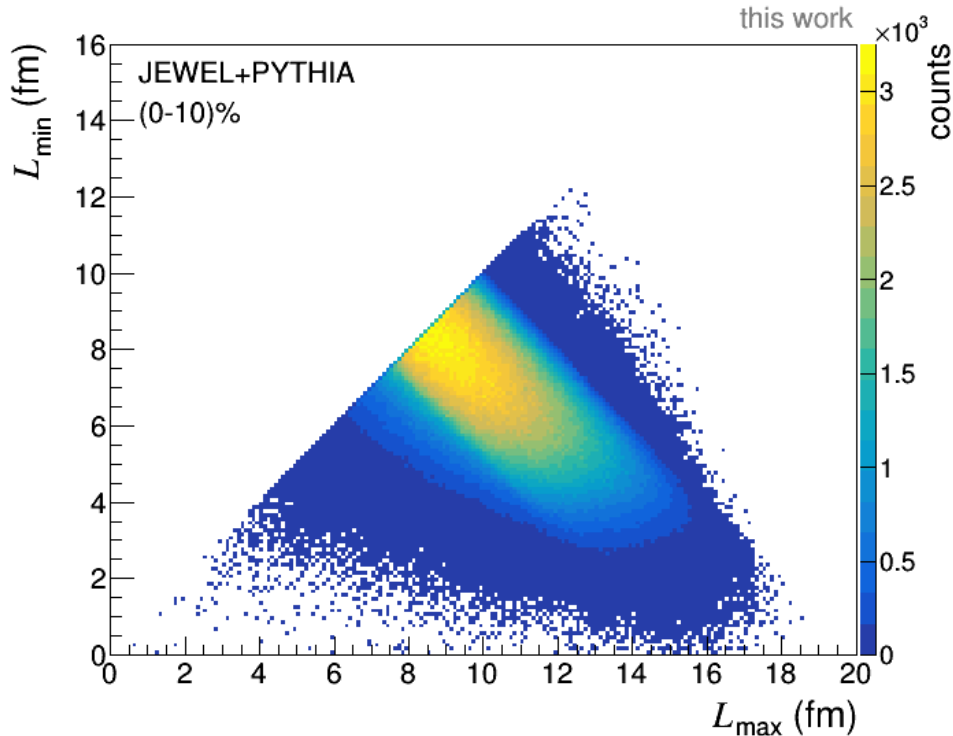


Figure 5.13: Distribution of the geometrical path-length, minimum value vs. maximum value.

rapidly when approaching the edges. Therefore, parton pairs are only rarely produced near the edge of the overlap region, explaining the lack of path-lengths  $L \lesssim 3$  fm. The partons are emitted back-to-back in azimuth and are generated uniformly in  $\varphi$ . Thus, the distribution of path-lengths reproduces the shape of the overlap region.

### Energy-density weighted path-length

The number of interactions and the scale of the interaction processes depend on the spatial- and energy-distribution of the mediums constituents. It is therefore important to not only consider the simple geometrical path-length when interpreting path-length shifts in triggered distributions, but also the energy-density distribution has to be taken into account. For this reason, an energy-density weighted path-length was introduced. The schematic depiction of this process is shown in Fig. 5.14. For the energy-density weighted path-length  $L\varepsilon$ , the energy-density distribution was integrated over the partons path, including the vertex of the hard scattering.

The formulas used in this part were already discussed in Sections 2.2 and 4.1. The transverse energy-density distribution at the beginning of the evolution is calculated on the basis of a Glauber model,

$$\varepsilon(x, y, b, \tau_0) = \varepsilon_0 n_{\text{part}}(x, y, b) \frac{\pi R_{\text{AU}}^2}{2A}, \quad (5.7)$$

where  $A = 208$  like in the initialization of JEWEL is chosen. The energy-density at the center,  $\varepsilon_0$ , is calculated according to Eq. (4.9) with the initial temperature  $T_i = 360$  MeV.

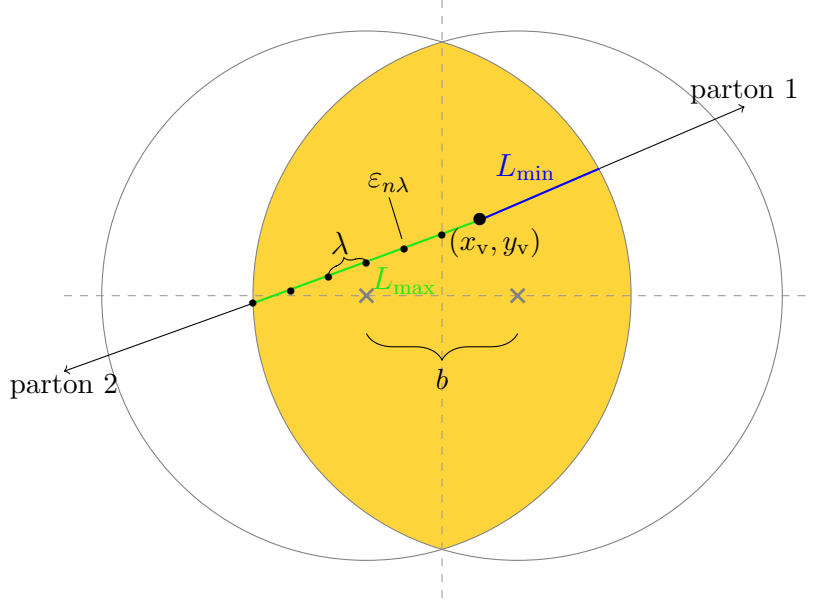


Figure 5.14: Schematic depiction of the energy-density weighted path-length calculation. The energy-density is integrated over the parton's path, including the vertex of the hard scattering. In the end it is normalized by the number of steps.

The resulting energy-density distribution is depicted in Fig. 5.15. It is largest in the center of the overlap region and decreases radially. Due to the longitudinal expansion in the Bjorken model, the temperature of the medium decreases – as described in Eq. (4.14) – and the energy density decreases accordingly over time. However, as simplification it was assumed in this analysis that the partons traverse the medium before the energy density drops significantly and only the initial value was considered.

For the integration of the energy-density distribution in direction of the parton path, the path was subdivided into single parts:

$$x_{n+1} = x_n + \xi \cos \varphi \quad (5.8)$$

$$y_{n+1} = y_n + \xi \sin \varphi. \quad (5.9)$$

$\xi = 0.1$  fm was chosen as stepsize. The number of participants at this transverse position is then calculated according to Eq. (4.12). The calculation starts with  $(x_0, y_0) = (x_v, y_v)$ . In each step, the local energy-density is added to the sum. In the end, the total integrated energy-density is normalized by the number of steps:

$$\langle \varepsilon_{\text{tot}} \rangle = \frac{1}{N} \sum_{n=0}^N \varepsilon_{n\xi}, \quad N = \frac{L}{\xi} + 1. \quad (5.10)$$

The energy-density weighted path-length is then calculated as product of the integrated energy density and geometrical path-length:

$$L_{\text{weighted}} = L \cdot \langle \varepsilon_{\text{tot}} \rangle. \quad (5.11)$$

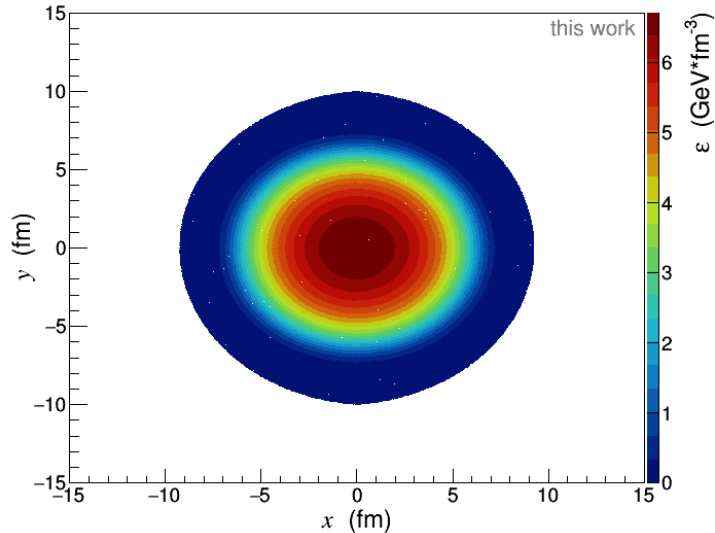


Figure 5.15: Energy-density distribution according to the Glauber model in the transverse overlap region of two "nuclei" with  $r = R_{\text{AU}} = 10$  fm and impact parameter  $b = 1.5$  fm for an initial temperature  $T_i = 360$  Mev.

The distribution of weighted path-lengths can be seen in Fig. 5.16. The shape obtained with the simple geometrical path-length is still visible. However, depending on the starting point and direction of each parton, the paths can receive very different weightings. This results both in a smearing of the overlap shape as well as an extension of path-lengths down to minimal values. When a parton is produced towards the surface of the overlap and directly flies out of the medium, without traversing the regions of highest energy density, it receives a low weighting, in some cases  $< 1 \text{ GeV}/\text{fm}^2$ . This results in the spread even down to  $L\varepsilon \approx 0$ , despite the lack of very low path-lengths in the geometrical case.

### 5.3.2 Path-length and jet modification

In Section 5.2, jets and jet modification were characterized amongst other things with the jet  $p_T$  spectra for different ranges in parton  $p_T$ . To add the path-length of the partons to this picture, a further selection criterion can be applied for these distributions: the requirement to lie in a certain range of (energy-density weighted) path-length. The resulting distributions for different ranges in  $p_{T,\text{parton}}$  and  $L/L\varepsilon$  are shown in Fig. 5.17 and Fig. 5.18 for all jets and the leading jets of the parton hemispheres, respectively. As was the case for the distributions without selection on the weighted path-length, the spectra are very similar for all jets and the leading jet only. Especially at low parton transverse momentum ( $p_T = 10 - 15 \text{ GeV}$  and  $p_T = 20 - 25 \text{ GeV}$ ), the bump observed for leading jets in vacuum is quenched away almost completely in the medium.

As can be seen in these distributions, there is a clear connection visible in JEWEL between parton energy loss and the path-length this parton had in the medium. The abundancies of jets with comparable transverse momentum decrease distinguishable when

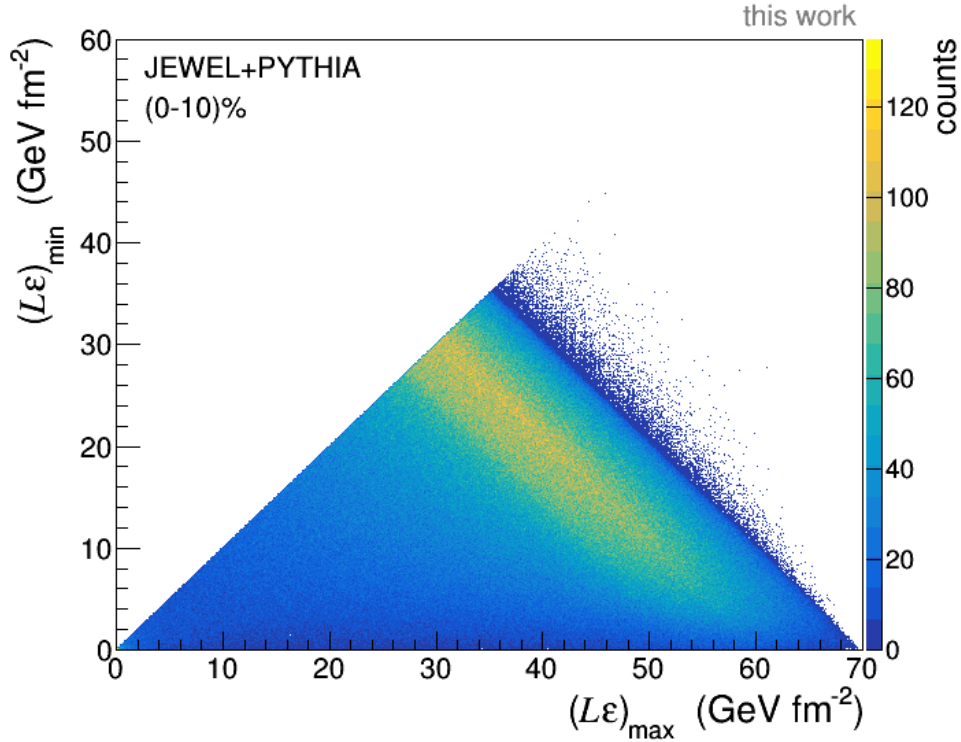


Figure 5.16: Distribution of the energy-density weighted pathlength. The smearing of the shape observed for the simple geometrical path-length as well as the extension down to  $L\varepsilon \approx 0$  is due to different weights on the path. The weights are dependent on production point and the direction of the respective parton.

going from intervals with low (weighted) path-length to intervals with high (weighted) path-length. It is remarkable that shape and evolution of distributions with interval selections in energy-density weighted path-length resemble closely those with selections in simple geometrical path-length. When the observation of path-length could be done independently for the un-weighted and weighted cases, one would expect different shapes and/or distributions. Thus, these plots indicate that the observation of path-length dependent energy loss is mixed with observations of the energy-density distribution.

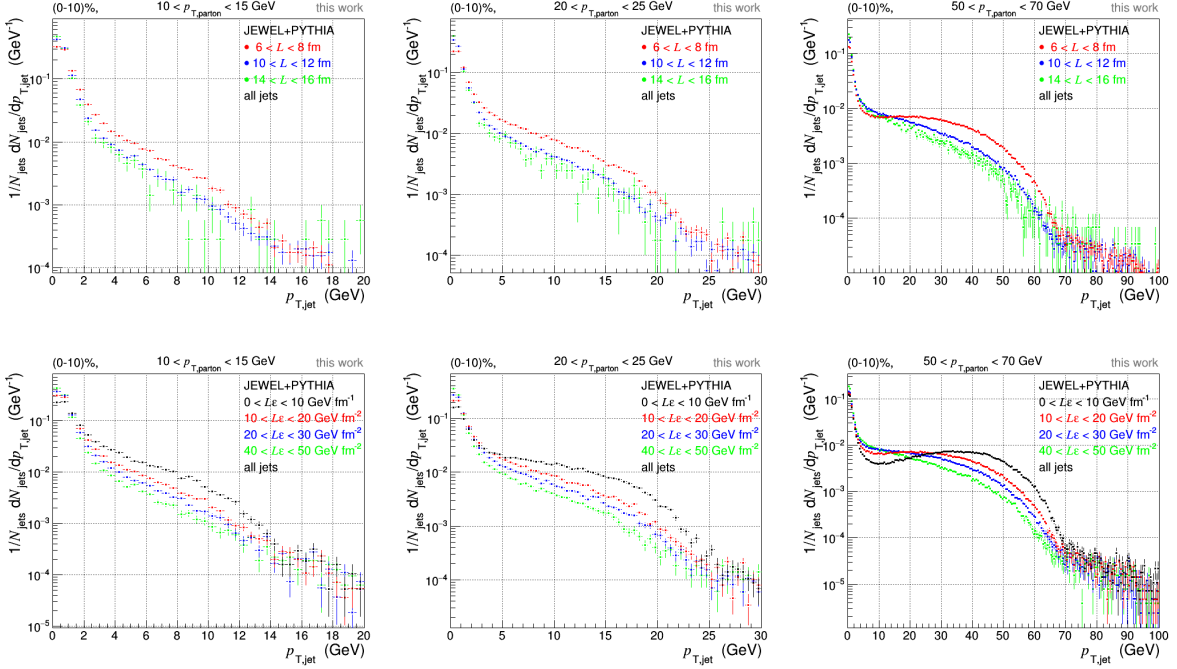


Figure 5.17: Jet  $p_T$  spectra of all jets for different ranges in parton  $p_T$  and (weighted) path-length. The top row shows distributions for the simple geometrical path-lengths, the bottom row for weighted path-lengths.

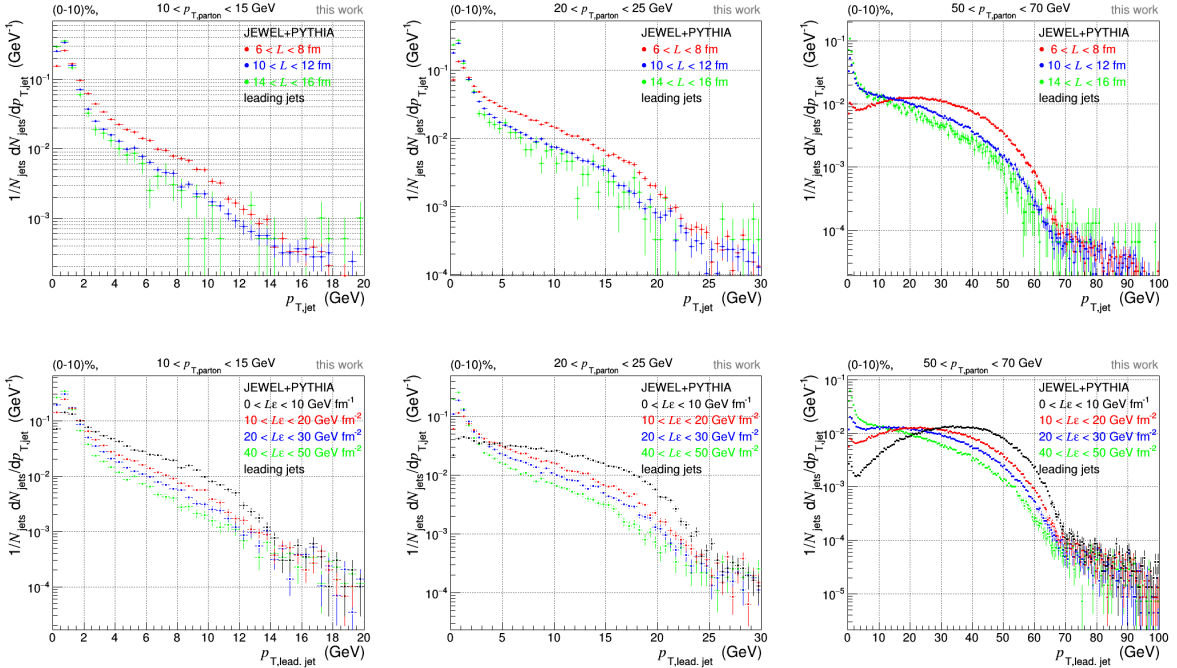


Figure 5.18: Jet  $p_T$  spectra of the leading jets for different ranges in parton  $p_T$  and (weighted) path-length. The top row shows distributions for the simple geometrical path-lengths, the bottom row for weighted path-lengths.

## 5.4 Triggered distributions

In the previous two sections jets and jet modification were characterized on a general basis. The geometrical and energy-density weighted path-length were quantified as well. The aim of this analysis is to test if the path-length, a hard scattered parton had in the QGP, can be probed with correlation functions. In order to do this, one has to understand how a trigger condition changes the selection of parton momentum, fragmentation and path-length. In the following, the effect of the application of a trigger condition on the general distributions described in Section 5.2 is discussed. This is done by looking first at the most basic trigger condition, the selection of a single hadron in a certain  $p_T$  interval. Once it is understood how a single trigger selects jet and parton  $p_T$ , fragmentation and path-length, the study is expanded to back-to-back dihadron trigger conditions.

### 5.4.1 Single hadron trigger

To study the influence of a hadron trigger on the distributions discussed in Section 5.2, the same characteristics as in these distributions were studied for jets that comply with specific trigger conditions. The trigger condition that selects the jet is the leading track, a single hadron, in the jet. If the leading hadron of the jet lies in the chosen  $p_T$  interval, the jet and its properties like the  $p_T$ , average angular distance of the jets constituents to the jet axis and so on, get filled into their corresponding histograms. The chosen bins for the trigger hadron in  $p_T$  have a width of 2 GeV. In total, nine bins were tested as trigger condition, covering the  $p_T$  range 2-20 GeV. The lower limit of each bin is inclusive, the upper limit is exclusive. The inferred parton properties ( $p_T$  and path-length; the determination of the latter is described in the previous section) are again taken from the parton that lies in the same hemisphere as the triggered jet ( $\varphi_{\text{triggered jet}} = \varphi_{\text{parton}} \pm \frac{\pi}{2}$ ). For the sake of presentability, in the following discussion of the triggered distributions and the comparison to the general ones, only three trigger conditions are actually displayed in the figures.

#### Jet transverse momentum

The distributions for the triggered jet transverse momentum versus the corresponding partons transverse momentum are shown in the top and middle row of Fig. 5.19. In the columns, the plots are ordered by increasing trigger- $p_T$ . On the left, the lowest bin is shown, where the leading hadron is required to have a transverse momentum in the interval  $2 \leq p_T^{\text{trig}} < 4$  GeV. The middle and right column correspond to  $6 \leq p_T^{\text{trig}} < 8$  GeV and  $12 \leq p_T^{\text{trig}} < 14$  GeV respectively. The top row shows the plots for the vacuum case, the middle row shows the plots for the medium case. The distributions show that, generally speaking, applying a trigger condition selects a (relatively broad) range both in parton  $p_T$  and jet  $p_T$ . Looking first at the 2 – 4 GeV triggered distribution, the majority of the simulated data points is observed both for the vacuum case and for the medium case at parton  $p_T \lesssim 50$  GeV. In the medium case, the peak has a long tail, extending to  $p_{T,\text{parton}} \approx 100$  GeV. Therefore, with such a low trigger momentum, predominantly scatterings in this range are selected. Although the majority of the triggered jets is found at  $p_{T,\text{parton}} \lesssim 50$  GeV, the distribution also extends to the highest parton trans-

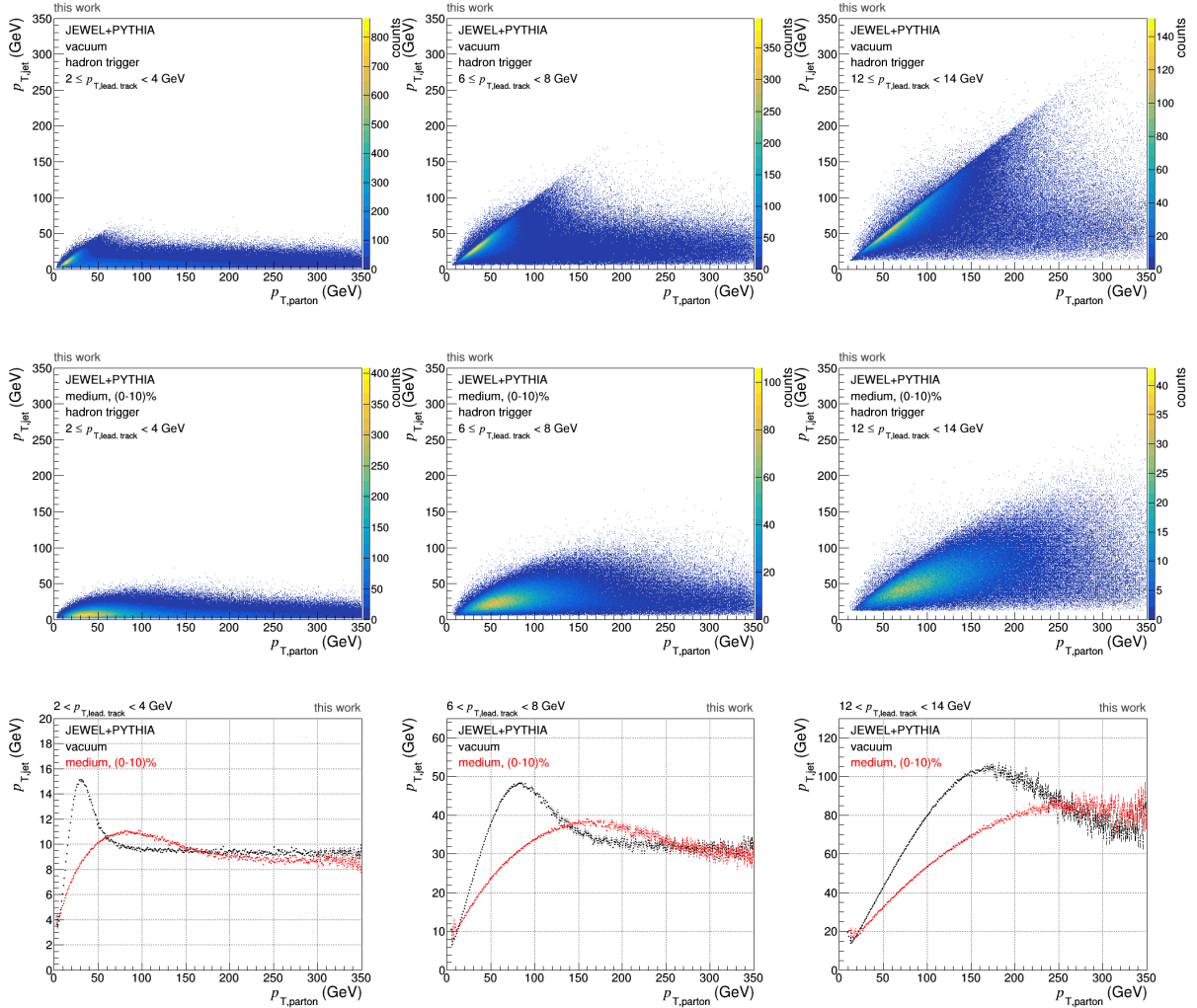


Figure 5.19: Top and middle: 2D distributions of the reconstructed triggered jet  $p_T$  vs. parton  $p_T$  in medium and in vacuum for three different trigger conditions. Bottom: Mean triggered jet  $p_T$  vs. parton  $p_T$  for three different trigger conditions.

verse momenta included in JEWEL,  $p_{T,\text{parton}} = 350 \text{ GeV}$ . At  $p_{T,\text{parton}} \lesssim 50 \text{ GeV}$ , the distribution of jet  $p_T$  vs. parton  $p_T$  resembles the distribution for the leading jets in Fig. 5.2, especially in the vacuum case. At higher parton  $p_T$ , the distribution is closer to the general distribution. Therefore, when the triggered jet in the vacuum case originates from a parton with  $p_T < 50 \text{ GeV}$ , in general a leading jet is selected with the trigger particle. For higher parton  $p_T$  in general a sub-leading jet is selected. Since the distribution for the leading jets in the medium case is very broad, the discrimination between leading and sub-leading jets is difficult, even at low parton  $p_T$ . It should however be noted that the parton  $p_T$  itself is not measurable in real experiments, unlike in the evaluation of simulated data. In combination with the corresponding jet momentum one can make a statement about the parton  $p_T$  range which was most probably selected, but even this evaluation can be quite ambiguous for low jet  $p_T$ . For example, a triggered jet with  $p_T = 10 \text{ GeV}$  originates most probably from a parton in the momentum range  $10 < p_T < 15 \text{ GeV}$  and is, in this range, the leading jet. However, when the trigger condition selects a sub-leading jet, it could originate from a parton with arbitrary transverse momentum. Due to quenching, the range in parton  $p_T$  for which a  $10 \text{ GeV}$  triggered jet in the medium case acts as leading jet is already broader than in the vacuum case. Additionally, the separation between leading and sub-leading jets is less distinct. This makes it even more difficult in the medium case to distinguish between different parton momenta and fragmentations. This complication underlines the need for an observable which can be used to measure the in-medium path-length of partons as independent of the parton  $p_T$  and fragmentation as possible.

The profiles, i.e. the mean triggered jet transverse momentum as a function of parton  $p_T$ , for the three different trigger conditions are shown in the bottom row of Fig. 5.19. The profile for the  $2 - 4 \text{ GeV}$  trigger condition is again placed in the left column. In the medium case, jets on average have a lower transverse momentum than jets in the vacuum case for  $p_{T,\text{parton}} < 60 \text{ GeV}$ . Due to the broad distribution of leading jets, the average momentum of triggered jets in the range  $60 < p_{T,\text{parton}} < 150 \text{ GeV}$  is higher in the medium case than in the vacuum case. The peak in the vacuum case between  $30$  and  $60 \text{ GeV}$  corresponds to the selected leading jets. On average, their momentum is  $\sim 5 \text{ GeV}$  higher than the momentum of the sub-leading jets. In the medium case, the less distinct difference between leading and sub-leading jets in transverse momentum becomes more apparent. The highest jet  $p_T$  on average, which is reached at  $\sim 80 \text{ GeV}$ , is only  $\sim 2 \text{ GeV}$  higher than the average momentum of sub-leading jets at high parton  $p_T$ .

When going from this lowest trigger condition to higher trigger  $p_T$  (see the other plots in Fig. 5.19), the predominantly selected range in parton  $p_T$  broadens and on average, higher jet  $p_T$  are reached. Comparing the 2-dimensional distributions to the general ones in Fig. 5.2, they increasingly resemble the leading jet distributions with increasing trigger  $p_T$ . Since the distribution of leading jet  $p_T$  is very broad in the medium, even with higher trigger  $p_T$ , it is not certain whether a leading or a sub-leading jet was selected. Likewise in the vacuum case, for  $p_{T,\text{jet}} \lesssim 150 \text{ GeV}$  in some cases sub-leading jets are selected even for high parton  $p_T$ . However, upon comparison of general and triggered distributions, trigger with increasing hardness select leading jets with increasing probability.

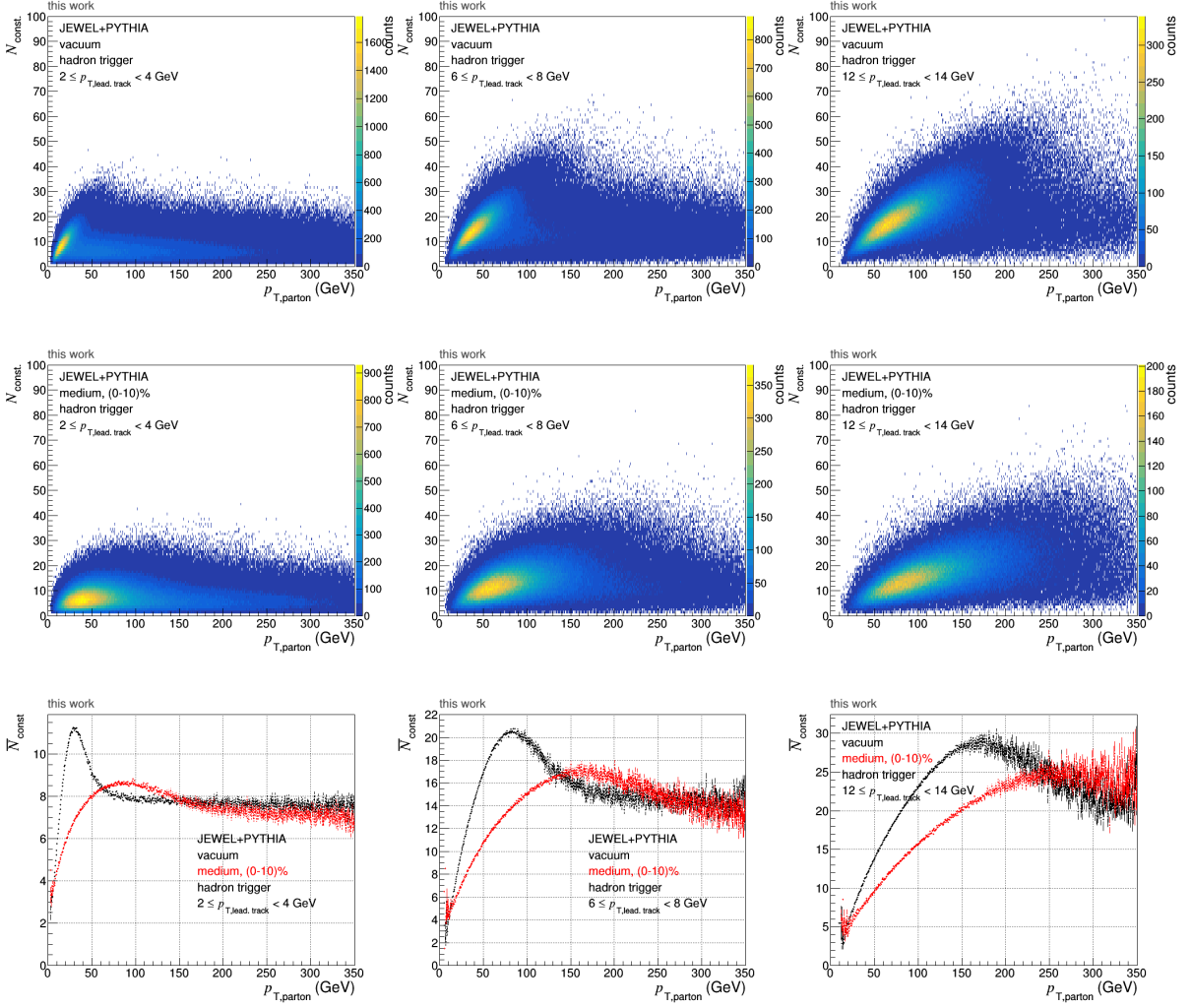


Figure 5.20: Top and middle: 2D distributions of number of constituents in the triggered jet vs. parton  $p_T$  for vacuum and medium for three different trigger conditions. Bottom: Mean number of constituents for different trigger conditions.

### Number of constituents

To make a coherent argument for the influence of triggering on the jet fragmentation, the discussion in this part starts with the examination of the number of constituents in the triggered jets.

The 2D distributions of number of constituents in the triggered jet for different parton  $p_T$  are shown in the top and middle row of Fig. 5.20. In their behaviour for increasing trigger  $p_T$  and in the different ranges of parton  $p_T$ , the 2-dimensional distributions resemble closely the distributions of triggered jet momentum. In the lowest bin in trigger condition, mostly jets with less than 10 constituents in the medium case and less than 15 constituents in the vacuum case are selected. With increasing hardness, the triggered jets have increasingly higher numbers of constituents. The profiles of the 2-dimensional distributions, bottom row of Fig. 5.20, are in shape very close to the distributions in Fig. 5.19. For parton  $p_T < 60$  GeV, jets in medium have on average less constituents

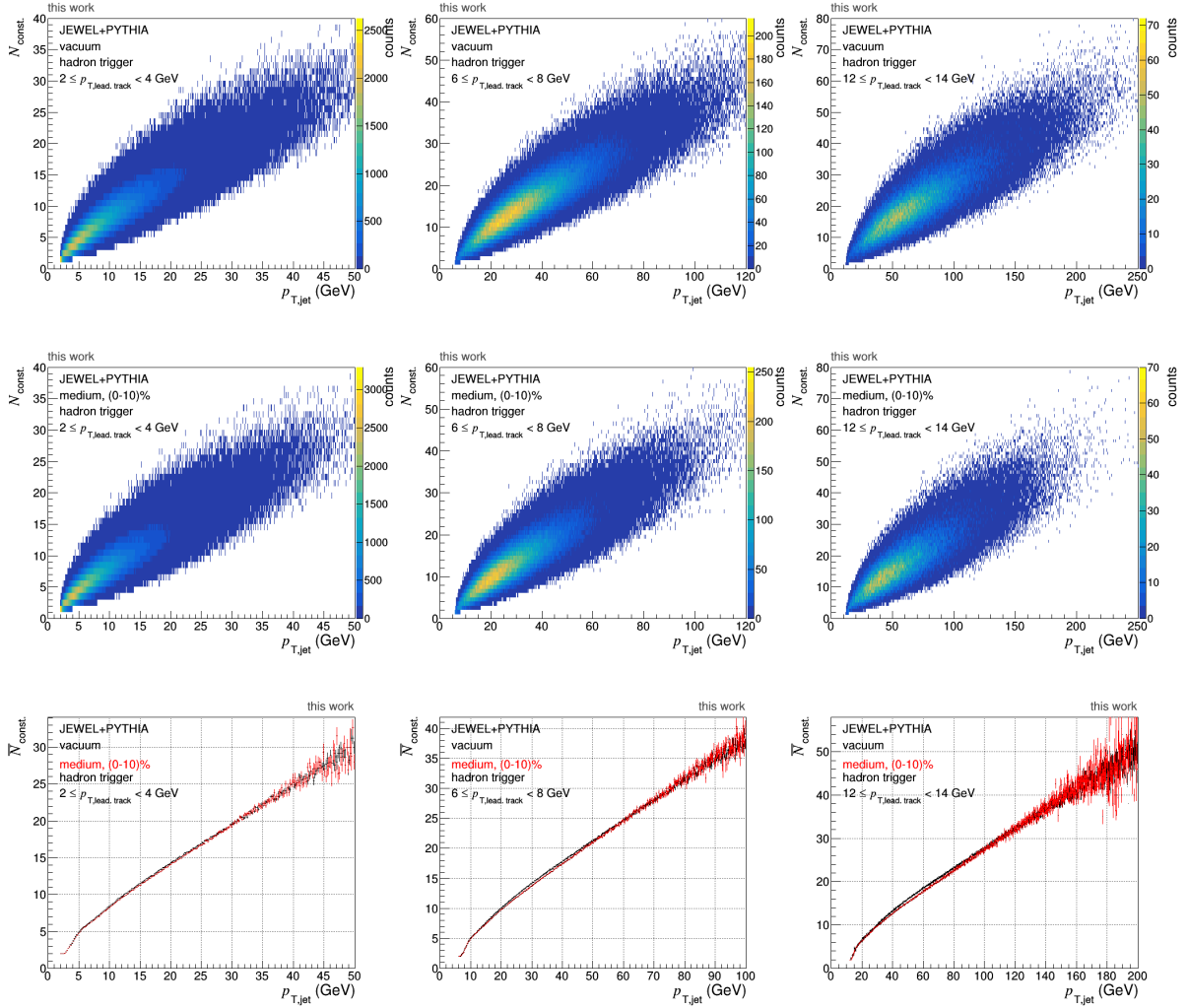


Figure 5.21: Top and middle: Number of constituents of the triggered jet vs. the jets  $p_T$ , in vacuum and medium for different trigger conditions. Bottom. Mean number of constituents vs. the triggered jet  $p_T$  for the different trigger conditions.

than jets in the vacuum case. In the parton  $p_T$  range, where  $p_{T,\text{jet}}$  is on average higher in the medium case, the jets on average also contain more particles than in the vacuum case. The profiles for the other trigger conditions are as well in direct correspondence to the associated profiles of the jet transverse momentum.

This behavior can be explained when looking at the number of constituents for different jet momenta, top and middle row of Fig. 5.21. The distributions are very similar in the vacuum case and in the medium case. A direct correlation of jet  $p_T$  and constituent number is observed. With increasing jet  $p_T$ , the number of particles this jet contains increases. With the lowest trigger condition,  $2 \leq p_T^{\text{trig}} < 4$  GeV, mostly jets with low momentum and therefore low number of particles get selected both in the vacuum case and in the medium case. With increasing trigger  $p_T$ , also higher jet  $p_T$  (and higher numbers of constituents) get selected more frequently. Due to this correlation, the shape of the distributions and profiles of (mean) number of constituents per parton  $p_T$  correspond

closely to the distribution of (mean) jet  $p_T$  per parton  $p_T$ . For low parton  $p_T < 60$  GeV the jet  $p_T$  is, on average, smaller in the medium case compared to the vacuum case. Therefore, also the number of constituents is smaller in this range. The same logic applies to other parton  $p_T$  ranges.

The mean number of constituents per jet  $p_T$  is shown in the bottom row of Fig. 5.21. For the same jet  $p_T$  and a cone radius of  $R = 0.6$ , the mean number of constituents is almost the same in the medium and the vacuum case, across all trigger conditions. However, on average the mean number of constituents in the medium case lies slightly below the mean number in the vacuum case for jet  $p_T$  below 30 GeV, 60 GeV and 100 GeV for the first, second and third trigger condition displayed, respectively.

### Average transverse momentum

The average transverse momentum that a constituent of the triggered jet carries is shown in Fig. 5.22. The top and middle row show the 2D distributions in vacuum and in medium, the bottom row displays the profiles of these distributions. In the 2D distribution a stripe pattern is visible. This corresponds to the momentum of the jet being divided by an integer number of constituents. The uppermost stripe corresponds to a single particle jet (i.e. the jet contains only the trigger particle), the stripe below that corresponds to a two-particle jet, and so on. For a given jet momentum and number of particles in the jet, the average momentum carried by a single jet constituent lies, in the 2-dimensional distributions, below the  $p_T$  of the trigger particle. The higher the trigger  $p_T$  is, the larger the difference between the trigger and the average of all particles. For example, in the 2D vacuum distribution for  $6 \leq p_T < 8$  GeV, the predominantly triggered jet  $p_T$  lies in the range 15-40 GeV. The average momentum per jet constituent for this jet momentum range is 2-3 GeV. This means that in JEWEL the main fraction of the triggered jet momentum is carried by the trigger particle. When looking at the mean average transverse momentum per jet constituent, it is slightly higher in the medium case for the same ranges in jet  $p_T$  where the number of constituents was lower in the medium case than in the vacuum case.

The 2D distribution of average transverse momentum carried by a constituent for different parton  $p_T$  is shown in the top and middle row of Fig. 5.23. The profiles are shown in the bottom row. It was found that at low parton  $p_T$ , in the medium case predominantly jets with lower  $p_T$  than jets in the vacuum case are selected. Therefore, the average transverse momentum per jet constituent is in this parton  $p_T$  range higher in the medium case than in the vacuum case. However, since the same jet  $p_T$  can be selected for different parton  $p_T$ , the mean average transverse momentum fraction is mostly constant across all parton  $p_T$ .  $\langle \Delta p_T \rangle_{\text{const.}}$  increases for all parton  $p_T$  with increasing trigger  $p_T$ , which is consistent with the previous findings.

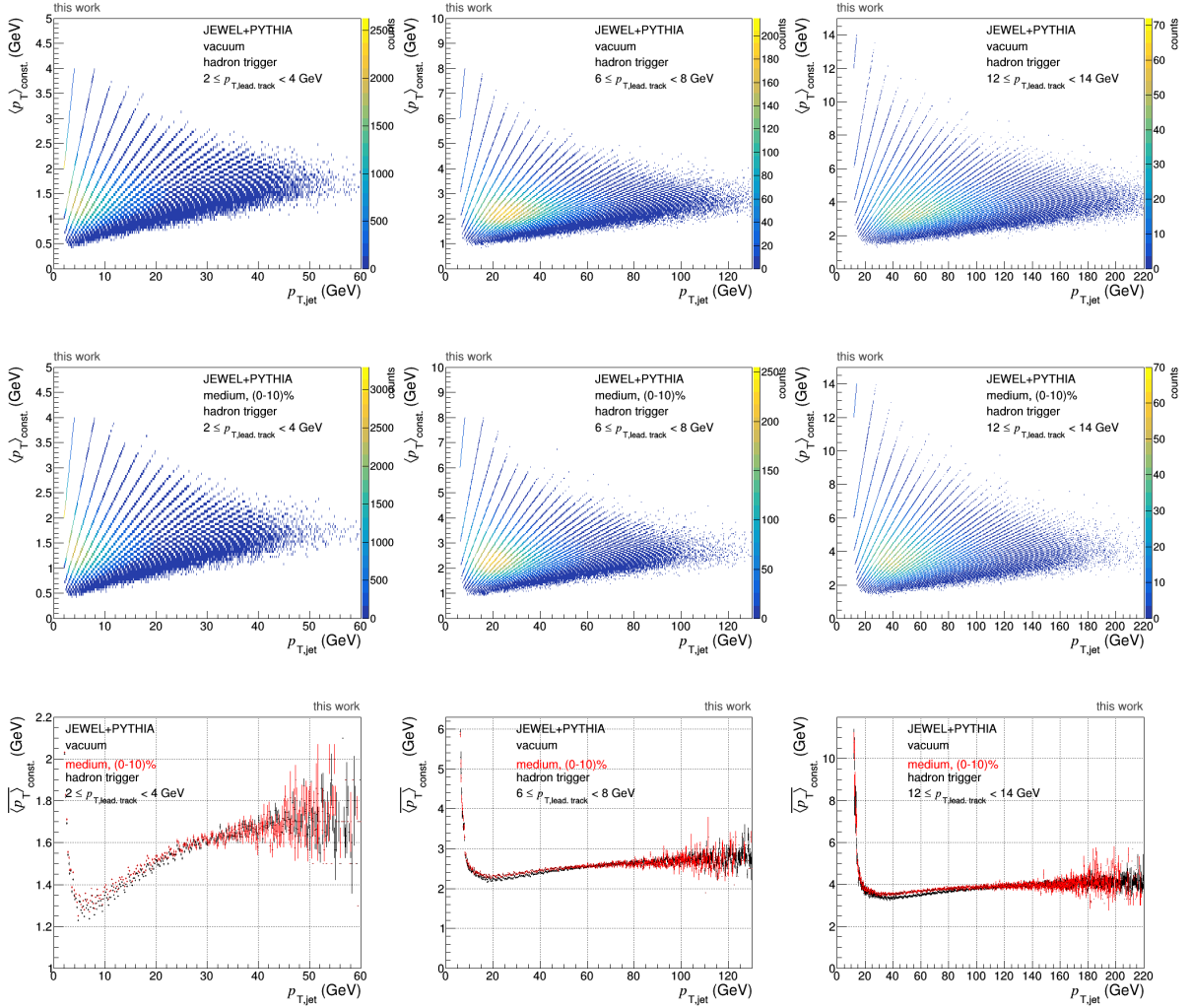


Figure 5.22: Top and middle: Average transverse momentum per jet constituent vs. the  $p_T$  of the triggered jet, in vacuum and medium. Bottom: Mean average transverse momentum of the triggered jets constituents vs. the triggered jet  $p_T$ .

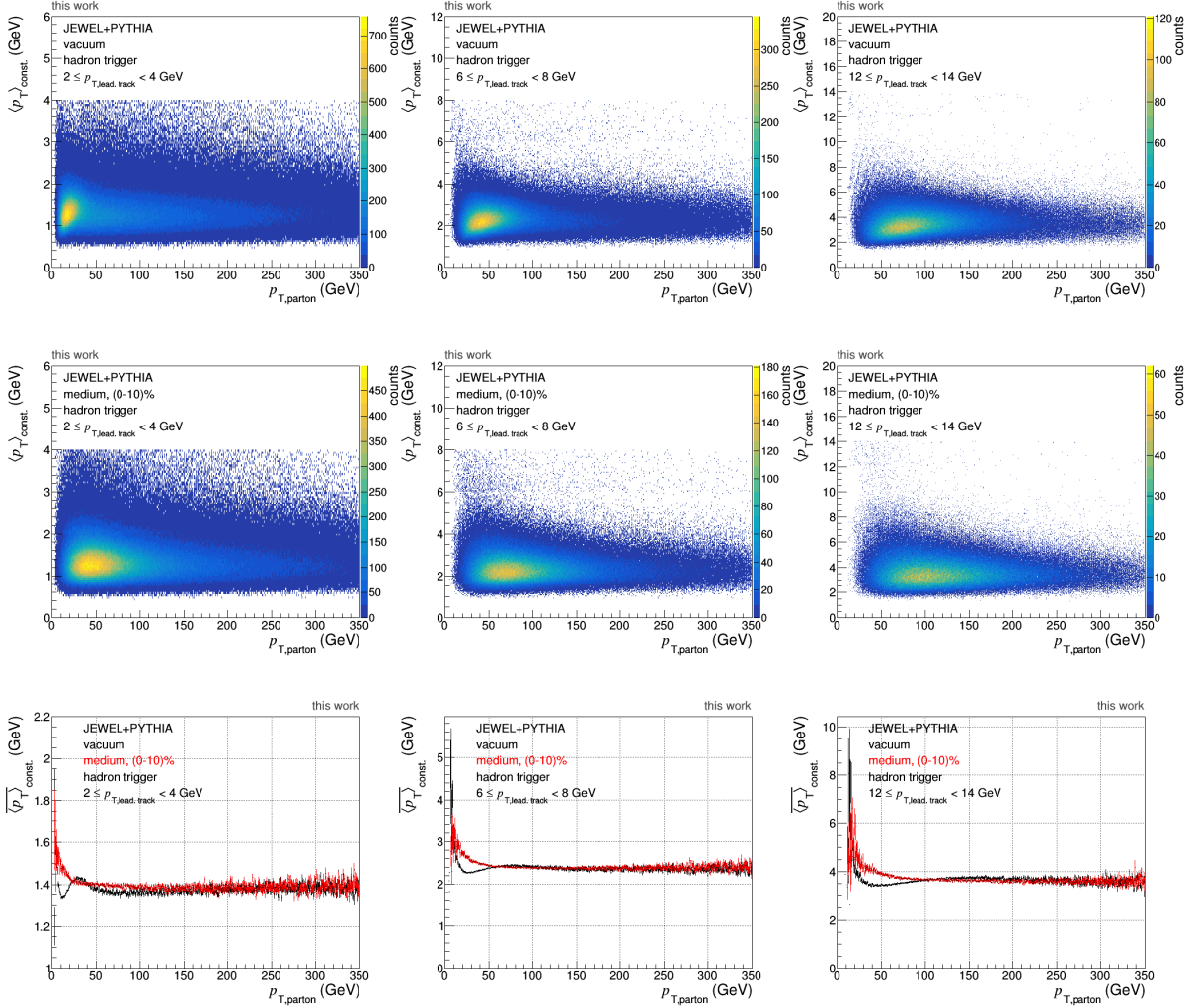


Figure 5.23: Top and middle: Average transverse momentum per jet constituent vs. the  $p_T$  of the corresponding parton, in vacuum and medium. Bottom: Mean average transverse momentum of the triggered jets constituents vs. the parton  $p_T$ .

### Average angular distance

The 2-dimensional distributions of the average angular distance of the triggered jet constituents for different parton  $p_T$  are plotted in the top and middle rows of Fig. 5.24. Consistent with the observations made for the triggered jet momentum, the predominantly triggered range in parton  $p_T$  broadens for the vacuum and medium case with increasing trigger  $p_T$ . The average angular distance decreases for both cases with increasing trigger  $p_T$ . The mean average angular distance is plotted in the bottom row of Fig. 5.24. There it can be seen that  $\langle \Delta\varphi_a \rangle$  changes from  $\sim 0.18$  to  $\sim 0.16$  when the trigger  $p_T$  increases from 2-4 GeV to 12-14 GeV. Since it was established that soft fragments get spread wider in the medium than harder fragments, it seems counterintuitive that constituents in jets originating from low  $p_{T, \text{parton}}$  have on average a smaller average angular distance to the jet axis in the medium case than in the vacuum case. The constituents of those jets are expected to be quenched significantly compared to the jets in

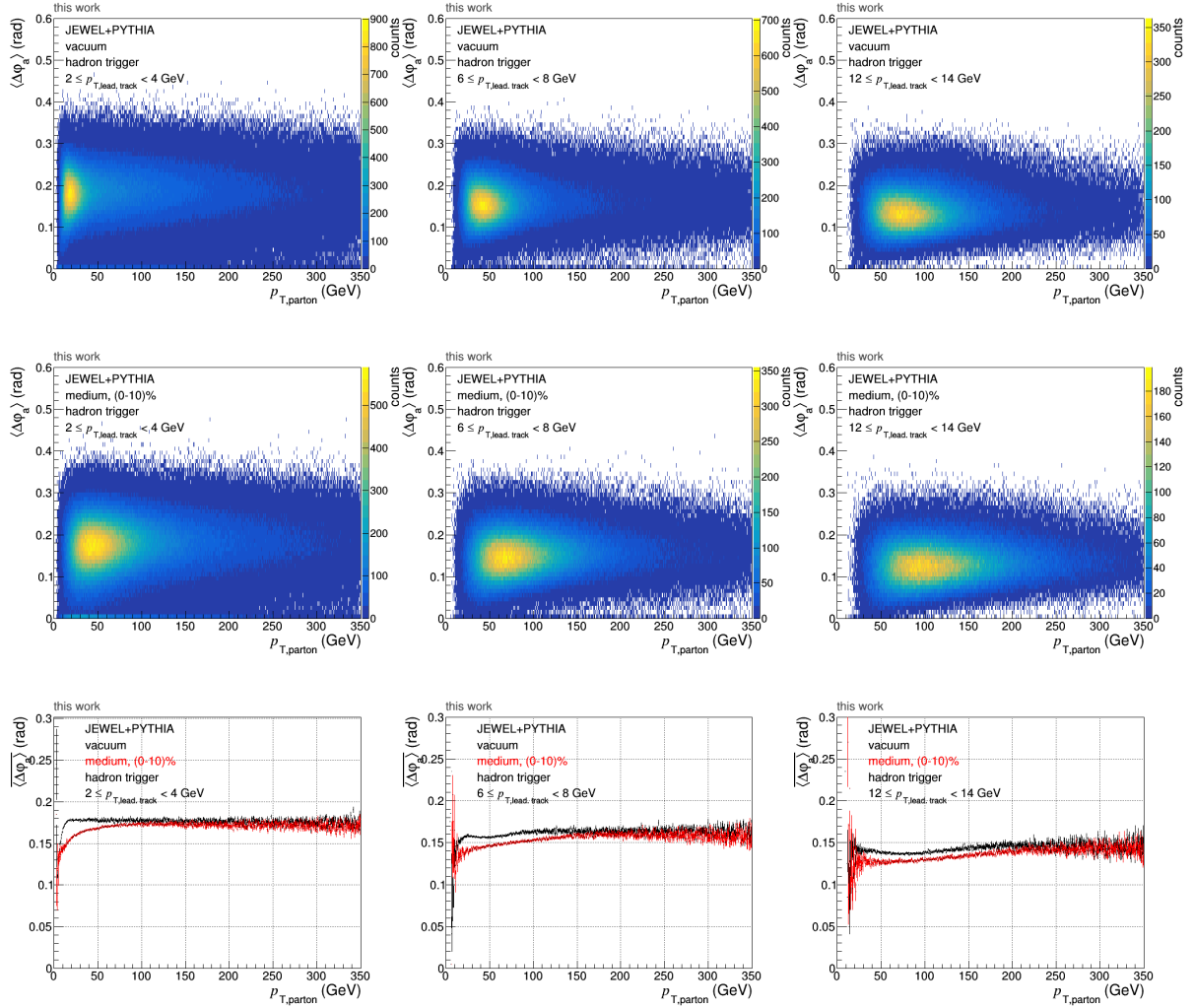


Figure 5.24: Top and middle: Average angular distance of the constituents of the triggered jet to the triggered jet axis vs. the  $p_T$  of the corresponding parton, in vacuum and in medium. The different trigger conditions are indicated on the plots. Bottom: Mean average angular distance of the triggered jets constituents vs. the partons  $p_T$ .

the vacuum case. However, for the interpretation of this finding the fragmentation and behavior of  $\langle\Delta\varphi_a\rangle$  for different jet  $p_T$  have to be considered.

The distributions of average angular distance for different jet and trigger  $p_T$  are shown for the vacuum and medium case in the top and middle row of Fig. 5.25. The distributions are very similar for both cases. The only difference visible in the 2-dimensional distributions is the larger range in jet  $p_T$  in the vacuum case. The mean average angular distance per jet  $p_T$  and for each trigger condition is shown in the bottom row of Fig. 5.25. There it is confirmed that the behavior across the trigger conditions and different jet  $p_T$  is very similar for the vacuum and medium case. However, it is observed that across all trigger conditions and for jet  $p_T < 30$  GeV, 60 GeV and 100 GeV, in the plots of the three trigger conditions respectively, the mean average angular distance of the triggered jet constituents is smaller in the medium case than in the vacuum case. These ranges correspond to the ranges found above, where a smaller number of constituents and higher average transverse momentum per jet constituent was found. This leads to the conclusion that the soft fragments of a parton, which is quenched to lower momentum, are scattered outside the cone of the reconstructed jet. A jet in vacuum, however still contains soft fragments, hence the lower average transverse momentum per constituent. Therefore, the average angular distance to the jet axis of the remaining constituents is, in the medium case, smaller than in the vacuum case. This also explains the lower  $\langle\Delta\varphi_a\rangle$  in the medium case compared to the vacuum case at low parton  $p_T$ . It was established that at low parton  $p_T$ , the average jet  $p_T$  is lower in the medium case than in the vacuum case. Since at low jet  $p_T$ , the average angular distance of the jet constituents is smaller in medium than in vacuum for the same jet  $p_T$ ,  $\langle\Delta\varphi_a\rangle$  is correspondingly lower in the medium case than in the vacuum case at low parton  $p_T$ .

### Summary

In this section, the influence of a hadron trigger on the general distributions, discussed in Section 5.2, was analyzed. It was found that the application of a trigger condition selects with increasing trigger  $p_T$  increasingly broad ranges in parton  $p_T$  and jet  $p_T$ . With increasing trigger  $p_T$ , the leading jets are selected with increasing probability as compared to the sub-leading jets. The fragmentation is very much dependent on the considered  $p_T$  range for both the parton and the triggered jet. For a parton in the medium case, the soft fragments are scattered outside the cone of the reconstructed jet. Therefore, for the same triggered jet  $p_T$ , jets in the medium case contain on average less particles but with higher average transverse momentum per constituent in the medium case than in the vacuum case. Correspondingly, the average angular distance of the constituents to the jet axis is in the medium case smaller than in the vacuum case for comparable jet  $p_T$ . Since for the same parton  $p_T$  the jets in the medium case have, on average, less transverse momentum than in vacuum, the constituents of the medium jet are on average located closer to than the constituents of the vacuum jet for the same parton  $p_T$  as well.

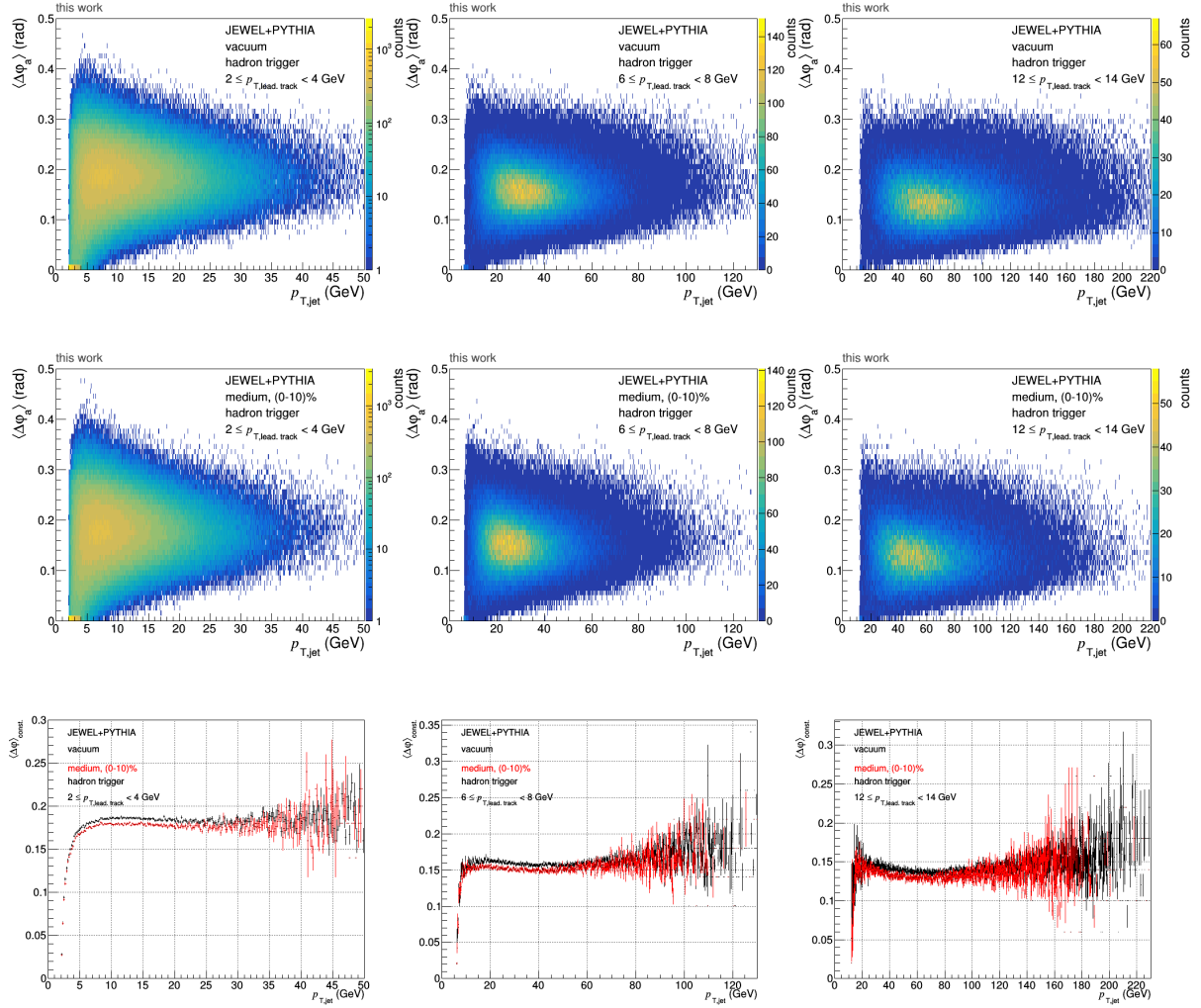


Figure 5.25: Top and middle: Average angular distance of the constituents of the triggered jet to the jet axis vs. the  $p_T$  of the triggered, jet, in vacuum and in medium. The different trigger conditions are indicated on the plots. Bottom: Mean average angular distance of the triggered jets constituents vs. the triggered jet  $p_T$

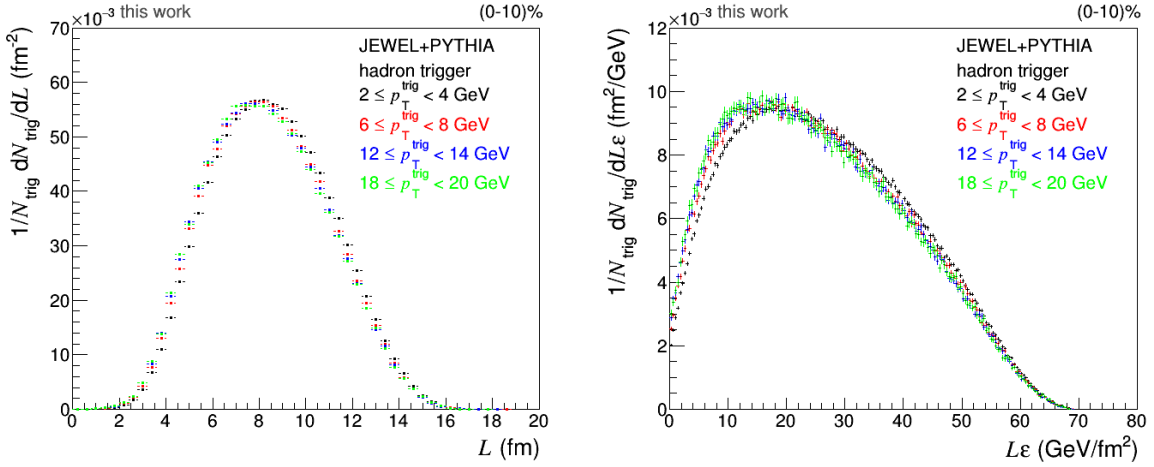


Figure 5.26: Path-length distributions for different hadron trigger conditions. The left plot shows the distribution of the geometrical path-lengths, the right plot the distribution of weighted path-lengths.

### 5.4.2 Hadron triggered path-length distributions

Since the goal is to measure different path-lengths with different trigger conditions and correlation functions, it needs to be specified what path-length is actually selected with a certain trigger condition. This was studied with the geometrical and energy-density weighted path-length distributions, generated for the partons corresponding to the triggered jets that were triggered with the different trigger conditions. A selection of distributions can be seen in Fig. 5.26. The left plot shows the distributions of the simple geometrical path-length, the right plot the distributions of the weighted path-length.

The distributions for all trigger conditions are very similar. It was found before that a trigger hadron selects a broad range in jet  $p_T$  and parton  $p_T$ . The path-length, which is assigned to the hadron trigger and triggered jet, depends very much on the individual parton  $p_T$  and jet  $p_T$  considered in each case. The fact that the distributions for the different trigger conditions are so similar is a first indicator that only a single hadron trigger without further information is not suited to measure the path-length differences between different jets. This is discussed in further detail below. A small shift is, however, visible of the weighted path-length distribution for  $2 \leq p_T^{trig} < 4 \text{ GeV}$  to higher values of  $L\varepsilon$  compared to the other distributions. Since jets with this trigger condition do not contain particles with a momentum larger than  $p_T = 4 \text{ GeV}$  and therefore have an overall very small momentum (smaller than the usual application range of JEWEL), it is possible that these jets are actually only clusters of random soft fragments outside of the jet cone. When these clusters are matched to a parton, on average higher energy densities are necessary to quench the parton to the cluster momentum, hence the shift of the distribution.

To get a clearer picture in general of the shift in the selected path-length with changing trigger conditions, the mean of each distribution is compared for all trigger conditions. The associated plots are shown in Fig. 5.27. The top row shows the mean and widths of

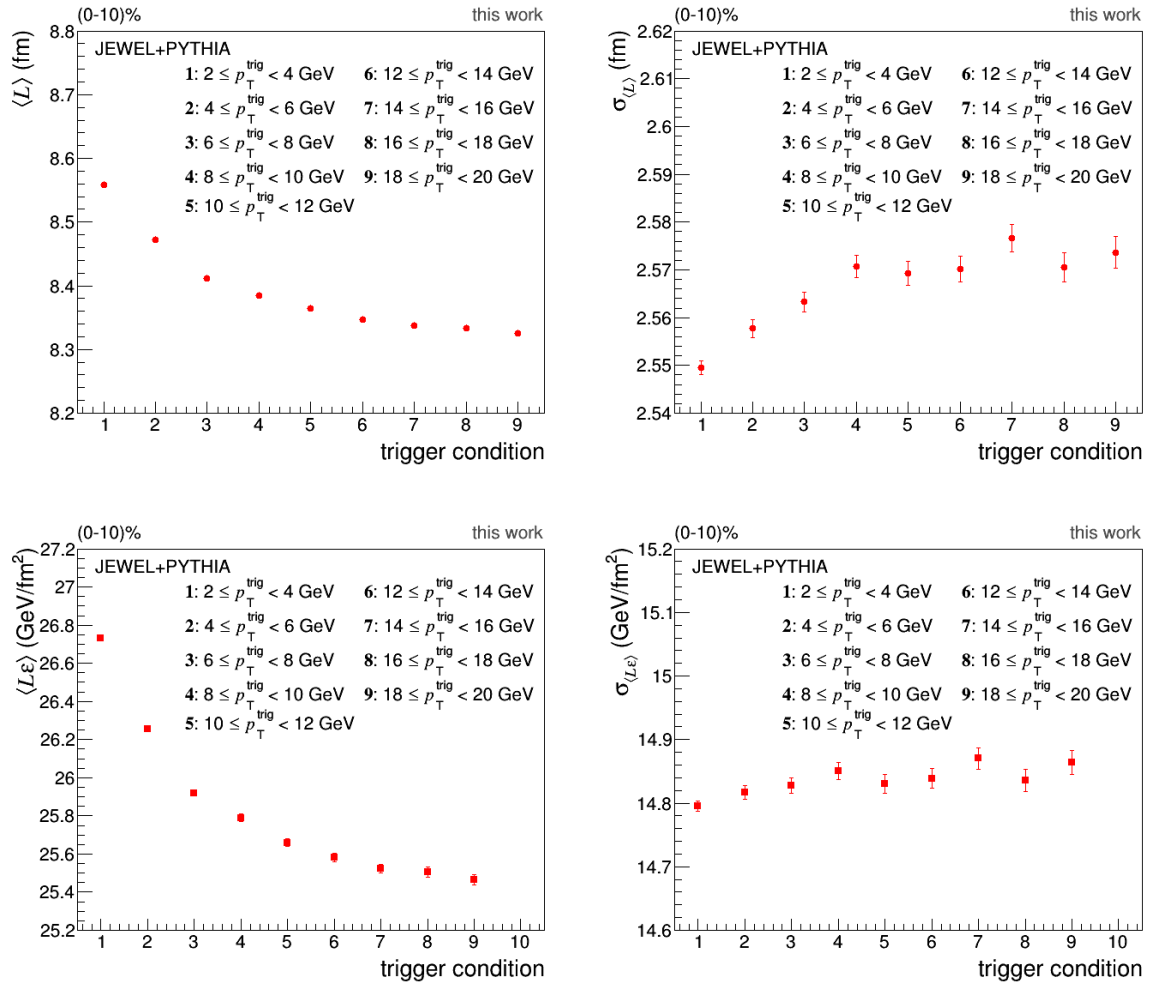


Figure 5.27: Mean and standard deviation of the (weighted) path-length distributions for different trigger conditions. The top row corresponds to the simple geometrical path-length, the bottom row corresponds to the energy-density weighted path-length.

the distributions of the geometrical path-length, the bottom row the means and widths of the weighted path-length. On average, a trigger hadron with high  $p_T$  selects a shorter (weighted) path-length than a trigger with comparatively lower  $p_T$ . It was found that with the hardness of the trigger hadron, the momentum of the triggered jet increases on average. In comparison with the average triggered parton  $p_T$ , jets transferred less momentum to the medium than jets which have a lower  $p_T$  leading track. Therefore, the path-length of high  $p_T$  jets is, on average, smaller. However, when comparing the maximum shift of the mean to the average width of the distributions, one observes that the average width of a (weighted) path-length distribution is  $\sim 10$  times higher than the shift in mean between the lowest (2-4 GeV) and highest (18-20 GeV) trigger condition. Thus, solely with the evaluation of jets via single hadron triggers, statements about the mean path-length corresponding to this trigger particle can be made, but the measurement is very imprecise. The width of the geometrical path-length distribution increases with increasing hardness of the trigger particle, while the width of the weighted distributions increases only very slightly. This can be interpreted as follows. When comparing the average triggered jet momentum of a low  $p_T$  trigger hadron to the average parton momentum, in most of the cases a large experienced energy density is necessary to quench the jet to the observed momentum. Jets with a high  $p_T$  leading track can originate either from very energetic partons, that transferred a large amount of their momentum to the medium, or they can originate from less energetic partons that only transferred a small amount of their momentum to the medium. Therefore, the range in experienced energy density is larger for high  $p_T$  trigger hadrons. This translates not to a large absolute increase of the weighted path-length distributions width, but more strongly as a relative increase of the width with respect to the mean weighted path-length selected. This means that, although jets with high  $p_T$  leading tracks can be generated via both processes, the latter occurs more frequently. In the widths of the geometrical path-length distributions, the increase is observed as absolute change of the width.

### 5.4.3 Path-length with respect to the event plane

Clearly, only the selection of a hadron trigger without further information is not sufficient to study the in-medium path-length of partons in much detail. In Section 3.3, the investigation of triggered jets with respect to the event plane was already discussed as an option to study the path-length with a single hadron trigger. The additional information of the jet angle potentially allows for a more differential and precise analysis. The event plane study is done in simulations with both (0-10) % centrality and (50-60) % centrality. The additional parameter used is the jet angle, relative to the event plane:  $\Delta\phi = |\varphi_{\text{jet}} - \Psi_{\text{event plane}}|$ . Since the angle of the event plane is always zero in JEWEL,  $\Psi_{\text{event plane}} = 0$ ,  $\Delta\phi$  is the angle of the jet, reduced to the interval  $[0, \pi/2]$ . The path-length is evaluated in bins of  $\pi/12$  ( $15^\circ$ ) of the relative jet angle. The first bin ( $\Delta\phi \in [0, \pi/12]$ ) corresponds to jet  $\varphi$  closest to the event plane (“in-plane”), while  $\Delta\phi = |\varphi_{\text{jet}} - \Psi_{\text{event plane}}| \in [5\pi/12, \pi/2]$  corresponds to jets located transverse to the event plane (“out-of-plane”).

The distributions for the path-length of any jet (i.e. no selection criterion is applied), for (0-10) % and (50-60) % centrality are shown in Fig. 5.28. Since the overlap region

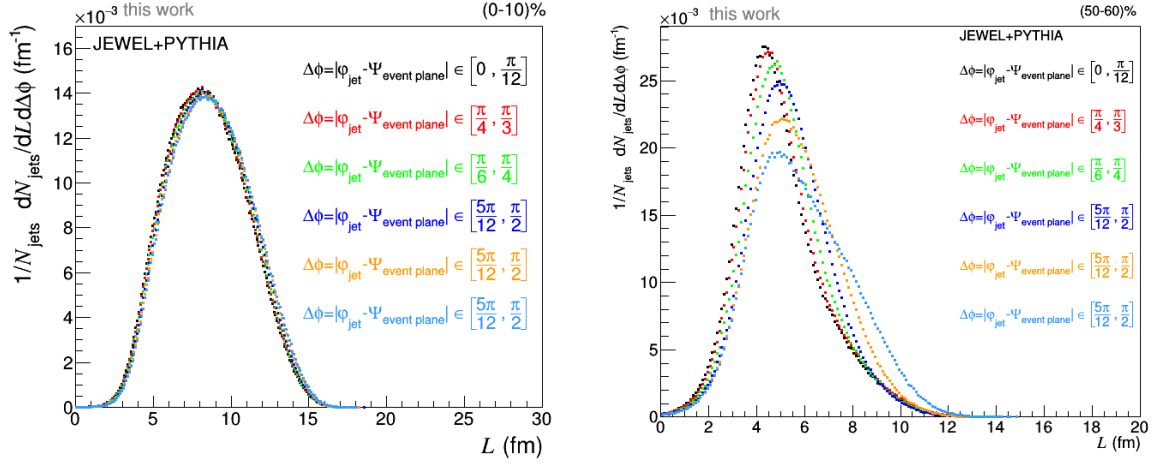


Figure 5.28: Untriggered path-length distributions in different bins of jet  $\varphi$  relative to the event plane. Left: (0-10) % centrality. Right: (50-60) % centrality.

for the (0-10) % centrality interval is quite symmetrical, the path-length distributions corresponding to the two bins most in-plane and most out-of-plane are very similar. For (50-60) % centrality, the peak of the path-length distribution shifts to higher values for more out-of plane intervals. At the same time, the shape of the distribution changes. With increasing relative jet  $\varphi$ , the distribution develops a tail towards higher path-lengths. This is due to the highly asymmetric shape of the overlap region in this centrality interval. Although the opening angle of each distribution is the same, the path-lengths at the limits of each bin in  $\Delta\phi$  are different. For the bin most in plane, the path-lengths corresponding to  $\Delta\phi = 0$  and  $\Delta\phi = \pi/12$  are very similar. In the bin most out-of-plane, the path-length corresponding to  $\Delta\phi = 5\pi/12$  is much smaller than the path-length corresponding to  $\Delta\phi = \pi/2$ . Therefore, the distribution for in-plane bins is rather symmetric with only a small tail towards higher  $L$ , while the distribution becomes increasingly asymmetric for more out-of-plane bins.

The means and widths of the path-length distributions for both centrality intervals are plotted in Fig. 5.29. The mean of the distributions for both centralities is shifted towards higher values for the more out-of plane bins. The effect is much more prominent in the simulations with a peripheral medium. Due to the geometry of the overlap region, the most out-of-plane bin in  $\Delta\phi$  corresponds to the largest path-length, while the in-plane bin corresponds to the small path-lengths. In peripheral events, the overlap region is much more asymmetric and the difference between in-plane and out-of-plane is larger than in central events. The correspondence between  $\Delta\phi$  and path-length can be seen directly in the shift of the means. Between the most in-plane bin and the most out-of plane bin, for (0-10) % the mean shifts by  $\sim 0.34$  fm, for (50-60) % by  $\sim 0.95$  fm. The width for (0-10) % is mostly constant at  $\sim 2.56$  fm, only for the two most out-of plane bins it increases slightly by up to 0.04 fm. The width for (50-60) % increases overall by  $\sim 0.27$  fm from the first bin in  $\Delta\phi$  to the last bin. However, for two bins (3 and 4), the width decreases again. When comparing the path-length distributions in these bins to the other distributions, there the shift in mean path-length is predominantly caused

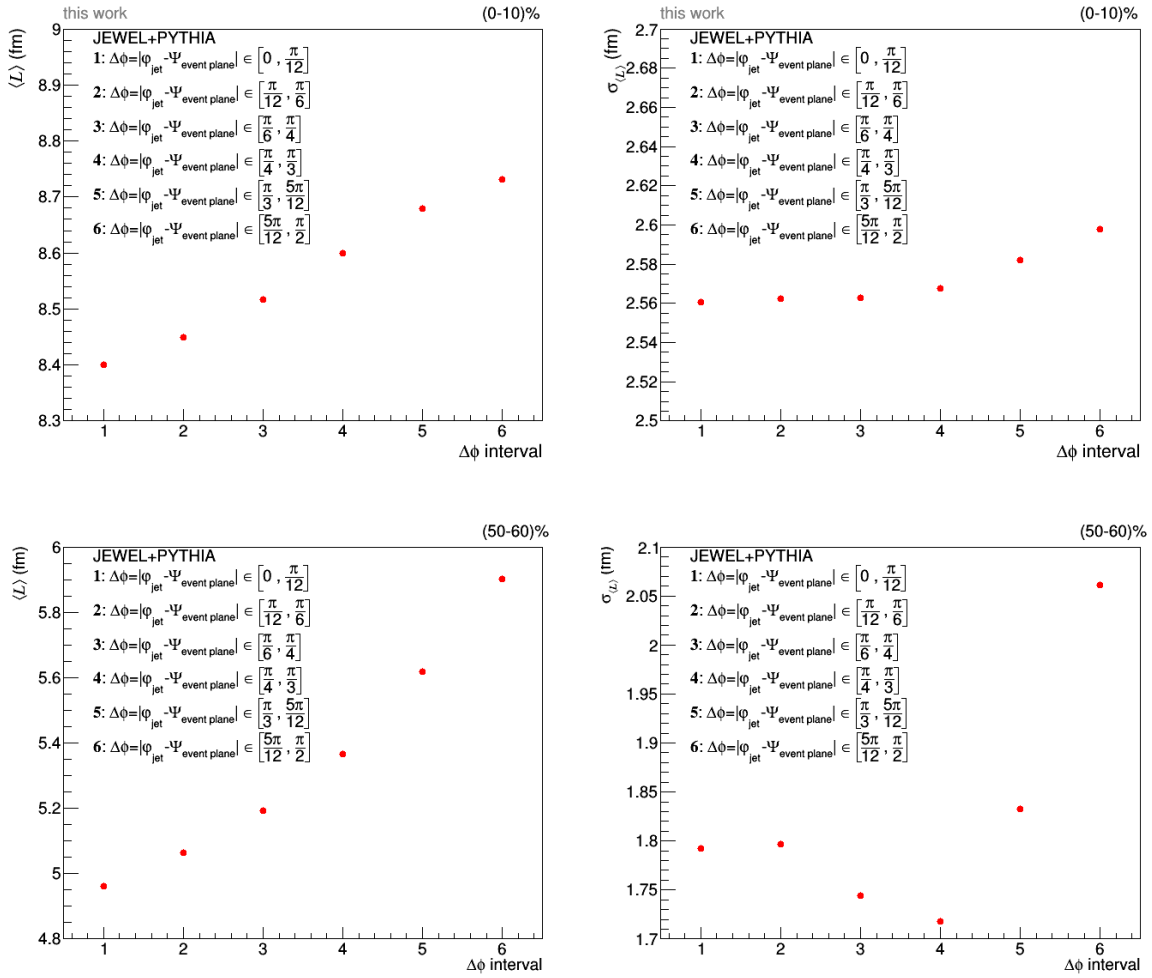


Figure 5.29: Mean and standard deviation of the untriggered path-length distributions in the different bins of  $\Delta\phi$ . Top: (0-10)% centrality. Bottom: (50-60)% centrality.

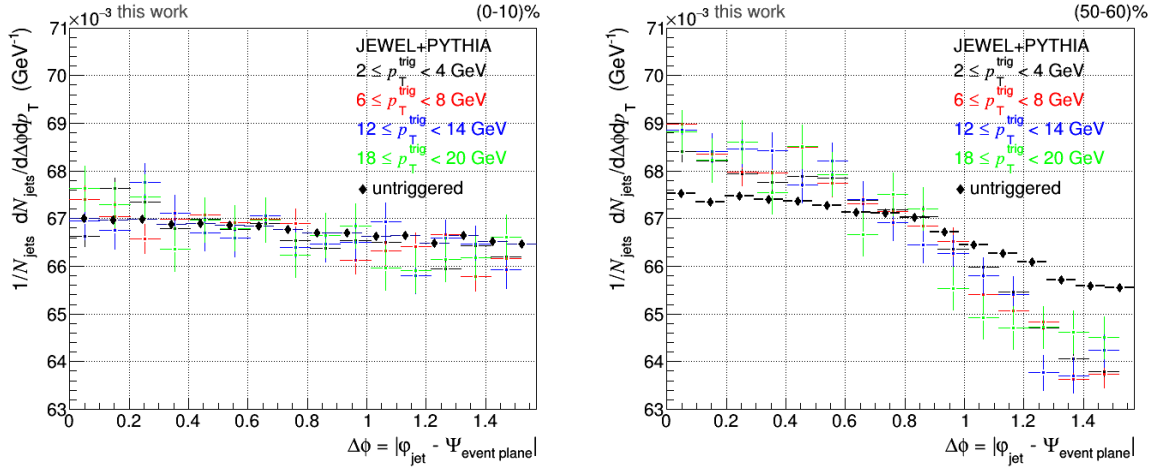


Figure 5.30: Distribution of triggered and untriggered jets in angle wrt. the event plane. Left: (0-10) % centrality. Right: (50-60) % centrality.

by a shift of the peak, while for the other bins the broadening of the distribution is the main factor. The overall increase of the width can be explained with the geometry, as was already done above. More complicated cases are the two  $\Delta\phi$  bins, where the shift in mean is predominantly caused by a shift of the peak and not by a broadening of the distribution. This is explained in the following. The mean of the distribution is the indicator, which path-length corresponds on average to the selected  $\Delta\phi$  bin. The peaks, however, indicate which path-length most of the jets are associated with. The distributions shown in Fig. 5.28 are the average of all jets. Depending on the momentum profile of the simulation, a specific average jet momentum can be assigned to the average jet. As different bins in  $\Delta\phi$  correspond to different path-lengths, the bins also correspond to varying amounts of momentum which is transferred from an average parton to the medium. When comparing the momentum of an average jet to the average momentum of a parton, the momentum difference between the two therefore corresponds to a specific path-length and, accordingly, to a specific bin in  $\Delta\phi$ . In the corresponding bin, most of the jets then have a path-length close to mean path-length associated with an average jet and the width decreases. The number of  $\Delta\phi$  bins over which the width is observed to be decreasing is an indicator for the width of the average  $p_T$  range. When comparing the shift in the mean to the width of the distributions, the comparison of the most out-of-plane bins in events with different centrality constitutes on this general basis the most promising way to measure the path-length.

To quantify how the path-length distribution with respect to the event plane changes when applying a trigger condition to the selected jet, first the distribution of differently triggered jets with respect to the event plane is examined. Since more out-of-plane bins correspond to larger path-lengths and therefore on average more transferred momentum, it is expected that the jets triggered with high  $p_T$  have a stronger dependence on the event plane than jets triggered with lower  $p_T$ . The distribution of triggered jets within a certain relative angle to the event plane is plotted for (0-10) % and for (50-60) % in Fig. 5.30. For comparison, also the distribution for all jets (no restriction on the selection) is

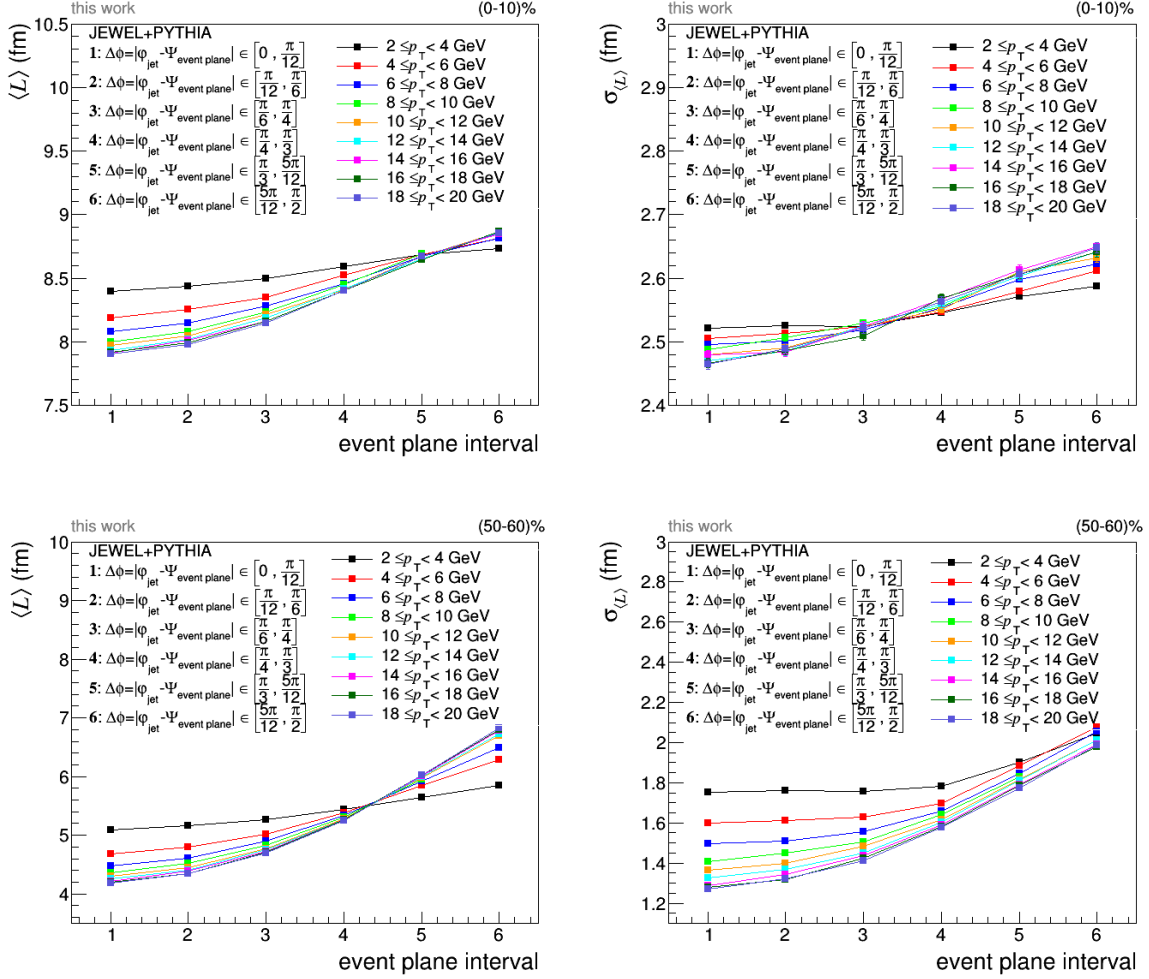


Figure 5.31: Mean and standard deviation of the path-length distributions for different trigger conditions and in the six different bins of the jet angle relative to the event plane. Top: (0-10)% centrality. Bottom: (50-60)% centrality.

shown. For (0-10)%, only a small shift between any trigger condition and the untriggered distribution and no significant shift in between different trigger conditions is visible. For (50-60)%, a larger shift is visible between the untriggered and triggered distributions. As well, no significant shift is observed between the different trigger conditions.

Like was done before for a general jet (Fig. 5.28), a path-length can be assigned to the triggered jets in the different  $\Delta\phi$  bins and for the different trigger conditions. The means and widths of those distributions are shown in Fig. 5.31. The observed shift in the mean path-length between different bins of relative jet  $\varphi$  is more prominent for (50-60)% than for (0-10)%. Although in the distribution of jets per  $\Delta\phi$ , no visible shift between the distributions for different trigger conditions was observed, there is a small though visible difference for the mean path-length. For both (0-10)% and (50-60)%, the shift in mean path-length is largest for the highest trigger  $p_T$  with 18-20 GeV between the most in-plane and most out-of plane  $\Delta\phi$  bins. For (0-10)% this is  $\sim 0.9$  fm and for (50-60)% the difference is  $\sim 2.6$  fm. The bin, after which the highest  $p_T$  trigger have a larger

path-length than the lowest  $p_T$  trigger is met earlier for (50-60) % than for (0-10) % (bin 4 vs. bin 5). This is due to the different asymmetries of the overlap regions for the two centralities. In (50-60) %, the path-length difference between two bins is larger than for (0-10) %. The behavior for the different trigger conditions is consistent with the previously stated findings and assumptions. The widths of the distributions increase for both centrality intervals with increasing relative jet  $\varphi$ . In both cases, the width for 2-4 GeV trigger momentum increases least with more out-of-plane bins, while the increase of width is more steep for higher trigger momenta. Due to the same symmetry argument, the behavior of the “crossing point” is inverse to what was observed for the mean path-length. Distributions from high trigger  $p_T$  reach the comparatively higher width earlier for (0-10) % (bin 3), than for (50-60) % (bin 6 or, hypothetically, later). When comparing the shift of the means and the widths of the distributions, two observables emerge as promising tool to study the in-medium path-length of jets with single hadron triggers and the additional information of the relative jet  $\varphi$ . The difference of the mean path-length of a triggered jet with high  $p_T$  leading track of the most in-plane  $\Delta\phi$  bin to the most out-of plane bin is for (50-60) % centrality larger than the widths of the corresponding path-length distributions. Therefore, the analysis of high  $p_T$  trigger particles with respect to the event plane in peripheral events is a good choice to measure the in-medium path-length of jets. The other possibility is the comparison of the same trigger condition in the same bin of  $\Delta\phi$  for different intervals of centrality. Especially for the most in-plane bin,  $\Delta\phi \in [0, \pi/12]$ , the difference in mean path-length for the two different centrality intervals is considerably larger than the widths of the distributions. For the lowest bin in trigger  $p_T$ , the difference of the mean path-lengths (3.3 fm) is 1.3 times as large as the width of the distribution for (0-10) % centrality and almost twice as large as the width of the distribution for (50-60) % centrality. To study this with correlation functions, the shift of observables obtained from correlation functions will be investigated for the same set of trigger conditions and bins in relative jet  $\varphi$  in Section 5.5.

#### 5.4.4 Dihadron trigger

The other trigger condition, which was discussed in Section 3.3 as promising tool to study the in-medium path-length of jets, is a back-to-back dihadron trigger. For this trigger condition, two hadrons in two specific momentum intervals are selected,  $p_T^{\text{trig } 1}$  and  $p_T^{\text{trig } 2}$ . Both hadrons are again required to be the leading track of the jet they are contained in. Furthermore, the two hadrons which lie in their respective momentum interval have to be back-to-back in azimuth. This is done by checking if the difference of their azimuthal angles is less than  $\pi \pm \frac{\pi}{8}$ :

$$\Delta\varphi_{\text{trig}} = ||\varphi_{\text{trig } 2} - \varphi_{\text{trig } 1} - \pi| < \frac{\pi}{8} \quad (5.12)$$

With the application of different momentum trigger conditions to the two hadrons, one can potentially select different jet momenta and, provided the hadrons originate from the same dijet system, different path-lengths. In the previous section, it was already checked that a single hadron trigger with varying momentum indeed selects (predominantly leading) jets in different momentum ranges. However, it was also found that the

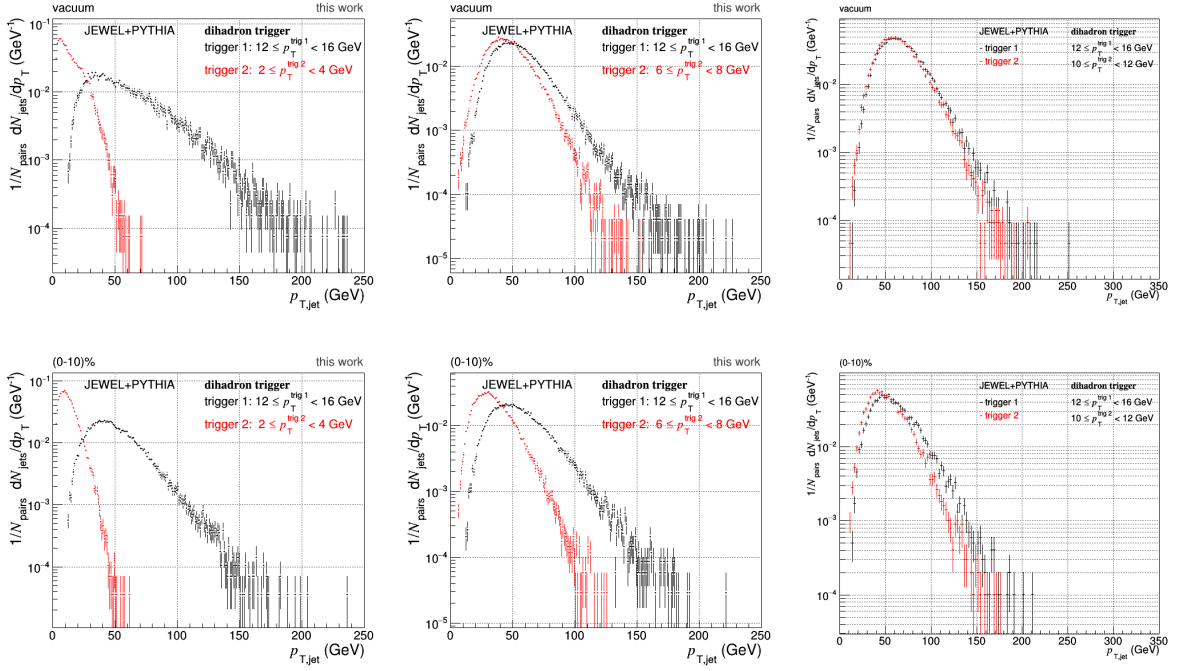


Figure 5.32: Jet momentum for different combinations of back-to-back dihadron trigger conditions. Top: vacuum. Bottom: (0-10) % medium.

corresponding parton has a large range in  $p_T$ . The picture is different, though, when selecting two trigger hadrons, at least in this analysis. Since JEWEL only simulates one dijet system per event, in this analysis it is ensured that the two triggered jets indeed originate from the same hard scattered parton pair. In real data analysis or even simulations which generate more than one dijet system per event, the mapping is not as explicit. In simulations, one can check the associated parton momentum, to make sure the two triggered jets originate from the same parton pair. Since the parton momentum itself is not accessible to measurements, this is not possible in real data analysis. There, the only way to ensure that the hadrons originate from the same dijet system is to restrict the range of the azimuthal angle difference and estimate the fraction of mismatched hadron pairs by comparison with simulations. However, as was said before, in JEWEL and therefore in this analysis this complication does not arise. To check, if the momenta of the triggered jets are consistent with what was found for a single hadron trigger, the jet  $p_T$  spectra for different combinations of trigger conditions are investigated.

The distribution of the triggered jet momentum for different combinations of  $p_T^{\text{trig } 1}$  and  $p_T^{\text{trig } 2}$  are shown in Fig. 5.32. The top row corresponds to dijet systems in the vacuum case, the bottom row to the (0-10) % medium. In the left column, the most asymmetric trigger momentum intervals, 12-16 GeV for trigger 1 and 2-4 GeV for trigger 2, are used, in the right column, the most symmetric momentum combination, 12-16 GeV and 10-12 GeV, is displayed. In consistency with the single hadron trigger, trigger particles with higher momentum have a wider range in jet  $p_T$  and, on average, select jets with higher momentum than a trigger particle with comparatively lower momentum. Therefore, the asymmetry of the trigger conditions is reflected in the distribution of

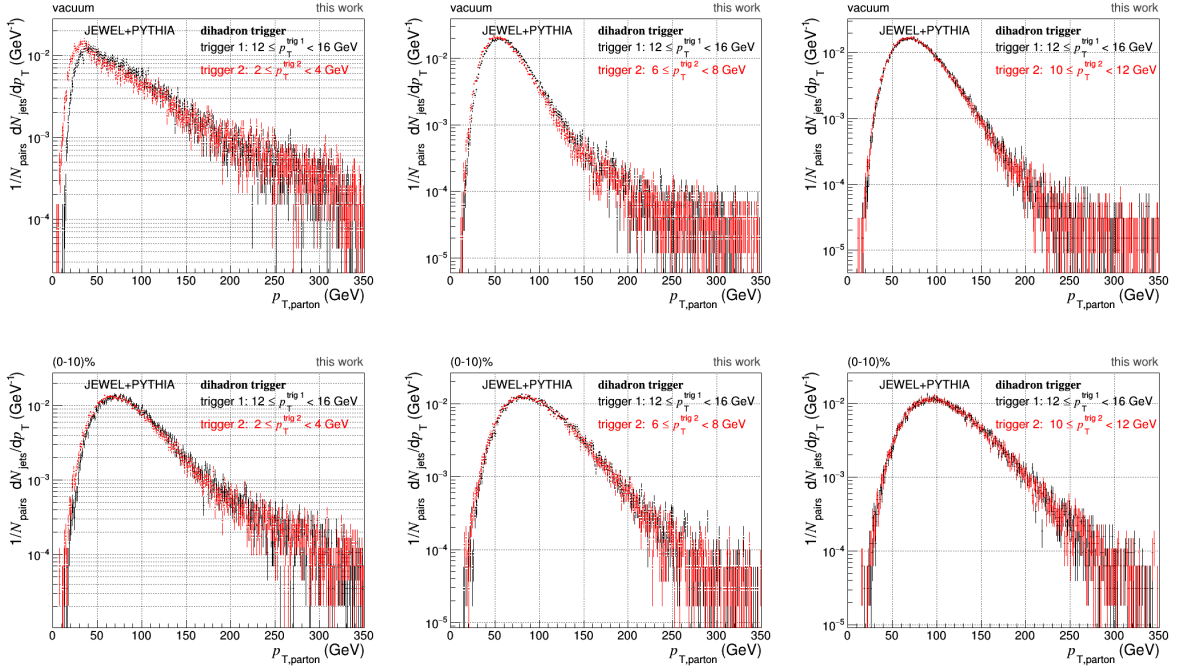


Figure 5.33: Parton momentum for different combinations of back-to-back dihadron trigger conditions. Top: vacuum. Bottom: (0-10) % medium.

triggered jet momentum. In the vacuum case, the triggered jet momentum adapts more rapidly with proceeding symmetry. For  $12 \leq p_T^{trig1} < 16$  GeV and  $6 \leq p_T^{trig2} < 8$  GeV, the distributions are almost congruent in the vacuum case, while the peak is still shifted by  $\sim 20$  GeV in the medium case. It is remarkable that, although the trigger momentum of trigger 1 is constant across all combinations, the jet  $p_T$  distribution shifts nonetheless also for trigger 1 when changing trigger 2. From the most asymmetric case to the most symmetric case, the peak of trigger 1's distribution is shifted by  $\sim 10$  GeV towards higher  $p_T$ . This indicates that a variation of trigger 2's momentum influences the path-length of both triggered jets. Furthermore, it was found previously that the same trigger condition applied to the same parton momentum yields lower jet momenta in the medium case than in the vacuum case. The fact that the dihadron trigger conditions select so similar ranges in vacuum and in medium implies that the underlying parton  $p_T$  range is different in both cases. This is confirmed with the distributions of parton momenta associated with the two trigger hadrons for varying trigger conditions, as shown in Fig. 5.33. For the same trigger condition, the selected average parton  $p_T$  is larger in the medium case than in the vacuum case for all trigger conditions. Only the shift of the peak from most asymmetric to most symmetric trigger conditions is similar in both cases ( $\sim 30$  GeV). This complicates the determination of medium modifications. The change of an observable between medium and vacuum for a specific trigger condition cannot be taken as measure, since the underlying system is not the same. Instead, only the relative changes between different trigger conditions in vacuum and medium can be compared.

The path-length corresponding to a triggered jet is determined in the same way as before. The distributions of (weighted) path-length for trigger 1 and trigger 2 are shown

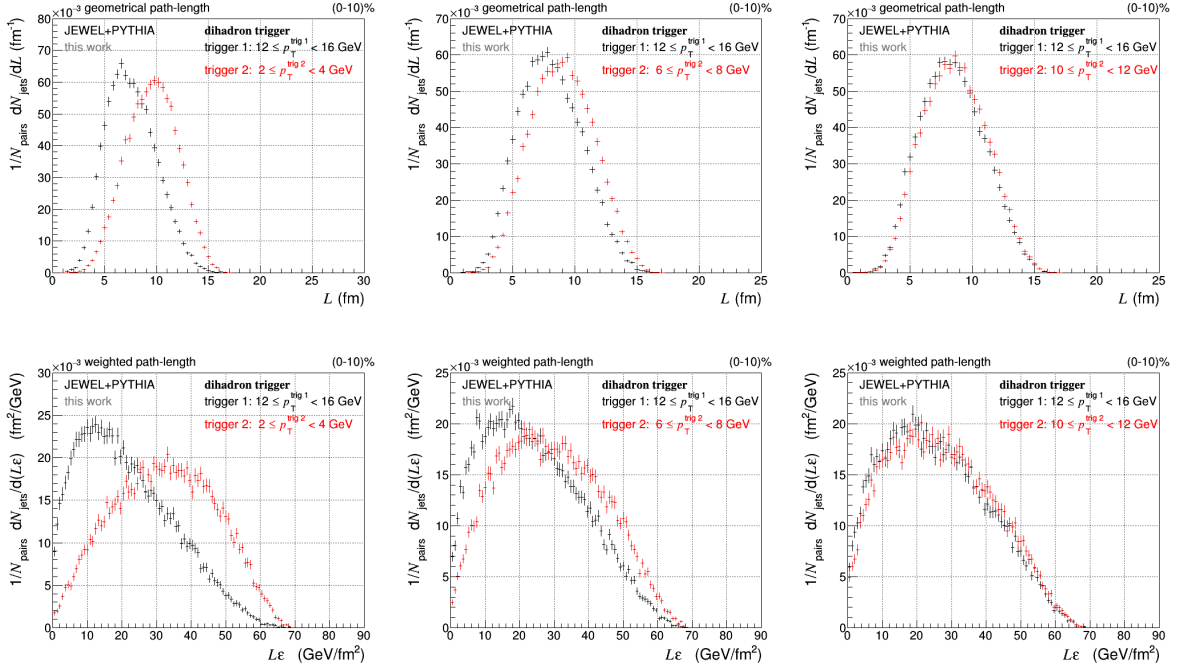


Figure 5.34: Path-length distributions for different combinations of back-to-back dihadron trigger conditions in (0-10)% centrality. Top: Geometrical path-length. Bottom: Energy-density weighted path-length.

in Fig. 5.34 for different trigger momentum combinations. The asymmetry of the trigger conditions and the triggered jet momentum is reflected in the distributions for the (weighted) path-length. The higher the momentum of the triggered jet, the lower the corresponding (weighted) path-length. For the most asymmetric trigger momentum bins, the peaks of the distributions are shifted by  $\sim 3$  fm. For the most symmetric bin, the distributions are almost congruent. In the distributions of jet momentum it was indicated that the momentum selection of trigger 2 influences the path-length of trigger 1, even for a constant  $p_T^{\text{trig}}$  interval. This is confirmed in the distributions. The peak of the geometrical path-length distribution for trigger 1 shifts from  $\sim 7$  fm to  $\sim 8$  fm. This shift is smaller than for trigger 2, where the peak is displaced by 2 fm. However, although the shift for trigger 1 is smaller than for trigger 2, this shows that for different trigger conditions, the path-length of trigger 1 cannot be taken as constant comparison value to draw the connection between the absolute path-length and energy loss with the different jets triggered by hadron 2. Instead, only statements about the relative change in path-length can be made.

The behavior of the weighted path-length distributions is very similar to the behavior of the distributions for the geometrical path-length. For a low  $p_T$  hadron as trigger 2 (left plot), the mean energy density experienced over its path is higher than for trigger 1. Since the jets containing the trigger hadrons originate from two partons with similar momentum, the difference in experienced energy-density over the path results in different amounts of momentum transferred from the jets to the medium and therefore different jet momenta. This is consistent with the observations made above. For more symmetric

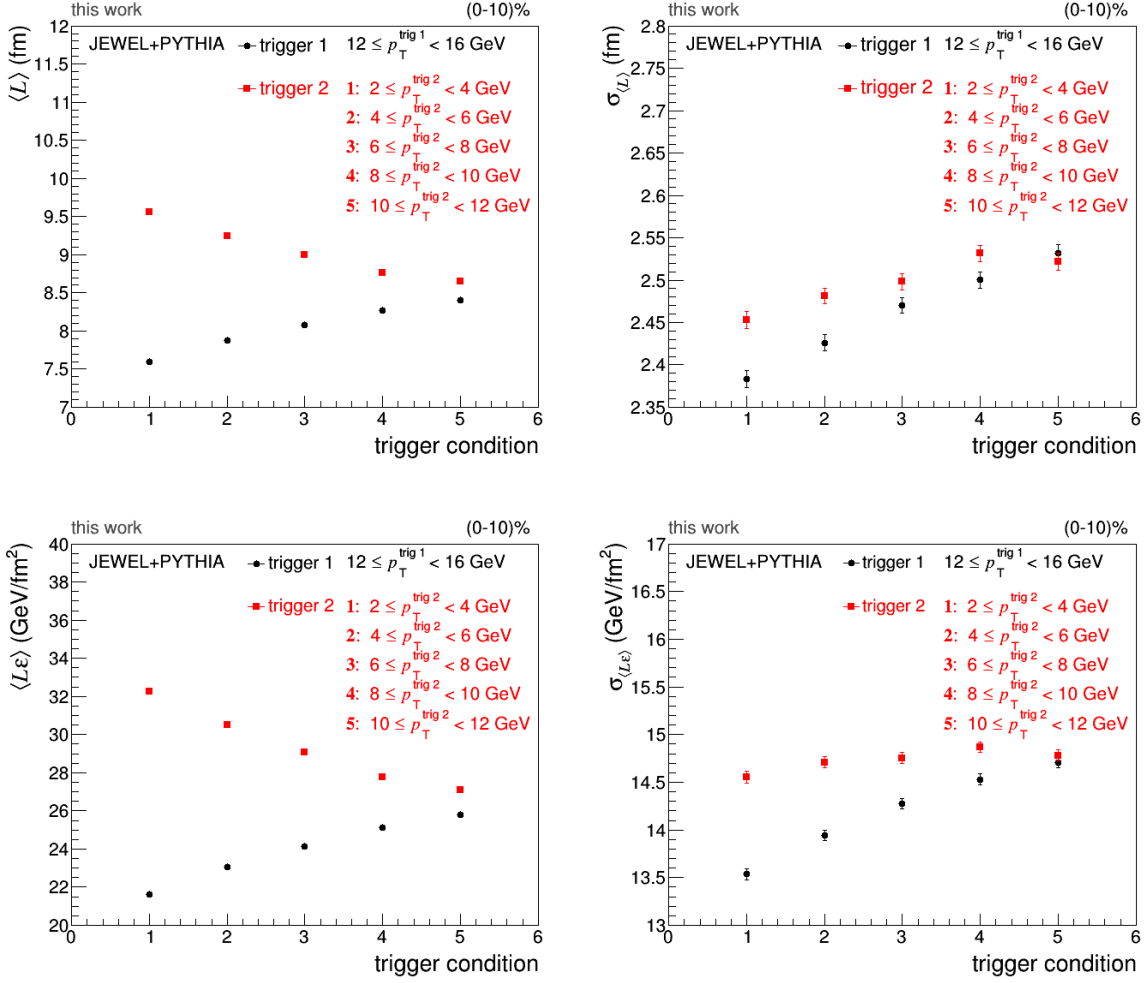


Figure 5.35: Mean and standard deviation of the path-length distributions for different back-to-back dihadron trigger conditions. Top: Geometrical path-length. Bottom: Energy-density weighted path-length.

trigger conditions and therefore similar triggered jet momenta, the experienced energy density aligns accordingly for triggers 1 and 2. It is noticeable that the weighted path-length distributions, by comparing the peak position to the width, are much wider than the geometrical path-length distributions. This is due to the different values of energy density at different positions in the overlap region. For the geometrical path-length, the deciding factors for the path-lengths reached by jets triggered with a specific hadron pair, are the scattering position and the angles of the partons. When, however, the energy-density is added to the picture, small shifts in vertex position and angle can result in large differences of the energy density experienced. Therefore, a relatively small range in geometrical path-length is expanded to a considerably larger range when the energy density is taken into account.

To get an impression how precise path-length differences can be measured between different trigger conditions, the means of the (weighted) path-length distributions are again compared to the widths. It should be noted that, due to the slightly asymmetrical

shape in the case of simple geometrical path-length and the very asymmetrical shape of the weighted path-length distributions, the mean is not necessarily the same as the peak position. Therefore, the shift in mean can be smaller than what was observed for the peak position. However, for the comparison with real data, the (weighted) path-length which is on average accessed with a certain trigger condition, provides the more well-defined quantity. The distributions of the mean (weighted) path-length and the associated widths are shown in Fig. 5.35. Like it was seen in the path-length distributions, the difference in path-length decreases for more symmetric trigger conditions. The difference in mean geometrical path-length drops from  $\sim 2$  fm for  $2 \leq p_T^{\text{trig } 2} < 4$  GeV to  $\sim 0.3$  fm for  $10 \leq p_T^{\text{trig } 2} < 12$  GeV. For the weighted path-length, the mean drops from  $\sim 11$  GeV/fm<sup>2</sup> to  $\sim 1.5$  GeV/fm<sup>2</sup>. In both cases, the shift in mean path-length difference between asymmetric and symmetric trigger conditions is approximately of the order of the average width of the corresponding distributions. The widths of the geometrical path-length distributions increase for both trigger particles and for increasingly symmetric trigger conditions. The difference in width is approximately equal for both trigger particles between the most asymmetric and the most symmetric trigger conditions. Meanwhile, the widths of the weighted path-length distributions increase as well for both trigger particles and for increasingly symmetric trigger conditions, but the increase is much larger for trigger 1 than for trigger 2 ( $\sim 1.1$  fm vs.  $\sim 0.4$  fm).

One further interesting observation can be made when looking at the 2-dimensional distributions of the weighted and geometrical path-length for different trigger conditions, Fig. 5.36. Like it was done in Section 5.3, the minimum value is plotted against the maximum value. The distributions are in all cases very similar to the general distributions shown in Fig. 5.13 and Fig. 5.16. Furthermore, there is no difference visible between the different trigger conditions. This indicates that the effect of surface bias, discussed in Section 3.3, is not as prominent as it is generally assumed, e.g. [58–60]. If it was, there would be a shift of the distribution to large  $L_{\text{max}}$  and at the same time small  $L_{\text{min}}$  visible for the most asymmetric trigger conditions. The differences in mean path-length for trigger 1 and 2 and between different trigger conditions in general are not as large as the discussed differences for triggered jet with respect to the event plane (see above). This leads to the conclusion that single hadrons, studied with respect to the event plane, may actually be suited better to study the path-length of hard scattered partons than dihadron triggered jets. However, for a definitive statement this still has to be compared to the conclusions obtained with the study of correlation functions. In the next section, the generation and evaluation of correlation functions is described in detail.

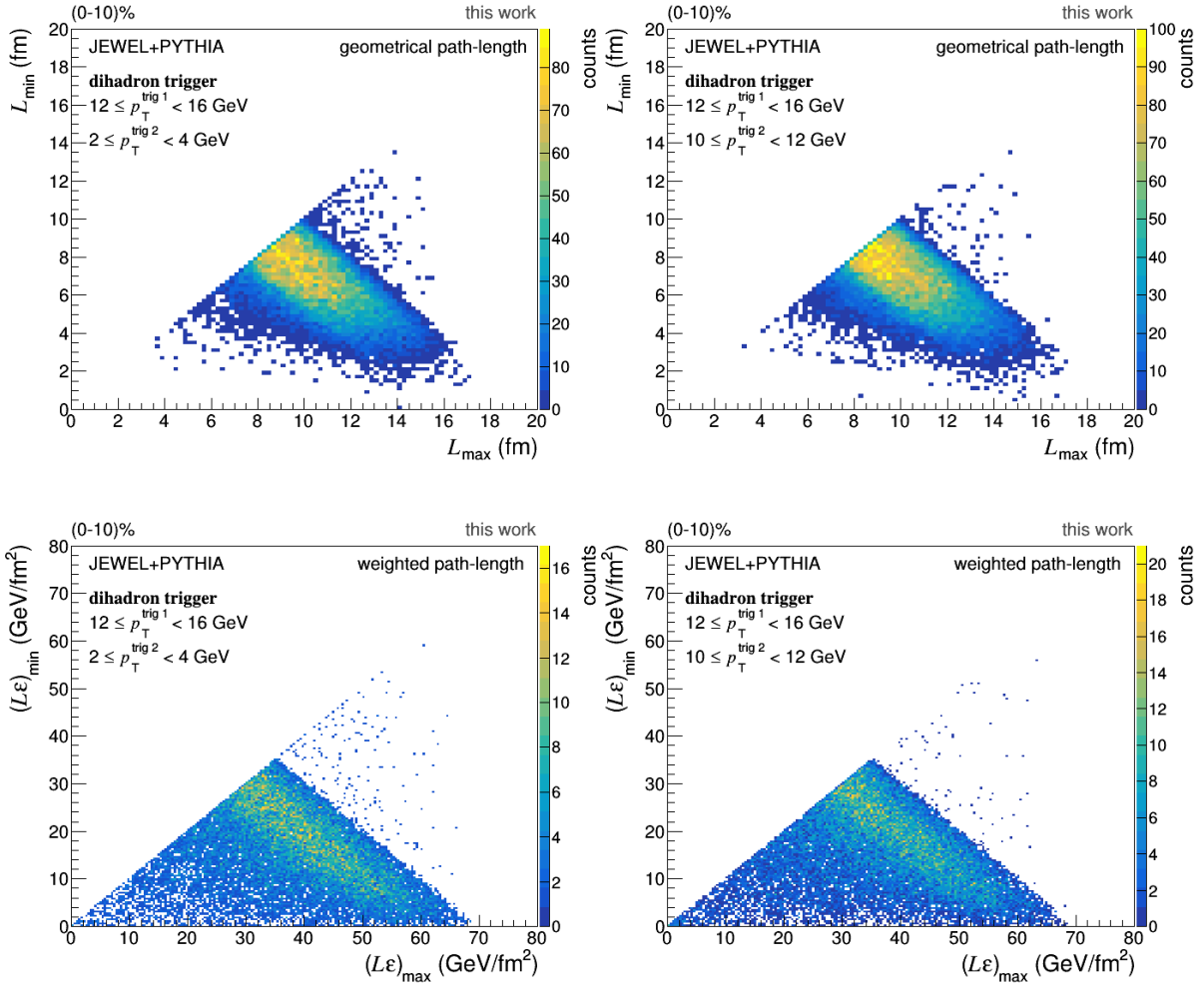


Figure 5.36: Distributions of the triggered (weighted) path-length, minimum value vs. maximum value. Left column: Most asymmetric dihadron trigger conditions. Right column: Most symmetric dihadron trigger conditions. Top: Geometrical path-length. Bottom: Weighted path-length.

## 5.5 Correlation functions

In the previous sections, jets and jet modification were characterized on a general basis. Furthermore, it was analyzed how the application of a trigger condition to the jets selects certain fragmentations or path-lengths of the scattered partons. To draw the connection to observables obtained from correlation functions, the generation of two-particle and 2+1 correlation functions, already introduced in Section 3.3, is explained in the following.

### 5.5.1 Two-particle correlations

In angular two-particle correlations, a different approach to jet measurements is taken. Instead of reconstructing the jets from all the measured particles, a single hadron is taken as a proxy for the jet. It is assumed that this hadron contains the original hard parton. The single hadron, selected from a certain  $p_T$  interval, is the trigger particle. The angular distances both in  $\varphi$  and  $\eta$  of all other particles in the event, the associated particles, to the trigger particle are calculated.  $\varphi$  is the azimuthal angle of the particles,  $\eta$  the pseudorapidity. Like it was done before in the analysis with reconstructed jets, only events for which  $|\eta_{\text{partons}}| < 1 - R = 0.4$  is fulfilled are selected. In these events, only particles within  $|\eta| < 1$  are considered for the correlation function. For a differential analysis, the associated particles are selected in momentum bins as well. This is done for all events which have a particle with  $p_T^{\text{min}} \leq p_T^{\text{trig}} < p_T^{\text{max}}$ . As triggered parton  $p_T$  range, the same bins as before were selected, i.e. bins with width 2 GeV ranging from 2-20 GeV. The associated momentum is binned with width 1 GeV, ranging from 0 to 10 GeV (both exclusive). When correlations with respect to the event plane are studied, the trigger particle is additionally sorted into one of the  $\Delta\phi$  bins already defined in Section 5.4. If multiple particles in one event fulfill the trigger condition, the relative angles between each of the trigger particles and the corresponding associated particles are calculated. If the momentum interval of the trigger and associated particles overlap, the particle with higher momentum is taken as trigger particle. To prevent correlations of a particle with itself, in overlapping trigger and associated momentum intervals, as well the barcode (a unique number assigned to each particle in an event) is taken into account. All particles are taken from the same event. The corresponding (same event) correlation function is obtained by counting the number of associated particles in an interval of  $(\Delta\varphi, \Delta\eta)$ :

$$S(\Delta\varphi, \Delta\eta) = \frac{1}{N_{\text{trig}}} \frac{d^2N}{d\Delta\varphi d\Delta\eta} \quad (5.13)$$

$$\Delta\varphi = \varphi_{\text{assoc}} - \varphi_{\text{trig}}$$

$$\Delta\eta = \eta_{\text{assoc}} - \eta_{\text{trig}}$$

The correlation function is normalized to the number of trigger particles in the selected momentum range. An example is shown in Fig. 5.37. Due to the restricted  $\eta$  range,  $|\Delta\eta|$  cannot be larger than 2. In azimuth, the whole range is accessible. The correlation function still needs to be corrected for the limited acceptance of the chosen  $\eta$  range. The peaks in Fig. 5.37 are explained after the correction was applied.

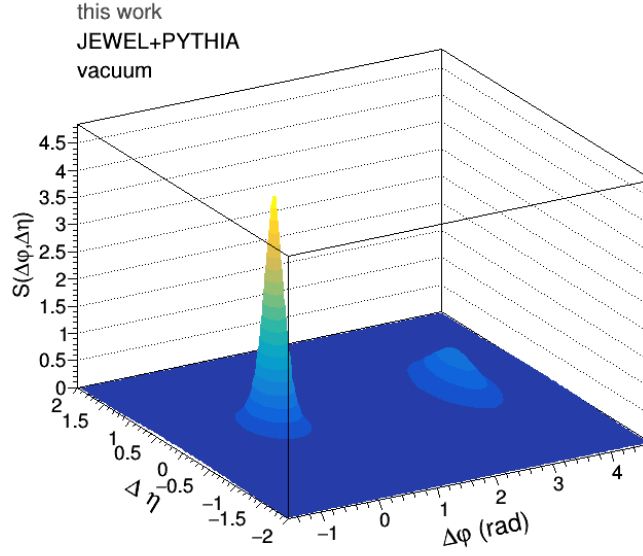


Figure 5.37: Uncorrected correlation function for  $4 \leq p_T^{\text{trig}} < 6 \text{ GeV}$  and  $2 \leq p_T^{\text{assoc}} < 3 \text{ GeV}$ .

### Correction with mixed events technique

Due to the limited acceptance in  $\eta$ , pairs of particles are detected with differing efficiency, depending on their individual  $\Delta\eta$ . Particles which are close in  $\eta$  are more probable to be detected, even if the particles are located close to the edge of the acceptance. When one particle, however, is located inside the accepted area, but the distance to another particle is large in  $\eta$  so that it lies outside of the acceptance, the pair is not detected. To correct for this effect, the mixed event technique is commonly used [47, 61, 62]. For this technique, trigger particles and associated particles are taken from different events. In this way, the particles are not physically correlated. Any correlation which is observed between two particles from different events is therefore due to acceptance effects. The particles themselves are, like for the correlation function generated with same event pairs, taken from  $|\eta| < 1$ . The cut on the partons  $\eta$ , though, is removed for the mixed events, i.e. all events which contain particles within  $\eta < 1$  are used. The strong parton  $\eta$  cut, which was used for the previous jet reconstruction as well as for the same event correlation function, is needed in these cases to ensure that the majority of the relevant particles lie inside the acceptance. In the determination of the uncorrelated background, however, the strong cut introduces a bias which disturbs the shape of the background function. The 2D mixed event function is shown in Fig. 5.38. Particles which are close in  $\eta$  are almost always detected (unless one particle is directly at the limit of the acceptance and the other one outside), while particles with  $|\Delta\eta| = 2$  are almost never detected (only when both particles are exactly at the two limits of the acceptance). The mixed event correlations are, as well, normalized. Since two particles that are located inside the accepted area with exactly the same  $\eta$  are always detected, the distribution is normalized to 1 at  $(\Delta\phi, \Delta\eta) = (0, 0)$ .

The same event correlation function is divided by the mixed event distribution to correct for the kinematic acceptance. In real data analysis, the correlation function has also to be corrected for single particle efficiencies, since real detectors detect particles not with

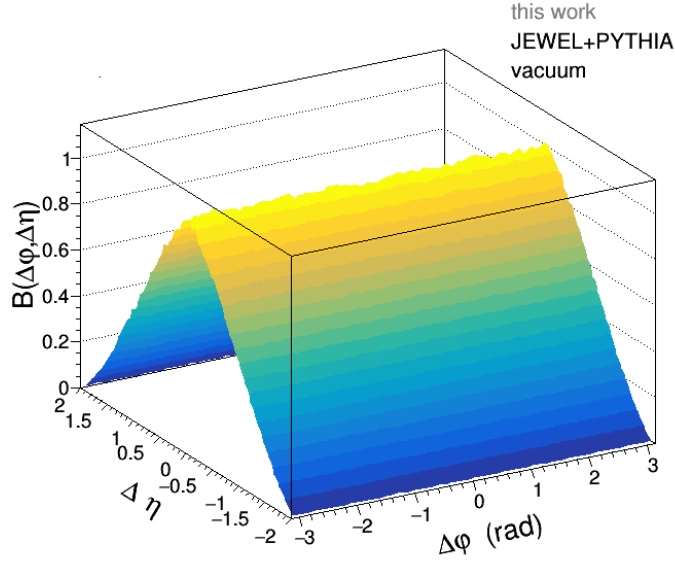


Figure 5.38: Mixed event correlation function. The same trigger and associated  $p_T$  ranges as for the same event correlations where used, but trigger and associated particles are taken from different events.

100% efficiency. However, since in JEWEL every generated particle, which is located inside the acceptance, is "detected", these corrections are not needed for this analysis. The resulting corrected correlation function ( $C = S/B$ ) is shown in Fig. 5.39. The effect of the uncorrelated background is very small in JEWEL, the only visible difference is a slight broadening of both peaks in  $\Delta\eta$ . Two peaks are observed in the correlation function, one at  $\Delta\varphi = 0 = \Delta\eta$  and one at  $\Delta\varphi = \pi$ . The second peak is smeared in  $\Delta\eta$ . The peak at  $\Delta\varphi = 0$  is caused by the particles contained in the triggered jet. Assuming they are located close to the trigger particle, the relative angles are small and result in the peak around  $\Delta\varphi = 0 = \Delta\eta$ , the near-side. The smaller peak corresponds to the recoil jet. Since the partons are emitted back-to-back in azimuth, the peak is located at  $\Delta\varphi = \pi$ , the away-side. The peak is smeared in  $\Delta\eta$ , since the pseudorapidities of both hard scattered partons depend on their momentum fraction taken from their original hadron. Contrary to the distribution shown in Section 3.3, the peak is not smeared over the complete  $\Delta\eta$  range. This is due to the  $\eta$  cut on the partons.

### Extracting the observables

From the correlation function, different observables can be extracted. The per-trigger yield  $Y$  provides insight into the number of particles which are contained within the jet. By binning the momentum of the associated particles, this can be investigated differentially. Medium modifications can be studied by comparing the yield obtained in the vacuum to the yield in the medium case:

$$I_{AA} = \frac{Y_{\text{PbPb}}}{Y_{\text{pp}}}. \quad (5.14)$$

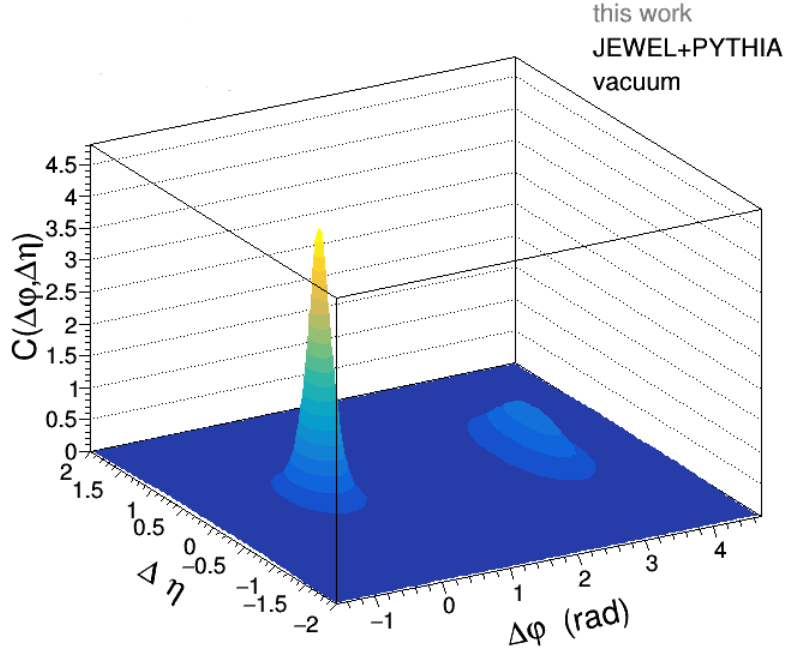


Figure 5.39: Corrected correlation function.

Deviations from 1 indicate the modifications. For example, an increased yield at low  $p_T$  and a decreased yield of high  $p_T$  associated particles going from vacuum to medium is an indicator that the high  $p_T$  particles transferred their momentum to the medium and are now observed as low  $p_T$  particles. When analyzing the  $I_{AA}$ , one has to keep in mind the previous findings. It was found, that the application of trigger conditions selects different ranges in parton  $p_T$  and jet  $p_T$  in the vacuum and medium case. Therefore, for an interpretation it has to be checked if the underlying processes are actually the same. Support for a consistent interpretation is provided by the shape of the peaks. The widths in  $\Delta\varphi$  and  $\Delta\eta$  help to identify the fragmentation and, by comparison of vacuum and medium, to infer the underlying process.

The per trigger yield is obtained by integrating the peaks individually. The integration is done by adding the bin contents of the histogram. Since uncorrelated background is non-existent in JEWEL, the integration can be done by simply singling out the peaks with adequate integration ranges. Further background subtractions are not necessary. To include the peaks of all shapes, the integration ranges are kept as large as possible. The near-side is integrated in the azimuthal range  $-\pi/2 \leq \Delta\varphi < \pi/2$  and pseudorapidity range  $-1.5 \leq \Delta\eta \leq 1.5$ . The limits in  $\Delta\eta$  are not extended to the edges of the acceptance to exclude potential statistical fluctuations from the integration. It was found that this range is sufficient to include all peak shapes. The away-side peak is integrated over the same pseudorapidity range and the azimuthal range  $\pi/2 \leq \Delta\varphi < 3\pi/2$ .

For the extraction of the widths in  $\Delta\varphi$  and  $\Delta\eta$ , the 2-dimensional distribution is projected onto the respective axes. For the width in  $\Delta\eta$ , the projection range in  $\Delta\varphi$  is restricted to the integration ranges given above. The width is defined as the standard deviation and is calculated from the bin contents, like was done for the yield. Examples

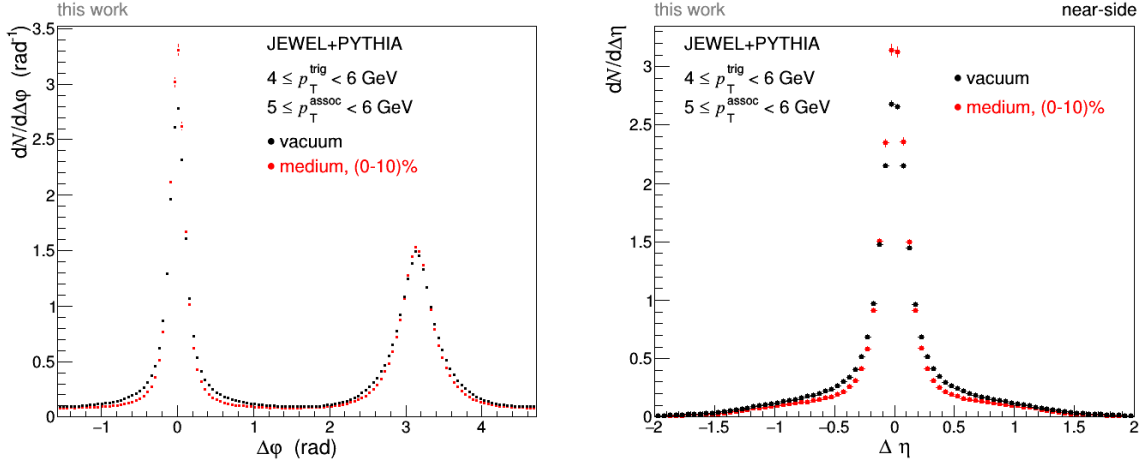


Figure 5.40: Projections of a corrected correlation function, in vacuum and in medium. Left: Projection on  $\Delta\varphi$ . Right: Projection on  $\Delta\eta$ .

of projections on  $\Delta\varphi$  and on  $\Delta\eta$  for the near-side peak can be seen in Fig. 5.40. In  $\Delta\varphi$ , both the near-side and away-side peak are visible.

### 5.5.2 2+1 correlations

For a more detailed analysis of the away-side, the two-particle correlations are extended to the 2+1 correlation analysis. In 2+1 correlations, two back-to-back hadrons are taken as trigger particles. A schematic is shown in Fig. 5.41. In this analysis, trigger 1 is required to have a momentum  $12 \leq p_T^{\text{trig } 1} < 16$  GeV. The momentum of the second trigger particle is varied between  $2 \leq p_T^{\text{trig } 2} < 4$  GeV and  $10 \leq p_T^{\text{trig } 2} < 12$  GeV in steps of 2 GeV. With these combinations of trigger  $p_T$  conditions, one can probe the shift in path-length observed in Section 5.4 and clarify, how the effects of surface bias, which were expected but not observed at the current statistics in the path-length distributions, appear in the evaluation of the correlations. The back-to-back selection is done by comparing the azimuthal angles of the two trigger particles. If they are separated by  $\pi \pm \frac{\pi}{8}$ , the particles are accepted as trigger pair:

$$\Delta\varphi_{\text{trig}} = ||\varphi_{\text{trig } 2} - \varphi_{\text{trig } 1} - \pi| < \frac{\pi}{8} \quad (5.15)$$

The relative angles of the associated particles are calculated with respect to both trigger particles. The correlation function is then generated for each trigger particle individually. The normalization factor for both histograms is the number of trigger pairs. In this way, both the ‘‘trigger’’ and ‘‘recoil’’ jet, corresponding to trigger 1 and 2, form a distinct peak on the near-side  $\Delta\varphi = 0$ .

The correction for the limited acceptance is again done with the mixed event technique. The trigger pair is taken from one event, the associated particles from another event. Both histograms are corrected with the same mixed events distribution. Also the ob-

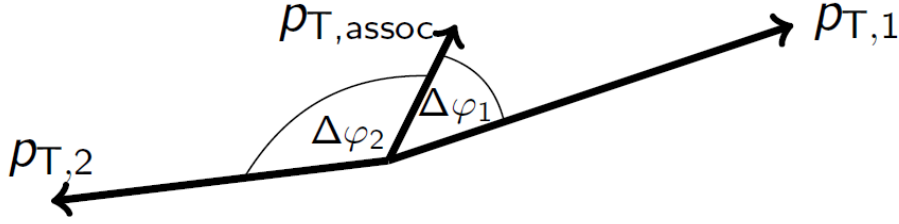


Figure 5.41: Schematics of 2+1 correlations.

servables per-trigger yield and the widths in  $\Delta\varphi$  and  $\Delta\eta$  are extracted for the 2+1 correlations.

The results from the analysis of per-trigger yield and the widths are discussed in the following. Medium and vacuum case are compared, as well as different trigger conditions. In the case of two-particle correlations, the resulting correlation functions in different bins of trigger  $\varphi$  relative to the event plane are studied. In Chapter 6, the findings of this part are brought into the greater context of the entire analysis done in this thesis.

### 5.5.3 Results

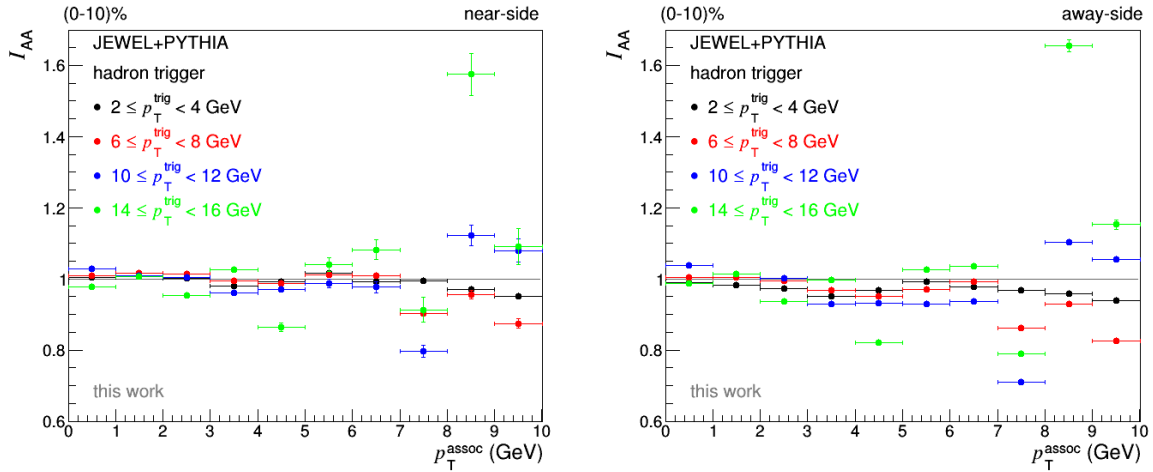


Figure 5.42:  $I_{AA}$  two-particle correlations, near and away side for different trigger conditions, for a medium with (0-10)% centrality.

First, the two-particle correlations were analyzed, with no restriction imposed on the trigger angle relative to the event plane. The distributions for different trigger conditions in (0-10)% compared to the vacuum case are displayed in Fig. 5.42. The left plot contains the  $I_{AA}$  of the near-side (i.e. of the peaks located at  $\Delta\varphi = 0$ ), the right plot the away-side ( $\Delta\varphi = \pi$ ). The distributions for all trigger conditions show large fluctuations. The mean value on both the near-side and the away-side across all  $p_T^{\text{assoc}}$  is 1. A deviation from 1 means that the jet was modified by the medium. Since no consistent deviation

from 1 is observed for the two-particle correlations  $I_{AA}$ , this gives the impression that the particle yield associated with the jets is not modified by the medium. One has to keep in mind the previous findings though. In Section 5.4, the influence of trigger conditions on the jet selection was studied. It was found that for the same parton  $p_T$ , trigger conditions select, on average, higher jet  $p_T$  in vacuum than in medium, which implies the occurrence of medium modifications. Furthermore, with the application of a trigger condition, ranges in parton and jet momenta get selected. However, there is no possibility to select a specific parton  $p_T$  with the trigger condition outside the scope of a simulation. Therefore, the  $I_{AA}$  equal to unity in this case does not mean that the hard scattered parton was not modified by the medium, but that instead of similar parton  $p_T$  similar jet  $p_T$  were selected in vacuum and in medium. This excludes the simple two-particle correlations from path-length studies, at least from the perspective of JEWEL. For a definitive statement, however, the  $I_{AA}$  and the observed fluctuations have to be investigated further and be compared to real data analysis.

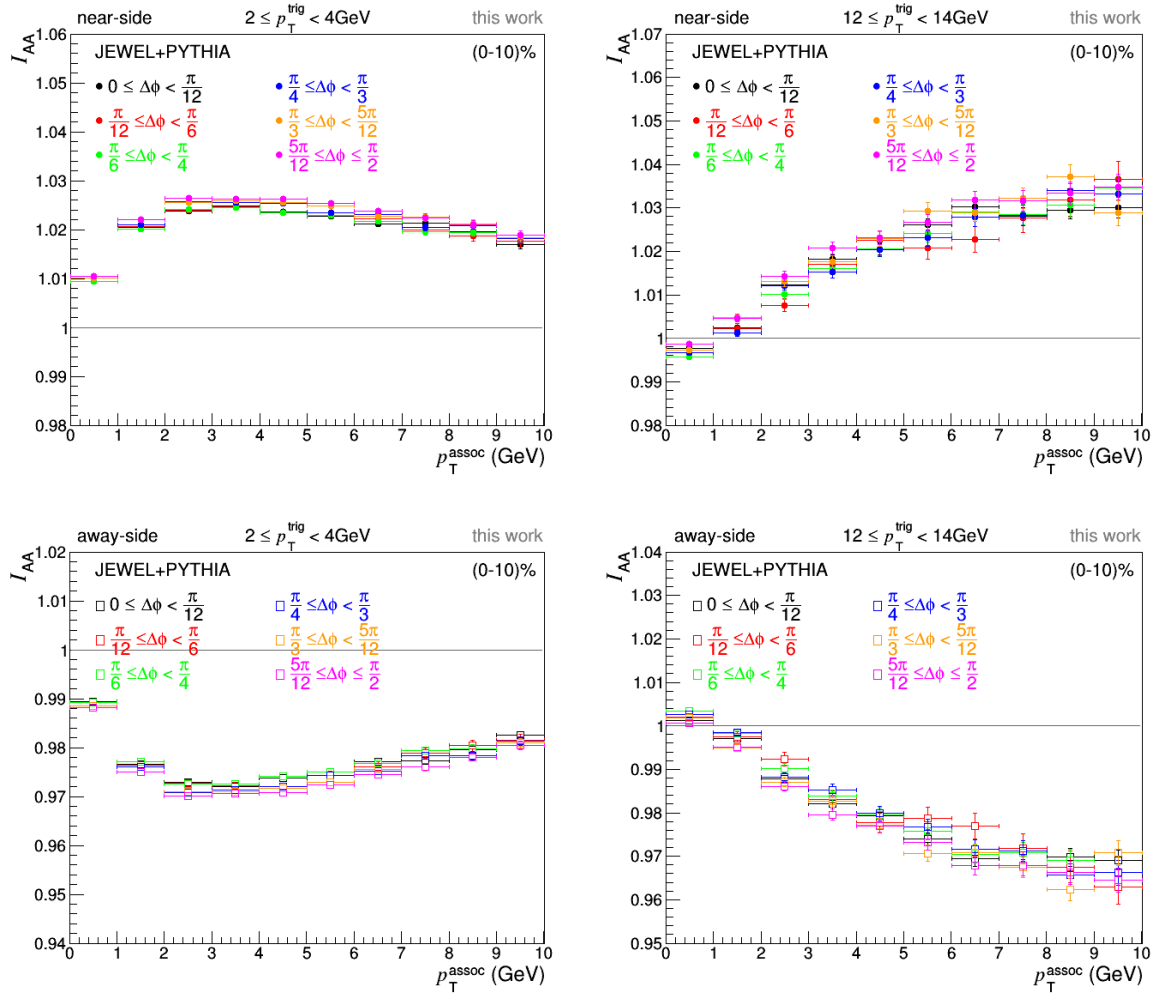


Figure 5.43:  $I_{AA}$  of two-particle correlations with respect to the event plane for two different trigger conditions, for a medium with (0-10) % centrality.

In Section 5.4, it was found that with the insertion of additional information, the jet angle relative to the event plane, the path-length for different trigger conditions can be studied in more detail than with a simple inclusive hadron trigger. Therefore, the two-particle correlations as well were studied in the different bins of the relative trigger hadron angle for each trigger  $p_T$ . The  $I_{AA}$  of the near- and away-side for two different trigger conditions and (0-10) % are shown in Fig. 5.43. Contrary to the more simple two-particle correlations, a modification of the  $I_{AA}$  is observed for different trigger conditions. In the same bin of  $\Delta\phi$ , different trigger conditions select, on average, different path-lengths. In vacuum, since there is by definition no medium, the selected jet  $p_T$  does not change when selecting a bin in  $\Delta\phi$ . In the medium case, however, the additional selection of a path-length changes the momentum of the jet for the same parton momentum. The way in which this different jet  $p_T$  selection occurs can be studied with the  $I_{AA}$ . On the near-side, the yields are enhanced in medium compared to the vacuum case. For the lowest trigger  $p_T$ , the associated particles with highest increase have momentum  $2 \leq p_T^{\text{assoc}} < 5$  GeV. For higher trigger momentum, the mostly enhanced  $p_T^{\text{assoc}}$  is shifted to the upper end of the chosen range. At the same time, the associated particles on the away-side are suppressed mirrorlike in  $p_T^{\text{assoc}}$ . This indicates that with the simultaneous selection of trigger  $p_T$  and path-length, higher jet  $p_T$  in medium than in vacuum are selected, and an even higher parton  $p_T$  compared to the simple two-particle correlations. The recoil jet then nominally experiences quenching of its high  $p_T$  fragments. The change of  $I_{AA}$  can be used to study the path-length differences between different trigger conditions.

Since the path-length for a single trigger condition was observed to be changing for different bins in  $\Delta\phi$ , one would expect to see different modulations for the same trigger condition but different relative trigger particle angles. This is not observed in Fig. 5.43 though. The  $I_{AA}$  behaves the same for all bins in  $\Delta\phi$ . For  $12 \leq p_T^{\text{trig}} < 14$  GeV, larger fluctuations are visible, but the difference between the different distributions are still not significant. This can be explained by investigating the widths of the distributions for the same trigger conditions and in the same bins in  $\Delta\phi$ , shown in Fig. 5.44. The widths in  $\Delta\phi$  are observed to be the same for all bins in  $\Delta\phi$  for the same trigger condition. The case  $\Delta\eta$  (not displayed here) is similar. This suggests that on average, regardless of the bin in relative angle, the same or at least a similar path-length is selected with a single trigger condition. Recalling that the changes in mean path-length for the same trigger condition from the most in-plane bin to the most out-of-plane bin are in magnitude on the order of the distributions widths, this seems plausible. However, for (50-60) %, the changes in mean path-length were larger compared to (0-10) % and for the highest trigger  $p_T$  exceeds the distributions width. Therefore, a larger modulation of the width and  $I_{AA}$  is expected for (50-60) %. In the distributions of the widths (bottom row of Fig. 5.44) this indeed can be observed. The changes are small when compared to the same distributions in (0-10) %. In the scope of a single trigger hadron for (50-60) % though, the differences are not significant. Therefore, the comparison of the different trigger conditions  $I_{AA}$  is done in one bin of  $\Delta\phi$  only.

Fig. 5.45 shows the  $I_{AA}$  of different trigger hadrons in the most in-plane bin of  $\Delta\phi$ . The top row contains the near-side, the bottom row the away-side. In the left column, the  $I_{AA}$  for (0-10) %, in the right column for (50-60) % is shown. The above hinted progression of  $I_{AA}$  modulation is clearly visible with the combination of several trigger conditions.

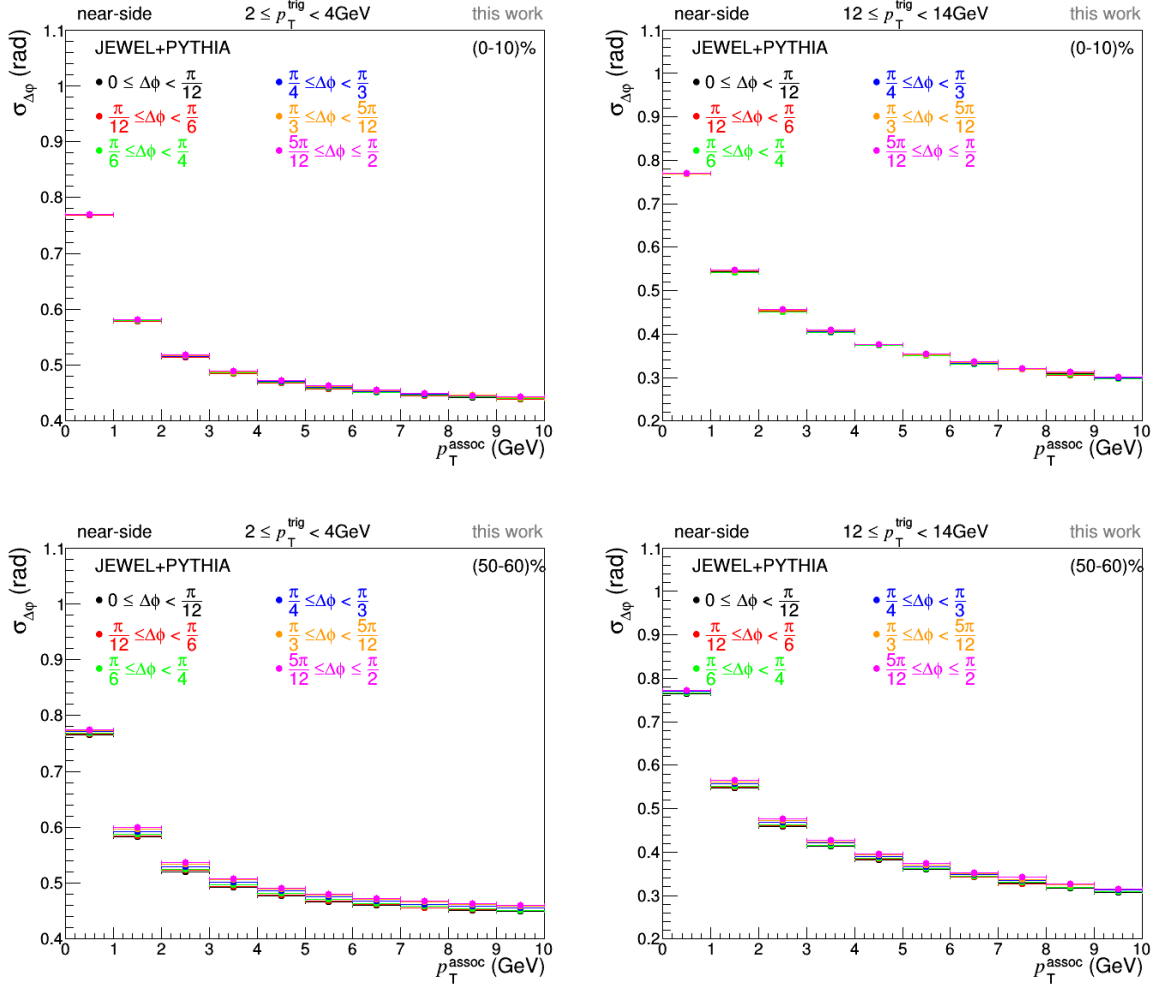


Figure 5.44: Width in  $\Delta\varphi$  of two-particle correlation functions with respect to the event plane. Top: (0-10)%. Bottom: (50-60)%.

For (50-60)% compared to (0-10)%, a diminished modulation of  $I_{AA}$  is observed. This is probably due to the overall smaller path-lengths in the (50-60)% overlap region and therefore less difference in jet  $p_T$  for vacuum and medium. For a connection of the change of  $I_{AA}$  to the path-length of the underlying partons either different trigger conditions within the same centrality or the same trigger condition for different centralities have to be compared. The change of the distribution corresponds to the change in mean path-length discussed in Section 5.4.

Lastly, the  $I_{AA}$  and widths in  $\Delta\varphi$  and  $\Delta\eta$  are discussed for the 2+1 correlations. In the investigation of the triggered jet and parton  $p_T$ , similar selected ranges in jet  $p_T$  but different ranges in parton  $p_T$  in vacuum and medium were observed for the same set of trigger conditions. Therefore, the  $I_{AA}$  for both trigger 1 and 2 (Fig. 5.46) fluctuates around unity, but no consistent influence of the medium modification is visible. In this regard, the 2+1 correlations resemble the simple two-particle correlations. Here as well, the results have to be compared to real data and further investigation of the fluctuations

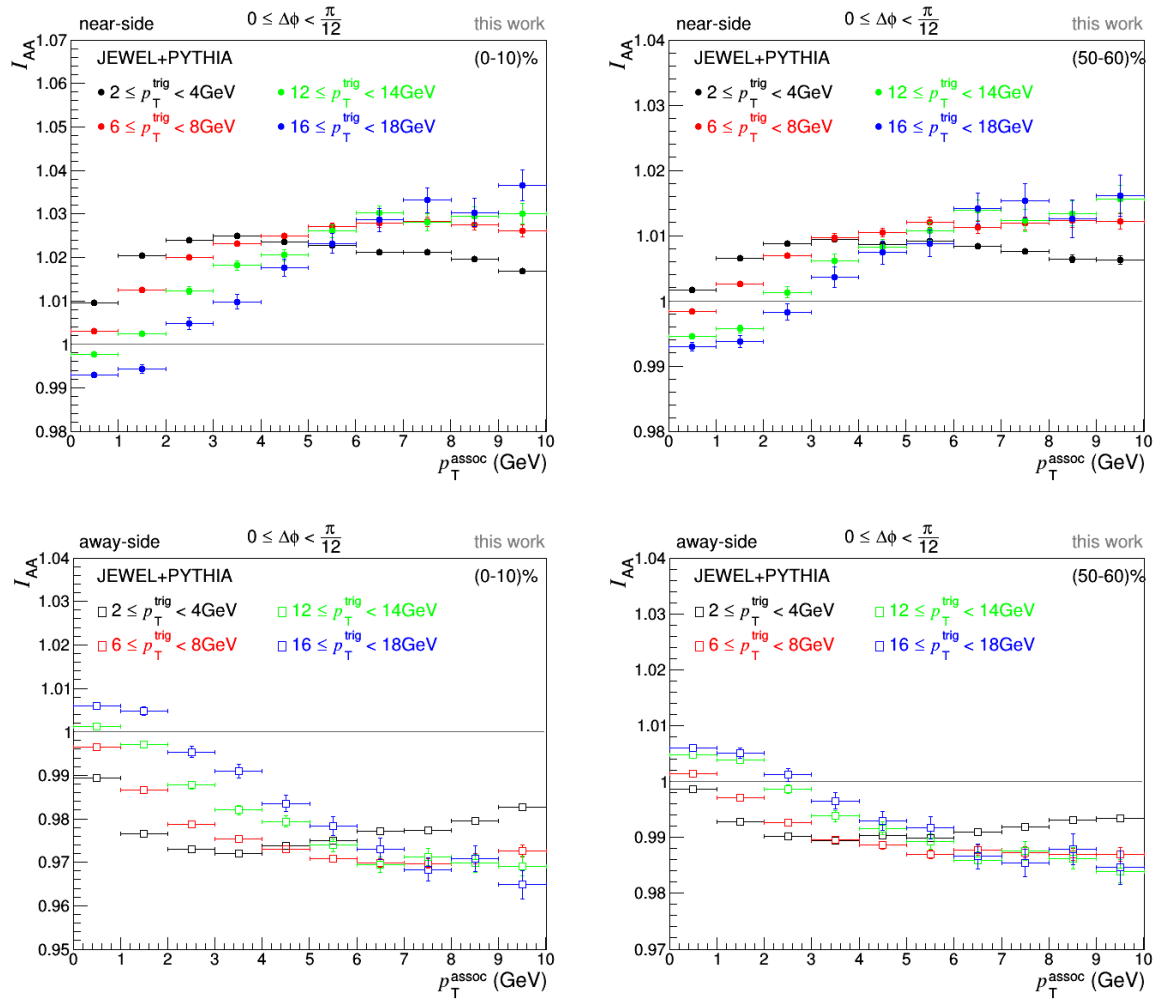


Figure 5.45:  $I_{AA}$  for the in-plane bin for different trigger conditions. Top: (0-10)%. Bottom: (50-60)%.

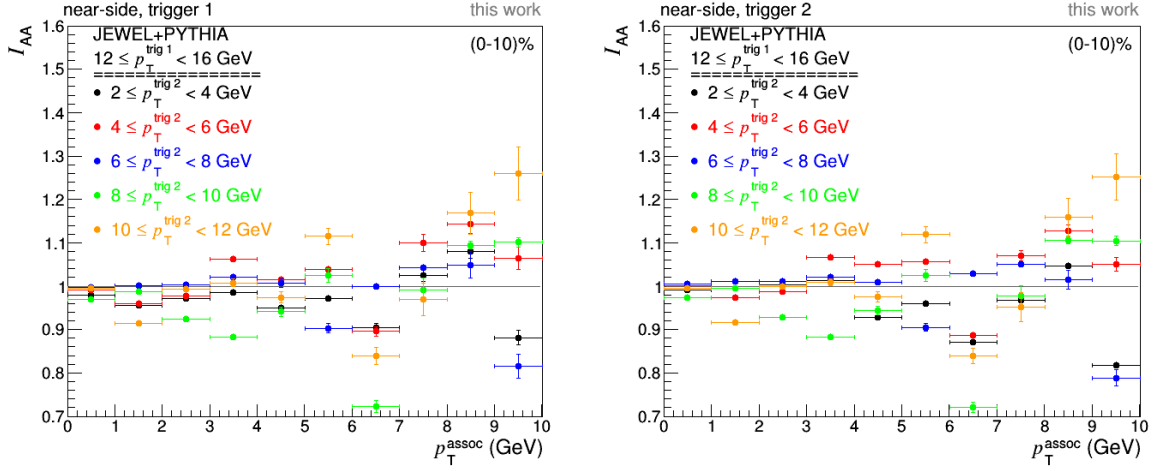


Figure 5.46:  $I_{AA}$  for 2+1 correlations, in medium with (0-10) % centrality. Left: Near-side of trigger 1. Right: Near-side of trigger 2.

is necessary. However, contrary to the two-particle correlations, in 2+1 correlations there is additional information available. The back-to-back scattered hadrons initially had the same momentum, due to momentum conservation. With the increasingly asymmetric trigger conditions, one can therefore tune the relative amount of momentum transfer between the jets and the medium. At the same time, as was shown in Section 5.4, the relative path-length between trigger 1 and trigger 2 is accessible. Even though no absolute statements can be made (e.g. that in the most asymmetric trigger conditions, the jet corresponding to trigger 2 transferred a fraction  $x$  of its momentum to the medium and traversed the medium with path-length  $y$ ), the relative path-length changes and fractions of momentum transfer can be compared for different trigger conditions.

For this, the widths of the peaks are used as observable. It was shown that the medium modifications influence the shape of the jets. Therefore, different widths in  $\Delta\varphi$  and  $\Delta\eta$  can be connected to the different path-lengths of the jets corresponding to trigger 1 and 2. The widths in  $\Delta\varphi$  and  $\Delta\eta$  for different combinations of trigger conditions are shown in Fig. 5.47. Since a comparison to vacuum fragmentations is ineffectual at this point, only the values for a (0-10) % medium are shown. The top row contains the width in  $\Delta\varphi$ , the bottom row  $\sigma_{\Delta\eta}$ . When investigating the plots, the peaks in two bins of  $p_T^{\text{assoc}}$  in each case are immediately noticeable. The  $p_T$  of the associated particles that form the peak corresponds to the momentum of the second trigger particle. Therefore, the peak is not visible in the rightmost plots, it is located out of range. The peaks form due to the selection of the trigger pairs. They are required to be back-to-back, by a maximum variation of  $\frac{\pi}{8}$ . Thus, all associated particles in the same momentum range as the trigger particle have to be located farther away from the jets than other associated particles. Otherwise it would be the trigger particle itself. For both the width in  $\Delta\varphi$  and in  $\Delta\eta$  it is observed that the difference between trigger 1 and trigger 2 decreases for more symmetric trigger conditions. While the difference in  $\sigma_{\Delta\eta}$  is especially large for  $2 \leq p_T^{\text{trig } 2} < 4 \text{ GeV}$ , they are equal for  $10 \leq p_T^{\text{trig } 2} < 12 \text{ GeV}$ . With increasing momentum of the second trigger hadron, the width in  $\Delta\eta$  for its correlation function

decreases, while the width for trigger hadron 1 increases slightly. This corresponds to the previously discussed dihadron triggered path-length distributions, where more asymmetric trigger conditions resulted in a large path-length of the jet triggered with hadron 2, a shorter path-length of the jet containing trigger 1, and vice versa. A possible explanation for this is that the particles get, in longitudinal direction, influenced by the expanding medium [63, 64]. Similar observations have been made in the evaluation of two-particles correlations, performed by the ALICE collaboration, see [63, 64]. In  $\Delta\varphi$ , the difference in width between the two trigger hadrons is much less prominent. As well, an overall change of  $\sigma_{\Delta\varphi}$  is, apart from the peak movement along the distribution, not visible. This supports the conjecture that with different trigger conditions, different underlying parton momenta get selected. However, by comparing the widths in  $\Delta\eta$  for trigger 1 and 2 for different trigger conditions one obtains information about the relative path-length between the two.

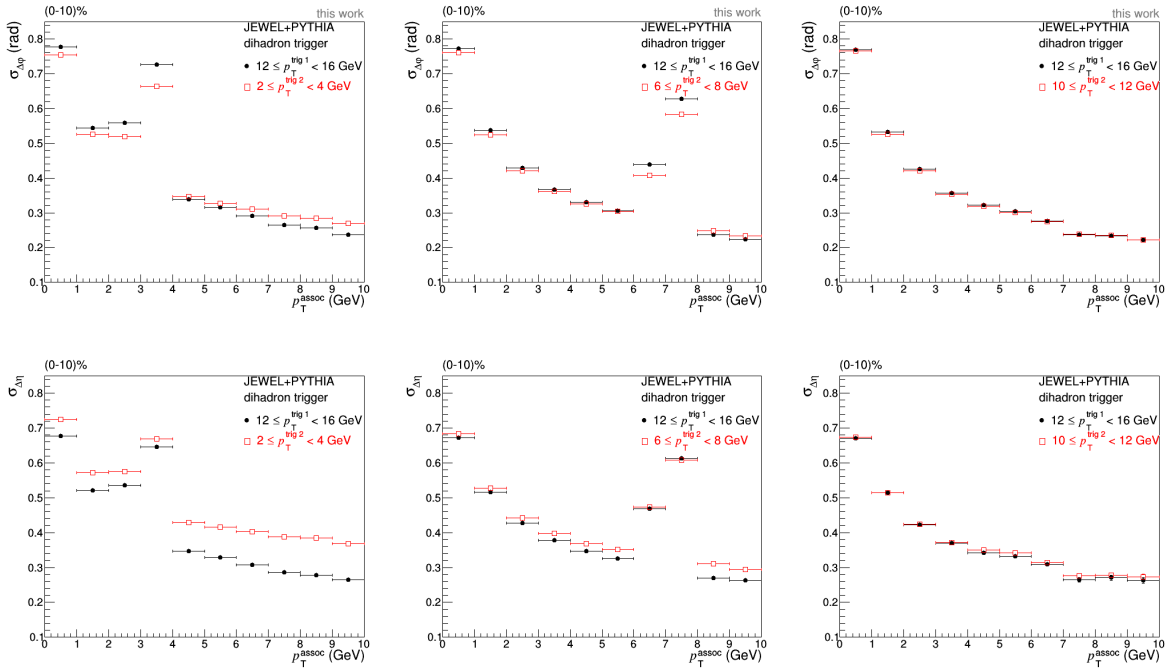


Figure 5.47: Widths in  $\Delta\varphi$  and  $\Delta\eta$  of 2+1 correlation functions for different trigger conditions.

With the evaluation of two-particle and 2+1 correlation functions and the comparison to the various path-length distributions and general (triggered) jet behavior investigated in the course of the analysis, the study in the scope of this thesis is completed. The conclusions are summarized in the following chapter. As well, an outlook is given on possible comparisons and future analysis utilizing the findings of this work.

# Chapter 6

## Conclusions and Outlook

In this thesis, the Monte Carlo simulation program JEWEL was used to study jets and the path-length of hard scattered partons in a QGP medium. Jets are a useful tool to study the properties of the QGP, since they are theoretically well understood. As well their features, being emitted back-to-back in azimuth and carrying initially the same transverse momentum due to momentum conservation, can be utilized for a detailed analysis. The aim was to carve out observables, obtained from two-particle and 2+1 angular correlation functions, that are sensitive to the different in-medium path-length of jets.

An important part and the baseline for the analysis was the characterization of jets and jet modification on a general basis. For this, the generated particles were reconstructed with the FastJet anti- $k_T$  algorithm and sorted into parton hemispheres. Parton properties associated with a reconstructed jet were taken from the parton in the same hemisphere as the jet. Distributions of reconstructed jet  $p_T$ , the average angular distance of the reconstructed jets constituents to the jet axis, the number of constituents per jet and the average transverse momentum carried by a single constituent were analyzed for different parton  $p_T$ . It was found that the jet reconstruction with a cone radius of  $R = 0.6$  captures 80-90 % of the partons transverse momentum in the leading jet. This leading jet momentum is reduced by 20-60 % for the highest to lowest parton momenta in a (0-10) % medium. On average, a (leading) jet contains less particles in medium than in vacuum. As compensation, the average transverse momentum carried by a single constituent is in medium higher for high parton  $p_T > 250$  GeV. The constituents of the jets in medium are observed to be scattered farther away from the jet axis in medium than in vacuum, although the effect decreases for increasing parton momentum. At low parton  $p_T < 30$  GeV, the jet constituents in medium are observed to be spread less compared to the vacuum case, as an artifact of the chosen jet cone radius.

In the next step, the geometrical and energy-density weighted path-length of the hard scattered partons was determined. For the geometrical path-length, the distance from the scattering vertex to the point where the parton leaves the overlap region was calculated. For the energy-density weighted path-length, the local energy density was summed in steps of 0.1 fm along the path and normalized by the number of steps. The weighted path-length was then calculated as the product of geometrical path-length and the mean energy density along the path. It was found that the combination of path-lengths of the

back-to-back scattered hadrons reproduces the shape of the overlap region. Due to the scattering vertex distribution, path-lengths  $L \lesssim 3$  fm do not occur. With the energy-density weighting, the distribution is smeared, due to the different weights. Investigating jet  $p_T$  spectra in bins of parton  $p_T$  and path-length, a clear connection of momentum transfer and the magnitude of the path-length was found. High  $p_T$  spectra are suppressed for the same parton momentum range but larger path-lengths.

A further important step in the analysis was the investigation of triggered distributions. For this, the leading track of a reconstructed jet in different ranges of  $p_T^{\text{trig}}$  was used to generate the distributions for triggered jet  $p_T$ , number of constituents per triggered jets, and so on. With the application of a trigger condition different ranges in parton  $p_T$  and jet  $p_T$  get selected. With increasing momentum of the trigger hadron, the reconstructed triggered jet  $p_T$  increases as well. On average, triggered jets in medium carry less transverse momentum than in vacuum for the same trigger condition. The medium jets were found to contain less particles for the same triggered jet  $p_T$  than in vacuum, but the single constituents on average carry a larger transverse momentum. This indicates that the soft fragments of the parton fragmentation are scattered outside the scope of a single jet in the sense of the reconstruction algorithm. Correspondingly, the remaining constituents with on average higher transverse momentum per particle are located closer to the triggered jet axis than in equivalent jets in the vacuum case. For the triggered jets generated by JEWEL, the main fraction of the jets transverse momentum is, on average, carried by the leading particle.

The path-length which is on average triggered with a certain trigger condition was investigated for single hadron triggers, hadron triggers with respect to the event plane and for back-to-back dihadron trigger pairs in different transverse momentum ranges. On average, a higher  $p_T$  trigger hadron corresponds to a shorter path-length. In the event plane studies, an increasing mean path-length was found when going from the most in-plane bin in  $\Delta\phi$  to the most out-of-plane bin. The dependence on  $\Delta\phi$  was found to be stronger for high  $p_T$  trigger particles and for peripheral systems. For dihadron trigger pairs, the asymmetry of the trigger condition is reflected in the asymmetry of the mean triggered path-length. For the most asymmetric trigger conditions, the difference in path-length for trigger 1 and trigger 2 is  $\sim 2$  fm, which decreases to  $\sim 0.3$  fm for the most symmetric trigger conditions. Interestingly, a variation of the second trigger particles momentum as well influences the path-length of the first trigger particle, although the momentum range was fixed for all combinations. Therefore, only relative path-lengths between the two jets can be determined by comparing the trigger particles. The picture of a surface bias effect is not supported by JEWEL simulations. Since with different trigger conditions, usually different underlying parton  $p_T$  get selected, path-lengths can only be determined as relative change between different trigger conditions. The changing underlying system as well complicates the determination of the momentum transferred from the parton to the medium. For most distributions, the change in mean path-length between different trigger conditions was found to be on the order of or smaller than the widths of the distributions. For distributions generated in different bins of angle relative to the event plane, however, changes in the mean path-length larger than the widths of the distributions were found for either the same trigger condition and between different centralities or the same centrality class but different trigger  $p_T$ . Therefore, the comparison of those

---

constitute the most promising tool to study path-length found in this analysis. In the last part of the analysis, two-particle and 2+1 angular correlation functions were evaluated. For two-particle correlations with no restriction imposed on the trigger angle relative to the event plane, the  $I_{AA}$  of both the near-side and the away-side was found to be on average consistent with unity for all trigger conditions. This indicates that in correlation functions, the same jet  $p_T$  is accessed in vacuum and in medium. Since medium modifications were observed in the general and triggered distributions, this leads to the conclusion that the same jet  $p_T$  but different underlying parton  $p_T$  are accessed. This prohibits statements about the medium modifications themselves and, without further information, excludes two-particle correlations from path-length studies. Modulations, however, were found for two-particle correlations in different bins for the trigger particle angle relative to the event plane. With the selection of a path-length, different jet momenta are selected in medium and in vacuum. The selected path-length is similar in all bins in  $\Delta\phi$ , due to the large widths of the path-length distributions. Changes between different trigger conditions within the same centrality class, or for the same trigger condition between different centrality classes can be used to infer relative path-length changes between the two conditions. For 2+1 correlations, like for two-particle correlations, the  $I_{AA}$ , was found to be on average consistent with unity. For both the two-particle and the 2+1 correlations  $I_{AA}$  further investigation of the fluctuations are necessary. In the case of 2+1 correlations, however, the back-to-back nature of the trigger pairs can be used to determine relative path-length changes between the two trigger particles. The difference in width in  $\Delta\eta$  was found to increase significantly for increasingly asymmetric trigger conditions. A possible explanation was found in the influence of the longitudinal expansion on  $\sigma_{\Delta\eta}$  [63, 64]. With a comparison of the changes in width, the relative path-length changes between trigger 1 and trigger 2 can be determined. However, overall it was found that the path-length selected by different trigger conditions is dominated by fluctuations, where there are only small biases due to the interplay of path-length dependent jet quenching and the geometry.

For a general validation of this thesis findings, the results of the analysis have to be compared both to real data and the results obtained with other Monte Carlo simulations. JEWEL simulations were already compared to different jet measurements [51] and found to be satisfactorily consistent with the data, especially at high  $p_T$ . In [65, 66] the  $I_{AA}$  obtained with JEWEL is on average consistent with what was found in this analysis, however the simulations underestimate the data especially at low  $p_T$ . Therefore, further studies are needed. The additional involvement of other simulations will be helpful to clarify the open questions. A possible Monte Carlo simulator for comparison, which as well implements the interactions of jets and a QGP medium, is YaJEM [67].



# Bibliography

1. Thomson, M. *Modern particle physics* ISBN: 978-1-107-03426-6 and 1-107-03426-4 (Cambridge University Press, Cambridge, 2013).
2. Gell-Mann, M. THE EIGHTFOLD WAY: A THEORY OF STRONG INTERACTION SYMMETRY. doi:10.2172/4008239 (Mar. 1961).
3. Ne'eman, Y. Derivation of strong interactions from a gauge invariance. *Nuclear Physics* **26**, 222–229. ISSN: 0029-5582 (1961).
4. Gell-Mann, M. Symmetries of Baryons and Mesons. *Phys. Rev.* **125**, 1067–1084 (3 Feb. 1962).
5. Ellis, R. K., Stirling, W. J. & Webber, B. R. QCD and collider physics. *Camb. Monogr. Part. Phys. Nucl. Phys. Cosmol.* **8**, 1–435 (1996).
6. Cabibbo, N. & Parisi, G. Exponential Hadronic Spectrum and Quark Liberation. *Phys. Lett.* **59B**, 67–69 (1975).
7. Collins, J. C. & Perry, M. J. Superdense Matter: Neutrons or Asymptotically Free Quarks? *Phys. Rev. Lett.* **34**, 1353–1356 (21 May 1975).
8. Sarkar, S., Satz, H. & Sinha, B. *The Physics of the Quark-Gluon-Plasma* ISBN: 978-3-642-02285-2. doi:10.1007/978-3-642-02286-9 (Springer, Berlin Heidelberg, 2010).
9. Aamodt, K. *et al.* Two-pion Bose-Einstein correlations in central Pb-Pb collisions at  $\sqrt{s_{NN}} = 2.76$  TeV. *Phys. Lett.* **B696**, 328–337 (2011).
10. Steinbrecher, P. The QCD crossover at zero and non-zero baryon densities from Lattice QCD. *Nucl. Phys.* **A982**, 847–850 (2019).
11. Zapp, K. C., Ingelman, G., Rathsman, J., Stachel, J. & Wiedemann, U. A. A Monte Carlo Model for 'Jet Quenching'. *Eur. Phys. J.* **C60**, 617–632 (2009).
12. Zapp, K. C., Stachel, J. & Wiedemann, U. A. A Local Monte Carlo implementation of the non-abelian Landau-Pomeranchuk-Migdal effect. *Phys. Rev. Lett.* **103**, 152302 (2009).
13. Zapp, K. C., Stachel, J. & Wiedemann, U. A. A local Monte Carlo framework for coherent QCD parton energy loss. *JHEP* **07**, 118 (2011).
14. Cacciari, M., Salam, G. P. & Soyez, G. FastJet User Manual. *Eur. Phys. J.* **C72**, 1896 (2012).
15. Cacciari, M. & Salam, G. P. Dispelling the  $N^3$  myth for the  $k_t$  jet-finder. *Phys. Lett.* **B641**, 57–61 (2006).

16. *Chin. Phys. C* **37**. <<http://pdg.lbl.gov/>>.
17. Fritzsche, H. & Gell-Mann, M. Current algebra: Quarks and what else? *eConf C720906V2*, 135–165 (1972).
18. Fritzsche, H., Gell-Mann, M. & Leutwyler, H. Advantages of the Color Octet Gluon Picture. *Phys. Lett.* **47B**, 365–368 (1973).
19. Bethke, S. Experimental tests of asymptotic freedom. *Prog. Part. Nucl. Phys.* **58**, 351–386 (2007).
20. Hagedorn, R. Statistical thermodynamics of strong interactions at high-energies. *Nuovo Cim. Suppl.* **3**, 147–186 (1965).
21. Chen, C.-H. Studying the Early Universe via Quark-Gluon Plasma. *Nuclear Physics B - Proceedings Supplements* **246-247**. Proceedings of the 9th International Symposium on Cosmology and Particle Astrophysics, 38–41. ISSN: 0920-5632 (2014).
22. Boyanovsky, D., de Vega, H. & Schwarz, D. Phase Transitions in the Early and Present Universe. *Annual Review of Nuclear and Particle Science* **56**, 441–500 (2006).
23. Shuryak, E. V. Quark-Gluon Plasma and Hadronic Production of Leptons, Photons and Psions. *Phys. Lett.* **78B**. [*Yad. Fiz.*28,796(1978)], 150 (1978).
24. *RHIC homepage* <<https://www.bnl.gov/RHIC/>>.
25. Adams, J. *et al.* Experimental and theoretical challenges in the search for the quark gluon plasma: The STAR Collaboration’s critical assessment of the evidence from RHIC collisions. *Nucl. Phys.* **A757**, 102–183 (2005).
26. Adcox, K. *et al.* Formation of dense partonic matter in relativistic nucleus-nucleus collisions at RHIC: Experimental evaluation by the PHENIX collaboration. *Nucl. Phys.* **A757**, 184–283 (2005).
27. *GSI homepage* <<https://www.gsi.de/start/aktuelles.htm>>.
28. Evans, L. & Bryant, P. LHC Machine. *JINST* **3**, S08001 (2008).
29. Aamodt, K. *et al.* The ALICE experiment at the CERN LHC. *JINST* **3**, S08002 (2008).
30. Rosnet, P. *Quark-Gluon Plasma: from accelerator experiments to early Universe in 11th Rencontres du Vietnam: Cosmology: 50 years after CMB discovery Quy Nhon, Vietnam, August 16-22, 2015* (2015). arXiv: 1510.04200 [hep-ph].
31. Miller, M. L., Reygers, K., Sanders, S. J. & Steinberg, P. Glauber Modeling in High-Energy Nuclear Collisions. *Annual Review of Nuclear and Particle Science* **57**, 205–243 (2007).
32. Abelev, B. *et al.* Centrality determination of Pb-Pb collisions at  $\sqrt{s_{NN}} = 2.76$  TeV with ALICE. *Phys. Rev.* **C88**, 044909 (2013).
33. Collaboration, S. Azimuthal Anisotropy and Correlations in the Hard Scattering Regime at RHIC. *Phys. Rev. Lett.* **90**, 032301 (3 Jan. 2003).
34. Ackermann, K. H. *et al.* Elliptic flow in Au + Au collisions at  $\sqrt{s_{NN}} = 130$  GeV. *Phys. Rev. Lett.* **86**, 402–407 (2001).

35. Collaboration, A. Anisotropic Flow of Charged Particles in Pb-Pb Collisions at  $\sqrt{s_{NN}} = 5.02$  TeV. *Phys. Rev. Lett.* **116**, 132302 (13 Apr. 2016).
36. Aad, G. *et al.* Measurement of flow harmonics with multi-particle cumulants in Pb+Pb collisions at  $\sqrt{s_{NN}} = 2.76$  TeV with the ATLAS detector. *Eur. Phys. J.* **C74**, 3157 (2014).
37. Collaboration, C. Measurement of higher-order harmonic azimuthal anisotropy in PbPb collisions at  $\sqrt{s_{NN}} = 2.76$  TeV. *Phys. Rev. C* **89**, 044906 (4 Apr. 2014).
38. Dokshitzer, Y. L. Calculation of the Structure Functions for Deep Inelastic Scattering and  $e^+ e^-$  Annihilation by Perturbation Theory in Quantum Chromodynamics. *Sov. Phys. JETP* **46**, 641–653 (1977).
39. Gribov, V. N. & Lipatov, L. N. Deep inelastic  $e p$  scattering in perturbation theory. *Sov. J. Nucl. Phys.* **15**, 438–450 (1972).
40. Lipatov, L. N. The parton model and perturbation theory. *Sov. J. Nucl. Phys.* **20**, 94–102 (1975).
41. Altarelli, G. & Parisi, G. Asymptotic Freedom in Parton Language. *Nucl. Phys.* **B126**, 298–318 (1977).
42. Campbell, J., Huston, J. & Krauss, F. *The black book of quantum chromodynamics: a primer for the LHC era* doi:10.1093/oso/9780199652747.001.0001 (Oxford University Press, Oxford, 2018).
43. Bjorken, J. D. Energy Loss of Energetic Partons in Quark - Gluon Plasma: Possible Extinction of High  $p(t)$  Jets in Hadron - Hadron Collisions. *FERMILAB-PUB-82-059-THY* (1982).
44. Braaten, E. & Thoma, M. H. Energy loss of a heavy quark in the quark-gluon plasma. *Phys. Rev. D* **44**, R2625–R2630 (1991).
45. Baier, R., Dokshitzer, Y. L., Mueller, A. H., Peigne, S. & Schiff, D. Radiative energy loss of high-energy quarks and gluons in a finite volume quark - gluon plasma. *Nucl. Phys.* **B483**, 291–320 (1997).
46. Domdey, S., Ingelman, G., Pirner, H. J., Rathsmann, J., Stachel, J. & Zapp, K. QCD Evolution of Jets in the Quark-Gluon Plasma. *Nucl. Phys.* **A808**, 178–191 (2008).
47. Aamodt, K. *et al.* Particle-yield modification in jet-like azimuthal di-hadron correlations in Pb-Pb collisions at  $\sqrt{s_{NN}} = 2.76$  TeV. *Phys. Rev. Lett.* **108**, 092301 (2012).
48. Zimmermann, M. B. *Multi-particle Correlation Studies in Heavy-Ion Collisions at the LHC* Presented 06 Dec 2016 (Sept. 2016). <<http://cds.cern.ch/record/2314849>>.
49. Renk, T. & Eskola, K. J. Prospects of medium tomography using back-to-back hadron correlations. *Phys. Rev. C* **75**, 054910 (5 May 2007).
50. Pei, H. *Jet Studies in STAR via 2+1 Correlations in 19th International Workshop on Deep-Inelastic Scattering and Related Subjects (DIS 2011) Newport News, Virginia, April 11-15, 2011* (2011). arXiv: 1110.1445 [nucl-ex].

51. Zapp, K. C., Krauss, F. & Wiedemann, U. A. A perturbative framework for jet quenching. *JHEP* **03**, 080 (2013).
52. Sjostrand, T., Mrenna, S. & Skands, P. Z. PYTHIA 6.4 Physics and Manual. *JHEP* **05**, 026 (2006).
53. Bjorken, J. D. Highly Relativistic Nucleus-Nucleus Collisions: The Central Rapidity Region. *Phys. Rev.* **D27**, 140–151 (1983).
54. Zapp, K. C. JEWEL 2.0.0: directions for use. *Eur. Phys. J.* **C74**, 2762 (2014).
55. Dobbs, M. & Hansen, J. B. The HepMC C++ Monte Carlo event record for High Energy Physics. *Comput. Phys. Commun.* **134**, 41–46 (2001).
56. *HepMC a C++ Event Record for Monte Carlo Generators* <<http://lcgapp.cern.ch/project/simu/HepMC/>>.
57. Cacciari, M., Salam, G. P. & Soyez, G. The anti- $k_t$  jet clustering algorithm. *JHEP* **04**, 063 (2008).
58. Peng, X.  $\pi^0$ -hadron correlations in pp and Pb–Pb collisions and  $\pi^0$  elliptic flow in Pb–Pb collisions measured at the ALICE experiment. *Nuclear and Particle Physics Proceedings* **289-290**. 8th International Conference on Hard and Electromagnetic Probes of High Energy Nuclear Collisions, 346–349. ISSN: 2405-6014 (2017).
59. Mazer, J. Exploring Jet-Hadron correlations at the LHC with ALICE. *Journal of Physics: Conference Series* **736**, 012021 (Aug. 2016).
60. Agakishiev, H. *et al.* Studies of di-jet survival and surface emission bias in Au+Au collisions via angular correlations with respect to back-to-back leading hadrons. *Phys. Rev.* **C83**, 061901 (2011).
61. Wang, F. Dihadron correlations in d+Au collisions from STAR. *Nuclear Physics A* **926**. IS2013, 250–257. ISSN: 0375-9474 (2014).
62. Chatrchyan, S. *et al.* Centrality dependence of dihadron correlations and azimuthal anisotropy harmonics in PbPb collisions at  $\sqrt{s_{NN}} = 2.76$  TeV. *Eur. Phys. J.* **C72**, 2012 (2012).
63. Adam, J. *et al.* Anomalous evolution of the near-side jet peak shape in Pb-Pb collisions at  $\sqrt{s_{NN}} = 2.76$  TeV. *Phys. Rev. Lett.* **119**, 102301 (2017).
64. Adam, J. *et al.* Evolution of the longitudinal and azimuthal structure of the near-side jet peak in Pb-Pb collisions at  $\sqrt{s_{NN}} = 2.76$  TeV. *Phys. Rev.* **C96**, 034904 (2017).
65. Adam, J. *et al.* Jet-like correlations with neutral pion triggers in pp and central Pb–Pb collisions at 2.76 TeV. *Phys. Lett.* **B763**, 238–250 (2016).
66. Greeshma, K. M. ' $2+1$ ' correlations in Pb–Pb collisions at  $\sqrt{s_{NN}} = 2.76$  TeV with ALICE@LHC Quark Matter 2017: Poster session. <<https://indico.cern.ch/event/433345/contributions/2358134/>>.
67. Renk, T. YaJEM: a Monte Carlo code for in-medium shower evolution. *Int. J. Mod. Phys.* **E20**, 1594–1599 (2011).

Erklärung:

Ich versichere, dass ich diese Arbeit selbstständig verfasst habe und keine anderen als die angegebenen Quellen und Hilfsmittel benutzt habe.

Heidelberg, den (Datum) .....